Hybrid Integration of Quantum Dot-Nanowires with Photonic Integrated Circuits

by

Edith Yeung

Thesis submitted to the University of Ottawa
In partial fulfillment of the requirements
For the M.Sc. degree in
Physics

Department of Physics
Faculty of Science
University of Ottawa

Abstract

Semiconductor quantum dots are promising candidates as bright, indistinguishable, single-photon sources—making them desirable for applications in quantum computing and quantum cryptography protocols. By embedding the quantum dots in III-V nanowires, the collection efficiency from the quantum dot is greatly increased. Our goal is to develop a platform that allows for the stable and efficient generation of single-photons on chip. This on-chip design offers an enhanced degree of stability and miniaturization, important in many applications involving the processing of quantum information.

In this thesis, we demonstrate the efficient coupling of quantum light generated in a III-V photonic nanowire to a silicon-based photonic integrated circuit. We use high quality SiN waveguide devices fabricated by a foundry (LIGENTEC) to minimize coupling and propagation losses through the waveguide. A hybrid integration of these single-photon sources with a photonic integrated circuit is developed by employing a "pick & place" method which uses a nanomanipulator in a scanning electron microscope setup. By tailoring the nanowire geometry, we are able to maximize the efficient coupling between the optical mode of the photonic nanowire and an accompanying SiN waveguide through evanescent coupling.

To determine the effectiveness of our integration method, we compare our hybrid devices with free-standing nanowires on their growth substrate. For each set, we measured the optical properties (brightness, spectral purity, lifetime, and single-photon purity) and efficiencies of the devices.

We have shown that using tapered nanowires with embedded quantum dots coupled to on-chip photonic structures is a viable route for the fabrication of stable, high-efficiency, single-photon sources. Although the measured collection efficiencies from device to device were substantially different ($9.6\% \sim 93\%$), we have found that the optical properties of the hybrid devices were hardly impacted from the transfer process. In fact, from the same nanowire that achieved 93% coupling efficiency, we were able to measure a single photon purity of 97%. By comparing the amount of emitted light collected from both ends of the nanowire (taper and base), we confirmed that the coupling efficiency of the devices have a strong dependence on the geometry of the nanowire as collection from the taper yielded count rates at least $10\times$ greater than from the base.

From our promising results, we can envision integrating the nanowire devices with different types of photonic structures such as ring resonators.

Statement of Contributions

For this thesis, I developed the transfer technique for moving nanowires from a growth substrate to chips containing SiN waveguides and measured all the properties of the transferred nanowires. This is the first time anyone has measured transferred, high-quality nanowires on commercial, foundry quality chips. In addition, I was involved in many other projects including the optical characterization of nanowires on growth substrates for both single and multi-dot devices which led to two publications. I also developed a suite of control software for the operation of optical equipment in the lab and for the analysis and optical characterization of nanowire-quantum dot emissions.

This thesis was entirely written by the author. I would like to identify that this was a big project and many others were involved. All of the research was done in conjunction with employees of National Research Council Canada (NRC) and fellow graduate student Patrick Laferrière.

The nanowires used in this thesis were grown by Dr. Philip J. Poole. Chips containing the SiN waveguides were designed by Dr. Robin L. Williams though simulations and the layout drawn with CAD software by Dr. Khaled Mnaymneh to be fabricated by the commercial foundry LIGENTEC. Dr. David B. Northeast provided all the waveguide simulations shown in this thesis.

Access to the optics lab was provided by Dr. Robin L. Williams and Dr. Dan Dalacu including all the equipment used for optical measurements — lasers, spectrometers, etalons, single-photon detectors, counting cards, cryostats, optical components, cameras, and computers.

Optical measurements for the free-standing nanowires including PL spectra, correlation measurements, and lifetime measurements were conducted alongside Isabelle Miron (PL spectra only) and Patrick Laferrière. However, the same three types of experiments were conducted solely by me for the hybrid devices. Software for quickly extracting the fitted intensities from PL spectra as a function of laser pump-power was written and used by me. All data collection for Section 4.3 on excitonic complexes of free-standing nanowires was split evenly between me and Patrick.

Both Dr. David B. Northeast and I were involved in the nanomanipulation of nanowires onto SiN waveguides with Dr. Northeast primarily playing the role of a mentor during the transfer process while I was at the controls. He also later assisted in the setting up of the system for loss measurements of the nanowires on waveguides. I conducted all the loss measurements for the waveguides both for ones with (Figure 5.2(c)) and without (Figure 5.1(a)) nanowires.

Software for data collection from a TimeTagger was written by Henri Morin. This software was used for all counting, correlation, and lifetime measurements.

I conducted the linewidth measurements with the temperature-controlled etalon for the hybrid device whereas Isabelle Miron conducted linewidth measurements for the free-standing nanowires using software she wrote to collect spectra with the temperature-controlled etalon. The measurements showing the fine-structure splittings in Figure 4.12(a)

were conducted by Aria Yin who also wrote the program to take future piezo-controlled etalon, linewidth measurements. The power-dependent PL spectra for above-band and quasi-resonant pumping in Figure 4.13 were conducted by Patrick Laferrière. The Hong-Ou-Mandel measurements were primarily conducted by me with the assistance of Dr. Dalacu and Dr. Northeast. PL spectra of nanowires on ring resonators were conducted by me, but measurements of the modes of the ring resonator (Figure 6.2(c)) were conducted by Dr. Payman Rasekh.

The author has attempted to acknowledge all contributions from collaborators at the appropriate points in each chapter.

Acknowledgements

I would first like to thank Dr. Dan Dalacu for first reaching out to me and inviting me to visit his lab at the National Research Council of Canada in the summer of 2019. At this visit, I was first introduced to epitaxially grown quantum dots in nanowire waveguide structures. I became quickly fascinated with the topic and later found myself pursuing a masters degree under his supervision. I would also like to thank him for his encouragement, patience, and countless hours helping me complete this thesis.

I would also like to thank my lab partner, Patrick Laferrière, who taught me the basics of proper laser alignment and safety. He served as my mentor when I first joined the research group, taught me how to conduct experiments and analyze the data, and explained basic concepts to me in detail.

I thank the co-op students, Henri Morin, Isabelle Miron, and Aria Xinyao Yin, who helped write many of the automation programs used to take the data for various experiments. Without them, data acquisition would have been much slower. I would especially like to thank Isabelle Miron for taking the data for high-resolution linewidth measurements with the temperature-controlled etalon and Aria Yin for taking the high-resolution polarization-dependent spectra shown in this thesis.

Thank you, Dr. David B. Northeast, for providing guidance and programming advice whenever I needed it. He is the one who provided all the simulations shown in this thesis. Thank you for the hours spent teaching me how to transfer nanowires with a nanomanipulator onto waveguides. Thank you Dr. Philip J. Poole for growing all the nanowires analyzed in this thesis. Thank you Dr. Robin L. Williams for all his sage advice and patience in explaining difficult concepts to me. Thank you Dr. Khaled Mnaymneh who drew the layout of the LIGENTEC chips used for this thesis. I would also like to thank him for patiently teaching me how to measure loss through waveguides.

I would like to thank those at NRC for all the great conversations during coffee break.

Lastly, I thank my parents for raising me and giving me the freedom to pursue graduate studies. I also thank my friends and sister who stayed with me everyday on Discord as we each worked from home during this pandemic. I would like to thank Dr. Jaewoo Park for being a loving, supportive boyfriend whose smiles were a great source of encouragement for me.

This thesis is dedicated my best friend,

who encouraged me to pursue a master's degree years ago
and shaped me into the person I am today.

I will always miss you.

Table of Contents

List of Tables

List of Figures

Nomenclature

η	source efficiency
η_{coll}	collection efficiency
η_{IQE}	internal quantum efficiency
$\|\alpha\rangle$	coherent state
$\beta_{\text{HE}_{11}}$	coupling efficiency into HE_{11} mode
γ	emission into other modes
$\Gamma_{\text{HE}_{11}}$	spontaneous emission rate in HE_{11} mode
θ_m	angle at which wave is travelling
b	annihilation operator for photon in a cavity mode
$b^\dagger$	creation operator for photon in a cavity mode
D_{dot}	diameter of quantum dot
$g^{(1)}(\tau)$	first-order correlation function
$g^{(2)}(\tau)$	second-order correlation function
H_{dot}	height of quantum dot
L	length of the waveguide
N_R	Number of reflections from each surface of a waveguide
t_g	thickness of the waveguide
CW	continuous wave
FSR	free spectral range
HeNe	helium-neon laser
HOM	Hong-Ou-Mandel

HWP half-wave plate

InAs indium arsenide

InAsP indium arsenide phosphide

InP indium phosphide

LPCVD low-pressure chemical-vapor-deposition

micro-PL micro-photoluminescence

PL Photoluminescence

QD quantum dot

SA-VLS selective-area vapour-liquid-solid epitaxy

SEM scanning electron microscope

TE mode transverse electric mode

TM mode transverse magnetic mode

TPI two-photon interference

WZ wurtzite InP crystal phase

X neutral exciton

X^- negatively charged exciton

XX biexciton

ZB zincblende InP crystal phase

ZPL zero-phonon line

Chapter 1

Introduction

Photons make up the smallest unit of energy of a quantized electromagnetic field. Particularly, single photons are important for quantum information technologies, quantum sensing, and certain implementations of quantum computation[64]. For example, quantum key distribution[14], a quantum cryptography protocol used in sending encrypted messages between two parties, demands a stable source of pure single photons in order to ensure the security of the network from eavesdroppers.

An ideal single photon source generates single coherent photons that are indistinguishable over long time scales and available at high repetition rates. A bright source will generate a fast stream of photons thus allowing for more complex computations; a source with high single photon purity will only contain one photon in each wave packet and no multi-photon emissions; a coherent source will generate photons with a stable phase; indistinguishable photons are identical in all aspects which is key in low-error rate quantum computation. Additionally, to be useful for quantum information sciences, a single photon source should ideally also be deterministic or "on-demand" meaning one should be able to control when a photon is emitted at some user-defined arbitrary time.

Many emerging technologies and research focus on developing quantum telecommunication networks. As such, the development of quantum information technology demands quantum light sources that can also easily couple into fibre and travel long distances while maintaining their single photon purity. A single photon available in optical modes with high overlap to Gaussian modes is needed to provide efficient coupling into optical fibres.

1.1 Introduction to single-photon generation

Single photons can be generated through both deterministic and probabilistic sources. Deterministic sources of single photons include colour centres, semiconductor quantum dots, mesoscopic quantum wells, single atoms, single ions, single molecules, and atomic ensembles. Each of these sources require some excitation energy followed by an emission of a photon of particular energy upon relaxation to a lower energy state. Probabilistic sources

of single photons involve the creation of pairs of photons where one photon heralds the creation of the other photon. This is achieved through either parametric down-conversion or four-wave mixing in a non-linear medium [19]. In the case of parametric down-conversion, a single laser photon is split into two photons, each carrying half of the initial laser photon's energy. Due to the probabilistic nature of this process, it is not possible to produce both a high probability of photons and have a high single-photon purity [28, 75]. This process operates in a low efficiency regime to mitigate two-photon events. Due to this lower efficiency, an on-demand single-photon source is more desirable for quantum communication applications.

Although sources such as single atoms, single molecules, or single ions have well-defined emission spectra, semiconductor quantum dots are of particular interest due to the ability to fabricate dots with desired emission wavelengths using standard semiconductor fabrication techniques. Moreover, temperature, strain, and an applied electromagnetic field can also be used to tune the emission of a semiconductor quantum dot.

1.2 Semiconductor single-photon sources

Semiconductor quantum dots (QD) spatially confine carriers on the order of nanoscale dimensions. Discrete energy levels similar to the level scheme found in atoms arise as a result of this confinement. As such, quantum dots are sometimes referred to as "artificial atoms". Like atoms, carriers can be injected either optical or electrically. In this thesis, we focus on generating carriers optically with lasers.

A common fabrication technique for producing epitaxial semiconductor quantum dots involves the random nucleation on a substrate[102]. The collection efficiency from these dots are not ideal due to the high index of refraction of the quantum dot compared to their surrounding (typically air). Total internal reflection limits the amount of light that manage to escape from the dot, and even less so is collected by the objective. To combat this, there has been much research into embedding these quantum dots into other devices such as a microcavity or nanowire waveguides [29, 32] to produce bright, efficient sources [34].

1.3 Hybrid integration of quantum dots in nanowires on photonic integrated circuits: Outline of thesis

Silicon photonics has been a promising route for integrating nano-electronic circuits with photonic and opto-electronics on chip. However, due to the indirect band gap and low optical gain of silicon [108], it is an unsuitable candidate for use as an efficient light source. Instead, recent research has focused on integrating III-V semiconductors on silicon [15].

In this thesis, we develop a way to integrate nanowires embedded with quantum dots on photonic integrated circuits. The nanowires were grown with a bottom-up approach

on a patterned substrate allowing for easy selection with a nanomanipulator probe. The nanowires were then transferred onto a chip containing photonic integrated circuits of interest. The single photon purity and high brightness of the quantum dots are maintained even after transfer onto another chip. This preliminary study on nanowires on simple SiN ridge waveguide structures paves the way for integration onto more complicated structures and allow for a stable, compact, on-the-go device.

A brief background on the different sources of light with particular attention towards semiconductor quantum dot light sources is given in **Chapter 2**. The experimental details of the setups used is described in **Chapter 3**. This chapter also discusses the growth process used to obtain the quantum dots in nanowires, the basic structure of the ridge waveguides on chips, the experimental procedures used to analyze the optical properties of the quantum dot emissions, and finally the "pick and place" method used to transfer nanowires from their growth substrate to a chip containing ridge waveguide structures. The results of the optical properties of quantum dots characterized both on their growth substrate and after transfer to ridge waveguides is discussed in **Chapters 4 & 5** respectively. These measurements aim to characterize the photoluminescent properties of the quantum dots, the efficiencies of the individual systems, lifetimes of quantum dot excitonic complexes, and single photon purity. Additional indistinguishability measurements taken for a nanowire on a ridge waveguide structure are also presented in the latter chapter. Further characterization on a more complex photonic integrated circuit containing ring resonators is shown in **Chapter 6** followed by a summary of the results in this thesis and future research outlooks.

Chapter 2

Background

The emission of light continues to be a fascinating and important area of research due to its prominence in a wide range of technologies. Coherent laser light and thermal light from a blackbody source (such as an incandescent light bulb) are both considered "classical" sources of light. There are also "non-classical" sources of light which include squeezed states, photon-number Fock states, and single-photon states [77]. Here, we are interested in single-photon states due to their usefulness in quantum technology applications. In this chapter, we provide a brief background on quantum light and its relation to quantum dots—particularly single-photon generation from quantum dots. We discuss the necessary parameters to maximize the efficient coupling of light emitted from a quantum dot through a nanowire waveguide. Finally, through simulations, we show the potential of coupling nanowire-quantum dots with SiN ridge waveguides.

2.1 Quantum Light

In quantum mechanics, light is described both as an electromagnetic wave and as a stream of particles known as photons. In this field, coherent states $|\alpha\rangle$, also known as Glauber states, were introduced to describe the quantum light theory of laser light. Glauber expressed $|\alpha\rangle$ as an eigenstate of the annihilation operator $\hat{a}$, so that $\hat{a}|\alpha\rangle = \alpha|\alpha\rangle$ where α is the complex amplitude of the optical electric field [48]. It is also useful to describe light in terms of Fock states (photon-number states $|n\rangle$) such as $|0\rangle$ which is a special case of a coherent state in vacuum. In the classical description, the vacuum state means that there is nothing, but in the quantum mechanical definition, it is the lowest possible energy level (i.e. photon count is zero). A coherent state can be described as a superposition of Fock states $|n\rangle$ [42]

$$|\alpha\rangle = e^{-\frac{|\alpha|^2}{2}} \sum_{n=0}^{\infty} \frac{\alpha^n}{\sqrt{n!}} |n\rangle \tag{2.1}$$

where $\alpha = |\alpha|e^{i\theta}$ in the polar form and θ is the phase [46]. Due to the uncertainty principle, Fock states, which are energy eigenstates of determined energies $E_n = \hbar\omega(n + 1/2)$, have

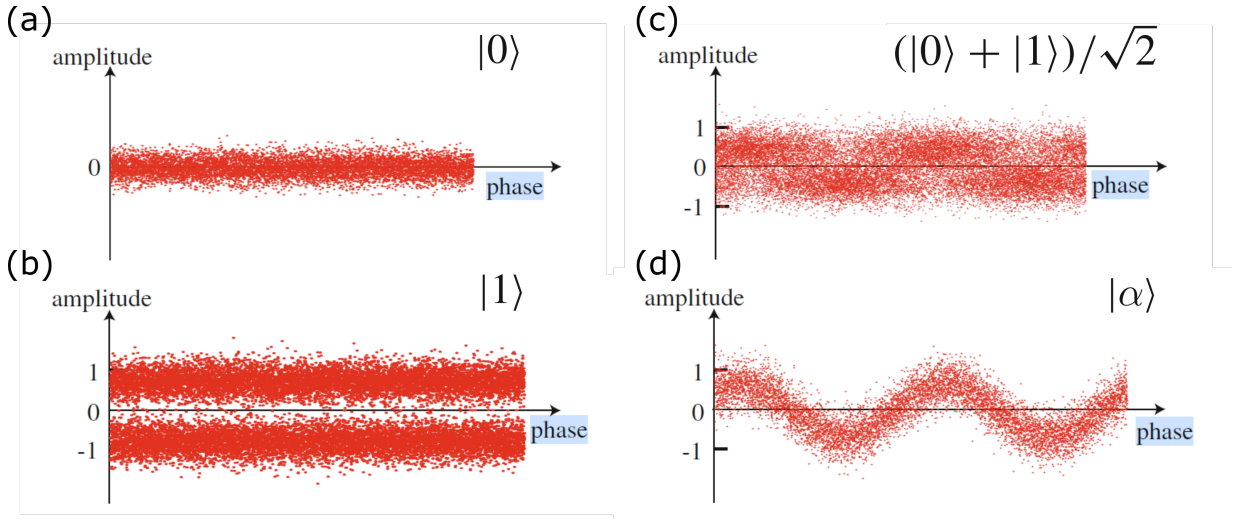

Figure 2.1: **Phase dependence of amplitude** for (a) the vacuum state $|0\rangle$, single-photon state $|1\rangle$, (c) a superposition of a vacuum $|0\rangle$ and a single-photon $|1\rangle$ so that $(|0\rangle + |1\rangle)/\sqrt{2}$, and (d) a very weak laser light $|\alpha\rangle$. Adapted from Furusawa, A. (2015). *Quantum states of light.* Springer [42].

fully undetermined phases. However, a superposition of the states reveal their wave nature in a coherent state.

To show the time-dependence of a coherent state, a balanced homodyne measurement can be taken using a measured light beam and a local oscillator. Figure 2.1 shows the resulting phase dependence of the amplitude for various states. A coherent state, such as laser light, exhibits a wave-like structure similar to the theoretical plot of the time dependence of the real and imaginary part of coherent light. Figure 2.1(d) shows the amplitude versus phases of very weak laser light. In a vacuum state $|0\rangle$, the energy is determined to be $E_0 = \hbar\omega/2$, thus resulting in no change as a function of the phase as shown in 2.1(a). Similarly, a single photon state $|1\rangle$ has energy $E_1 = 3\hbar\omega/2$ and again no change in the amplitude as a function of the phase (see 2.1(b)). Mixing those two states incoherently will yield a plot of amplitudes with no obvious change as a function of the phase. However, a superposition of the two states $(|0\rangle + |1\rangle)/\sqrt{2}$ reveals a periodic pattern in the amplitude as a function of phase (see Figure 2.1(c)). Conversely, a superposition $(|0\rangle - |1\rangle)/\sqrt{2}$ yields a similar graph, except the plot is flipped along the x-axis. Higher photon-number terms are needed to obtain an even clearer sinusoidal wave structure described by Eq. (2.1) and shown in Figure 2.1(d).

From this understanding of coherent states, light can be further classified into squeezed states, single-photon states, and entangled states which are understood to be some superposition combination of Fock states [42]. Of these, single-photon states are of particular interest and best represent the particle nature of light. Single-photons are represented as state $|1\rangle$ and will always have a count of 1. Over the years, the number of applications requiring single-photons have grown as the field of quantum information technology has expanded.

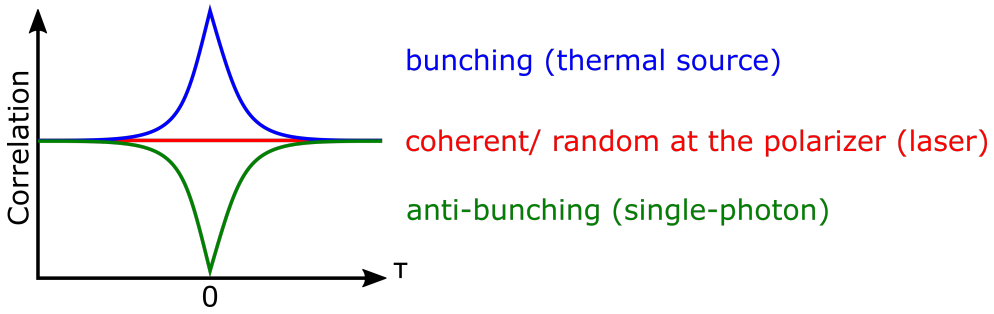

Figure 2.2: Possible outcomes of second correlation function $g^{(2)}(\tau)$.

2.2 Thermal sources, laser sources, and single photon sources

The correlation properties of photons are useful for characterizing different types of light such as classical (thermal and laser) or non-classical (single-photons) light. This concept was first introduced by Glauber [48] who described this correlation in terms of a quantum field measured at four different times. For us, we are only interested in the time at which a photon is emitted, t_1, and the probability of another photon being emitted at t_2 [76]. A zeroth-order correlation gives the intensity $\langle n \rangle$, and the normalized first-order correlation function describes the field-amplitude correlations as measured with a Michelson interferometer. The degree of coherence of the photons, $g^{(1)}(t,\tau)$, is described by

$$g^{(1)}(t,\tau) = \frac{\langle b^\dagger(t) b(t+\tau) \rangle}{\langle b^\dagger(t) b(t) \rangle}, \tag{2.2}$$

where $b^\dagger$ and b are creation and annihilation operators for photons in a cavity mode.

The second-order correlation $g^{(2)}(\tau)$, or intensity correlation function, is given by

$$g^{(2)}(t,\tau) = \frac{\langle b^\dagger(t) b^\dagger(t+\tau) b(t+\tau) b(t) \rangle}{\langle b^\dagger b(t) \rangle \langle b^\dagger(t+\tau) b(t+\tau) \rangle}, \tag{2.3}$$

and gives information on the statistical properties of the radiation. In a stationary situation where time is invariant, we can omit t because we are only interested in the delay τ between the emission times of two photons. The correlation at zero time delay, $g^{(2)}(\tau = 0)$, allows us to characterize the three types of possible light sources as shown in Figure 2.2. Thermal radiative sources will produce a $g^{(2)}(0) = 2$, indicating a high likelihood of finding two photons at the same time. Coherent radiative sources such as ideal lasers obey Poisson statistics and give a $g^{(2)}(0) = 1$. Noise in the system arises from the randomness of spontaneous emission. Finally, for non-classical light, the intensity autocorrelation gives $g^{(2)}(0) < 1$. Typical autocorrelation measurements are conducted using a Hanbury Brown and Twiss experiment[20]. More detail will be given on the experimental setup in Section 3.4.4.

2.3 Optical Properties of Quantum Dots

Quantum dots can be reliable sources of quantum light. Unlike probabilistic methods of single-photon generation such as parametric down-conversion, quantum dots provide on-demand single-photons upon excitation by some external energy. This is important for certain applications of quantum cryptography which require a fast, bright, deterministic, indistinguishable stream of single photons.

2.3.1 Types of Quantum Dots

There are several types of quantum dots including gate-defined [3, 103], colloidal [50], and epitaxial [13, 88]. Each type is shown in Figure 2.3.

Lateral, gate-defined quantum dots use electrostatically tunable barriers to define the quantum dot, usually made of GaAs/AlGaAs [24, 103] or InAs/InP [92] heterostructures. Gate-defined quantum dots rely on the quantum tunneling of electrons and utilize voltage gates to control the number of free electrons at the site. Depending on the voltage applied, the quantum dots can be squeezed from 500 nm to 0 nm, thus reducing the number of free electrons allowed to pass. Typically, the gate is used to modulate the potential in an underlying, enclosed two-dimensional electron gas in order to isolate charges [37].

Colloidal quantum dots are nanoscale semiconductor particles synthesized in solutions and have been extensively studied in the field of chemistry. When asked what a quantum dot is, one is likely to recall the image of a row of brightly coloured vials against a black background. These brightly coloured vials contain colloidal quantum dots emitting at different wavelengths due to the differences in their sizes. A common method for making colloidal quantum dots involves a heating process that promotes the formation of nanocrystals and is stabilized with solubilizing ligands (see Figure 2.3(b)(left)). The size of these colloidal quantum dots is controlled through their growth process. Common uses of colloidal quantum dots include biological tags [21], LED devices [2], and photovoltaic devices such as solar cells [39]. Much like the dyes used in dye-sensitized solar cells, colloidal quantum dots can also be used to coat the titanium dioxide layer necessary for facilitating transport of electrons across the solar cell matrix after excitation from an external light source [82]. An example of colloidal quantum dots dried and packed into a hexagonal array is shown in Figure 2.3(b)(right).

Lastly, epitaxial quantum dots are any quantum dot grown through epitaxial means (i.e. nanocrystals grown on a substrate). The conventional way to achieve epitaxially grown quantum dots is through self-assembly using a Stranski-Krastanov growth mode [102, 9] where a thin film of the same material as the quantum dot, typically of a III-V or II-IV semiconductor material, is deposited onto a substrate atomic monolayer by monolayer to form the wetting layer. As layers are added, quantum islands begin to form due to the strain from the lattice mismatch between the substrate and the wetting layer. These islands make up the basis for the quantum dot. Another more recent method is droplet epitaxy quantum dots which uses the formation and crystallization of metallic droplets on a substrate. In this process, the group III droplet, such as indium (In) or gallium

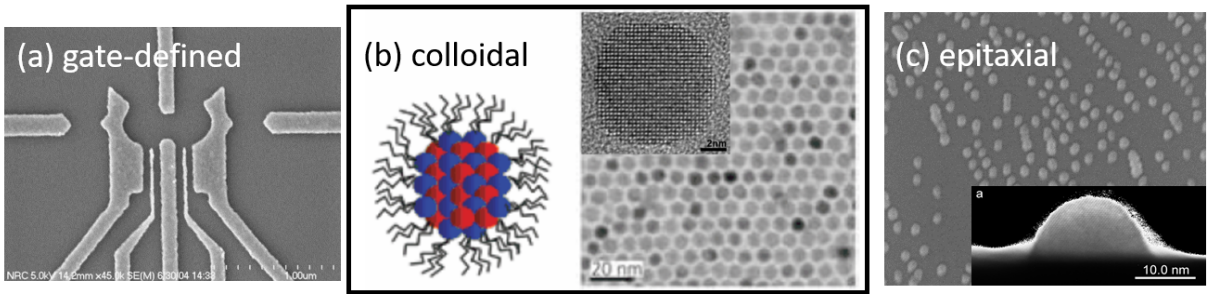

Figure 2.3: **Types of quantum dots.** (a) SEM of a gate-defined quantum dot. (b) Schematic of QD nanocrystal core surrounded by solubilizing ligands (left) and TEM (right) of colloidal quantum dots dried and packed in an hexogonal array. Adopted from Guyot-Sionnest, P. (2007). *Quantum Dots: An Emerging Class of Soluble Optical Nanomaterials* (Vol. 2). Material Matters [50]. (c) SEM of epixially grown quantum dots on a substrate. Inset shows cross sectional TEM of an epixially grown quantum dot.

(Ga), is first introduced to the substrate. The size of the droplets can be well controlled by adjusting the flux of the group III material into the system. Using a group V rich environment such as arsine (As), the droplets crystallize to form the quantum dots [44].

In both these methods, the quantum dots are distributed randomly on the surface of the substrate with varying sizes as seen in Figure 2.3(c). A cross-section of one such dot is also shown in the inset. These dots are typically flat and strongly confined in the vertical direction. The horizontal radius of the dot can range from 10 nm to tens of nanometers [13]. For a quantum dot in free space, it is able to emit in all directions. However, the collection of light from dots grown in this method is not ideal since the quantum dot emitter is typically clad in a high index material. The large difference in the index of refraction between the cladding material and air causes total internal reflection to occur. Therefore, if light is emitted at an angle greater than the critical angle with the normal, the light is reflected back down and cannot escape the material. This is shown later in Figure 2.9(a). The fraction of emission that manages to escape the material is estimated to be $1/4n^2$ where n is the refractive index of the material [8]. For perspective, that means for an InP quantum dot ($n = 3.362$ at 953 nm), no more than 2% of the photons are able to escape. In reality, this number is even less because the collection is also dependent on the numerical aperture of the lens used in the system.

2.3.2 Quantum confinement

Quantum dots are the physical realization of the particle in a box. The quantum dot confines carriers (electrons and holes) in three-dimensions. These carriers form quasi-particles called excitons (bound electron-hole pairs), and the confinement is on the order of the exciton Bohr radius. As the size of the quantum dot decreases, the confined energy levels that the carriers occupy move further apart. Using the illustration of a particle in a

box, the energy levels can be described by

$$E_n = \frac{n^2\hbar^2\pi^2}{2mL^2} = \frac{n^2h^2}{8mL^2}, \tag{2.4}$$

where m is the mass of the particle in the box, L is the length of the box, and n is a discrete energy level. From Eq. (2.4), it can be seen that as L decreases, the relative difference between the energy levels also increases. An example of how the energy levels change with varying lengths is shown in Table 2.1.

L	$n=1$	$n=2$	$n=3$
0.5	$4E_1^*$	$16E_1^*$	$36E_1^*$
1	$E_1^* = \frac{h^2}{8m}$	$4E_1^*$	$9E_1^*$
2	$\frac{1}{4}E_1^*$	E_1^*	$\frac{9}{4}E_1^*$

Table 2.1: Discrete energy levels for particle in a box.

From the table, it can be seen that the levels have an energy 4 times greater just by reducing the size of the box by half. Similarly, this increase in the spacing between energy levels is seen in quantum dots as the size of the quantum dot is reduced. These discrete energy levels mirror that of an atom. As such, quantum dots are sometimes referred to as "artificial atoms."

For a semiconductor quantum dot, confinement is achieved by placing a small band gap semiconductor (quantum dot) in a larger band gap host material. Assuming a parabolic confining potential, one obtains energy levels given by [30]

$$E = (n_x + n_y + 1)\hbar\omega_0 + \left(\frac{\pi^2\hbar^2}{2m^*L^2}\right) n_z^2, \tag{2.5}$$

where n_x and n_y are integers ≥ 0, n_z is an integer ≥ 1, L is the height of the quantum dot, ω_0 is the energy-level spacing, and m^* is the effective mass of either the electron or the hole.

Populating these levels with carriers and subsequent recombination leads to emission of photons with energies given by [74]

$$E_x = E_e + E_h - V_{eh}, \tag{2.6}$$

where E_e and E_h are defined by Eq. (2.5) with its respective effective masses, and V_{eh} accounts for the Coulomb interaction between the carriers (i.e. for a single electron-hole pair, the exciton binding energy).

In this thesis, we focus on indium arsenide phosphide (InAsP) quantum dots in bulk indium phosphide (InP) nanowires. Bulk InP has a band gap of 1.34 eV at 300 K. Bulk indium arsenide (InAs) has a band gap of 0.354 eV at 300 K. Since InP has a much larger band gap than InAs, InAs makes a good candidate as a quantum dot in a bulk InP material.

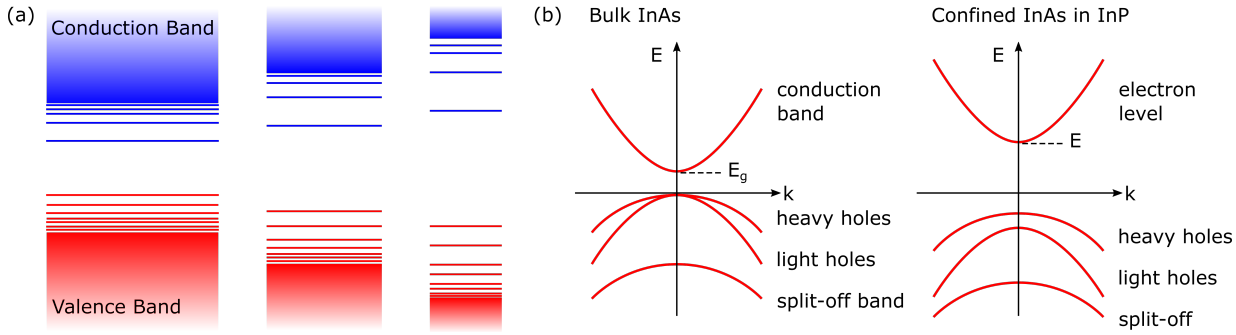

Figure 2.4: **Confinement of a quantum dot.** (a) Schematic of quantum confinement effects. The spacing between discrete energy levels increases with decreasing size. (b) E-k diagram of bulk InAs (left) and confined InAs in InP (right).

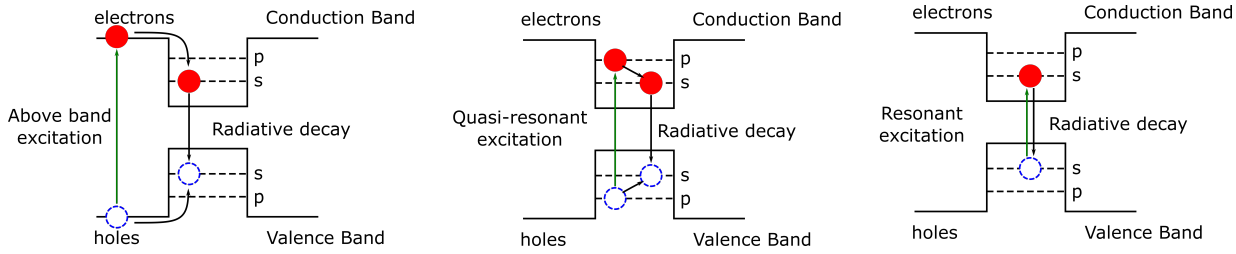

Figure 2.5: **Excitation regimes.** Above-band excitation, quasi-resonant excitation, resonant excitation

The band gap of the quantum dot (see Figure 2.4(a)) is determined by the bulk band gap of the dot material (see Figure 2.4(b)(left)) which will depend on the composition of the dot and the lattice mismatch-mediated strain between the dot material and the host material (also dependent on composition). We note that for strong confinement in the growth direction, the degeneracy of the heavy-light hole bands is removed (see Figure 2.4(b)(right)) with the heavy hole band forming the ground state. In this thesis, we are only concerned with the heavy hole band. The above is a very simplified picture of the electronic structure of a quantum dot. For a more realistic model, see Ref. [31].

Excitation regimes for quantum dots in nanowires

The quantum dot levels can be populated with carriers using both optical and electrical methods. Here, we only discuss optical excitation. Optical injection of carriers in the quantum dot can be done in several ways including above-band excitation, quasi-resonant excitation, and resonant excitation.

In above-band excitation, the nanowire is pumped with light of energy either equal to or greater than the band gap of the bulk InP nanowire (see Figure2.5 (left)). This is achieved with a laser of $\lambda \leq 832\,\text{nm}$ (i.e. the band gap of wurtzite InP). An electron is promoted from the bulk InP valence band to the conduction band creating an electron-hole pair, both free to diffuse throughout the material. The electron-hole may recombine directly in the InP bulk material or find lower energy states to relax into (i.e. become trapped). Carriers

would rather be in the lowest energy state possible, so preference is given to relaxing into the potential well of the InAsP quantum dot which is of much lower energy than that of the bulk InP material as mentioned above. Like the discrete energy levels of an atom, we describe the energy levels of the quantum dot as the s-shell, p-shell, d-shell, etc. When the electron and hole relax to the s-shell of the InAsP quantum dot, they can recombine and emit a photon with energy given by Eq. (2.6). The excess energy from the relaxation of the carriers from higher orbitals to the s-shell is emitted into the solid state environment as phonons. Similarly, for excitation energies greater than the band gap of InP, relaxation to the InP band edges (thermalization) occurs through the emission of phonons.

In quasi-resonant and resonant excitation, the excess energy is chosen to be resonant with one of the energy levels of the quantum dot. If for example, the excitation was resonant with one of the p-shells of the quantum dot, an electron from the p-shell of the valence band will jump into the p-shell of the conduction band. Due to symmetry, only recombination of electrons and holes in the same shells is possible. For example, electrons in the p-shell can only recombine with a hole in the p-shell, and an electron in the s-shell can only recombine with a hole in the s-shell [76]. An electron in the p-shell of the conduction band can, however, relax into the s-shell of the conduction band before it recombines with a hole in the s-shell. P-shell pumping is a good way to limit the effects of other interactions with the environment by limiting the relaxation to one or two processes (see Figure 2.5 (middle)) (i.e. it eliminates the thermalization process and does not flood the whole nanowire with carriers). When the excitation is resonant with the transition that produces photons to be measured, this is considered strictly resonant excitation (see Figure 2.5 (right)). If the electrons and holes relax into other lower energy states before emitting a photon of less energy in a multi-step process, then it is quasi-resonant excitation.

For excitation below the band gap of InP, if the excitation energy does not have the same energy as one of the discrete energy levels, it will simply not be absorbed (i.e. the material is transparent at that wavelength).

2.3.3 Photoluminescence

Photoluminescence (PL) occurs when light energy stimulates the emission of a photon in a material. In this work, most experiments are performed with above-band excitation shown again in Figure 2.6, for the specific case of an InAsP quantum dot in an InP bulk material. Without an external source providing extra energy, the electrons (and holes) will not be able to escape back into the bulk material. This is the case here since we are performing experiments at 4 K. As mentioned above, carriers are generated in the InP which then diffuse and can be trapped in the quantum dot. Subsequent relaxation to the ground state occurs over a few tens of picoseconds. The trapped electron-hole pair that form the exciton can then recombine and release the energy it had stored radiatively in the form of a photon. An excitonic lifetime is defined then by how long it takes for the exciton to recombine and emit. This lifetime is typically much longer than the non-radiative relaxation of the carriers to the ground state levels and is in the order of nanoseconds. This photoluminescence process is capable of producing single-photons (i.e. it can have a

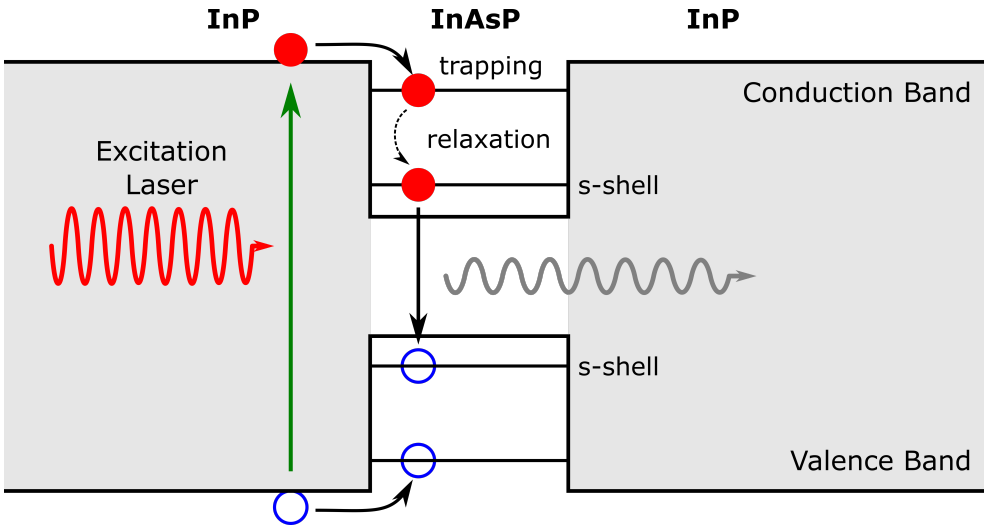

Figure 2.6: **Schematic of single-photon generation.** An excitation laser promotes an electron from the valence band to conduction band of a bulk InP material. Electron-hole pairs created in the bulk nanowire material travel towards the quantum dot and become trapped. When the electron and hole recombine, a photon is emitted.

zero probability of multi-photon emission). As such, it exhibits the anti-bunching property seen in Figure 2.2.

A more complete picture of all the emission processes that can occur in the InP/InAsP nanowire system, is shown in Figure 2.7(a). As well as quantum dot emission, we also observe band to band recombination from the wurtzite InP, recombination from donor-acceptor impurity levels, and recombination related to stacking faults (discussed in Section 4.1). A typical photoluminescence spectrum of an InP/InAsP nanowire using a 780 nm continuous-wave laser pumping above-band is shown in Figure 2.7(b). The figure shows the wurtzite at 832 nm. The emission at 875 nm due to zincblende InP is typically not observed or is very weak. Emission in the range of 832-875 nm is related to stacking faults and donor-acceptor levels. The emission from the quantum dot is observed around 980 nm for this sample. The emission wavelengths are summarized in Table 2.2.

Centre Wavelength (nm)	Source
832	Wurtzite band gap
840	Stacking faults in nanowire
860	Donor-acceptor band gaps
875	Zincblende band gap
930-980	Quantum dot emission

Table 2.2: Commons sources of peaks from an wurtzite InP nanowire with embedded InAsP quantum dot grown on an InP substrate.

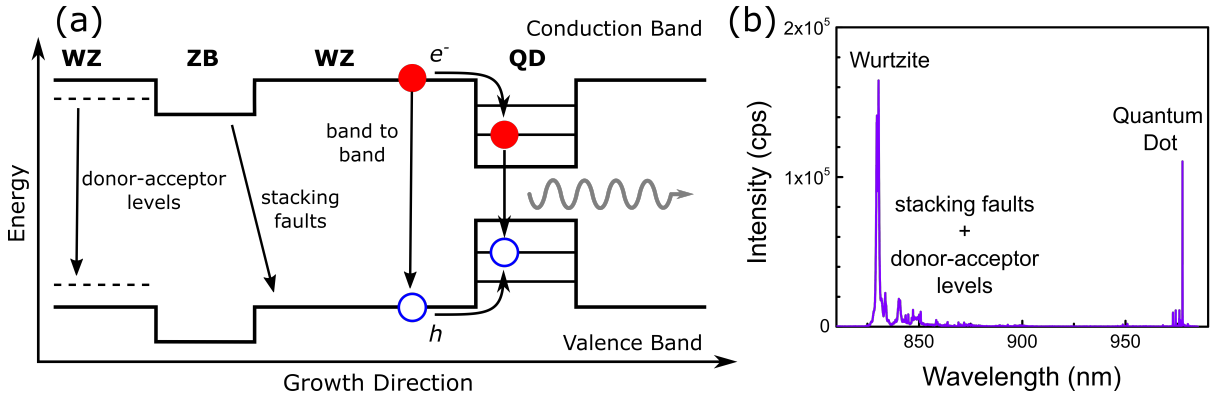

Figure 2.7: (a) Emission from an InP nanowire with an InAsP quantum dot including defects from stacking faults and donor-acceptor impurities. (b) A typical photoluminescence spectrum of a nominal nanowire-quantum dot.

2.3.4 Excitons, charged excitons, and biexcitons

Finally, we discuss the different emission lines that may be present in the s-shell due to different charge and spin configurations. It is useful to think of the spin states of the particles in terms of their angular momentum $|J, J_z\rangle$. In a quantum dot, the complexes of interest happen at the lowest energetic level, so in this section, we will only be discussing heavy holes. The following are the spin states for the electron and heavy holes, which are typically the lowest energy level in a quantum dot:

$$\begin{aligned} |e,\uparrow\rangle &= \left|\frac{1}{2},+\frac{1}{2}\right\rangle; |e,\downarrow\rangle = \left|\frac{1}{2},-\frac{1}{2}\right\rangle \\ |h,\Uparrow\rangle &= \left|\frac{3}{2},+\frac{3}{2}\right\rangle; |h,\Downarrow\rangle = \left|\frac{3}{2},-\frac{3}{2}\right\rangle \end{aligned} \tag{2.7}$$

Excitons trapped in a quantum dot may have four different spin states along the growth direction. The total angular momentum basis of the exciton state is

$$\begin{aligned} &|e\uparrow, h\Downarrow\rangle \text{ and } |e\downarrow, h\Uparrow\rangle \\ &|e\uparrow, h\Uparrow\rangle \text{ and } |e\downarrow, h\Downarrow\rangle \end{aligned} \tag{2.8}$$

Only states with a total angular momentum of ± 1, such as the ones in the first row, emit light in what is called a "bright" exciton. States with a total angular momentum of ± 2 do not emit a photon and are referred to as "dark" states. These have parallel spin states such as those in the second row of Eq. (2.8). They are considered optically inactive unless one of the spins eventually flip thus allowing for recombination to occur [76]. Figure 2.8 shows the possible excitonic complexes at the lowest energy level (s-shell) that produce a photon upon recombination. In this figure, we show three different types of excitonic complexes, a neutral exciton X consisting of a single electron-hole pair, a biexciton XX consisting of two electron-hole pairs, and charged complexes $X^{+/-}$ consisting of a single electron-hole pair plus an additional carrier. Recombination of a single electron-hole pair

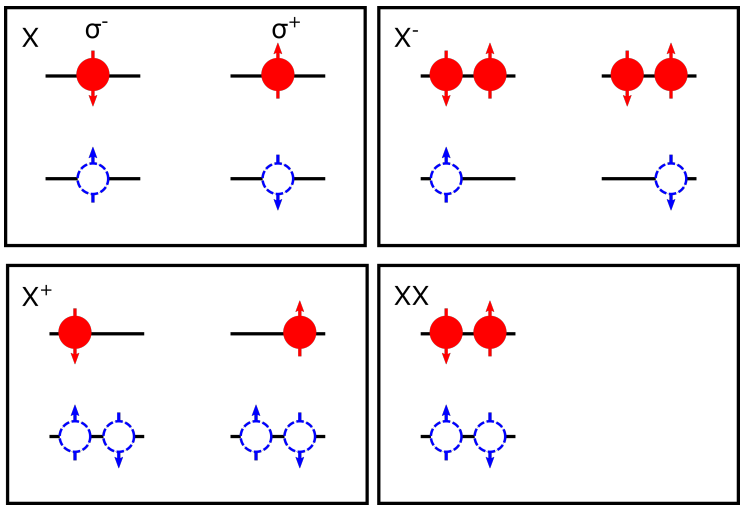

Figure 2.8: **Excitonic complexes of "bright" states.** Top-left: neutral exciton, top-right: positively charged exciton, bottom-left: negatively charged exciton, bottom-right: biexciton

in any of these charge configurations produces a photon with a distinct emission energy. This will be further discussed in the Section 4.3.

2.4 Efficiency

We mentioned previously for a flat epitaxial InAs quantum dot, less than 3% of emitted photons is collected from the quantum dot (See Section 2.3.1 and Figure 2.11(a)). To force the light emitted from a quantum dot to emit in a particular direction, the physical environment of the quantum dot needs to be altered. We can mediate this problem of collection efficiency by incorporating the quantum dot into different structures such as 3-D cavities (e.g. micropillars, photonic crystals) or waveguide structures (which can also be photonic crystals, but also beams, and nanowires).

Not only do we want to generate single photons, but we also want the single photons to be in a mode compatible with the single-mode of an optical fibre. A structure encasing the quantum dot can be tailored to provide the necessary mode that will couple well into an optical fibre. In 1987, Yablonovitch [109] proposed the use of micro-cavities to maximize the collection efficiency from a quantum dot. A 3-D photonic crystal is used as a perfect mirror and tailored defects within the crystal act as the cavity. This ideal photonic box provides 3-D confinement of the light and forms a discrete series of confined modes. If the modes are well separated, then the cavity can be designed to support only a single mode into which the dot emission can efficiently couple.

The micropillar cavity consists of two distributed Bragg reflectors made of high index and low index materials stacked on top of each other sandwiching a layer of continuous spacer material [81] as shown in 2.9(b). The stacks above and below this spacer act as mirrors. Total internal reflection due to the difference in refractive index between the spacer

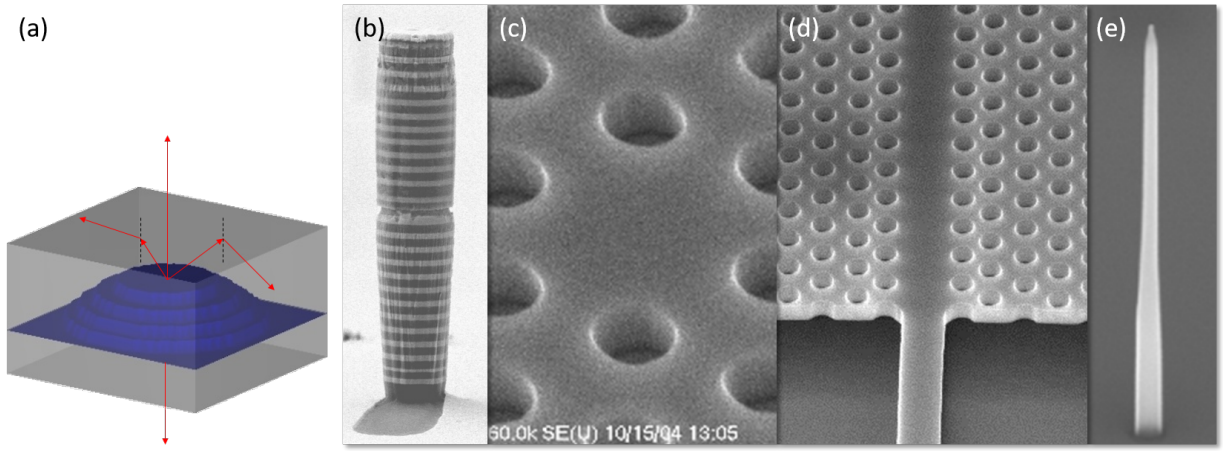

Figure 2.9: (a) Schematic Stranksy-Krastonow quantum dot emission. (b) SEM of micropillar cavity (c) SEM of photonic crystal cavity (d) SEM of photonic crystal waveguide (e) SEM of nanowire waveguide

and vacuum surrounding the pillar also makes the walls of the material act as mirrors. These mirrors confine the light three-dimensionally within the micropillar. In order for the emitter to couple well into the system, there needs to be good spectral and spatial matching. We want the light leaving the cavity to overlap well with a Gaussian beam shape for efficient coupling into optical fibres, detectors, and other optical components [83]. One study has shown that a micropillar micro-cavity can offer a collection efficiency of $\sim 70\%$ [8].

Photonic crystal cavities work in a similar fashion. Except, instead of a stack of high and low index materials that make up the Bragg reflectors, patterned holes are etched into a high index material. In this case, the low index material is either vacuum or air. If a hole is missing from this matrix (see Figure 2.9(c)), then it acts in a similar fashion to the section of continuous material between the two Bragg reflectors of the micropillar thus forming the cavity.

Removing an entire row of holes, such as the one shown in Figure 2.9(d), forms a photonic crystal waveguide [99]. The two sections with holes act as side mirrors on either side of the hole-less strip. Generated single photons from the quantum dot are guided along the waveguide and collected at the exit. A coupling efficiency of $98.43 \pm 0.04\%$ has been achieved for a quantum dot coupled to a photonic crystal waveguide [5].

Similarly, if we replace the two stacks of Bragg gratings with a continuous material, we arrive at the nanowire (see Figure 2.9(e)). Note both the photonic crystal waveguide and nanowires do not rely on micro-cavities to confine the light from a quantum dot. The nanowires act as waveguides which direct light from the quantum dot along the length of the nanowire and prevent significant loss through their sidewalls.

The structures in Figure 2.9 represent two classes of devices. Micropillars and photonic crystal cavities confine light in three dimensions and can produce a single strongly localized optical mode. Such devices target lifetime reductions due to the Purcell effect which relates to controlling the available modes into which an emitter can emit [45]. High Purcell

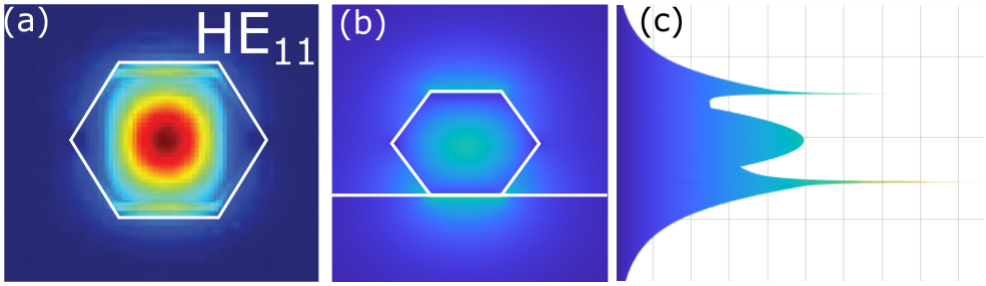

Figure 2.10: **Simulation of nanowire waveguide modes.** Intensity of the electric field is shown for (a) a free standing nanowire. Adapted from Bulgarini, G. (2014). Nanowire-based Quantum Photonics. [23]. (b) HE_{11} mode in the z-direction of a nanowire lying on a substrate (c) Intensity profile of the HE_{11} mode showing the profile of the mode and evanescent field at nanowire boundaries. Simulations courtesy of Dr. David B. Northeast.

enhancements of radiative lifetimes have been demonstrated with such devices [40], but this requires special attention to be made to spectral and spatial matching of the emitter and cavity mode [6].

The second class of devices represents structures based on propagating modes. For these structures, spectral matching tolerances are relaxed which allow for a broadband spectral range of a few meV allowing for the study of different spectrally distinct complexes within the nanowire. However, attaining a high Purcell enhancement in these structures however is not straightforward. They do allow for emitter-optical mode coupling efficiencies that approach 100%. For this reason, we focus on nanowire waveguides embedded with quantum dots for efficient coupling of light from the quantum dot.

2.4.1 Coupling efficiency of quantum dot to nanowire waveguide

To understand the coupling of light from one medium to another, we need to re-frame our understanding of light back into the classical definition where light is an electromagnetic wave. Electromagnetic energy is transmitted through waves and can propagate in either a medium or vacuum. A waveguide guides light through a medium that is spatially confined. If the wave propagation is confined in one-dimension (sandwiched between a material of lower refractive index called a cladding), then it is a planar waveguide. To gain a rough understanding of how waveguides work, it is useful to think in terms of ray optics. Due to total internal reflection between the high and low index mediums, the light cannot escape from the waveguide edges if the angle of incidence is greater than the critical angle $\theta_c = \arcsin(n_1/n_2)$.

If the waveguide is further confined in two dimensions, then it is a channel waveguide. In this latter case, the propagation is permitted only in one dimension. It is common to consider the electric field distribution at a perpendicular cross-section of the waveguide relative to the propagation direction, but some of these distributions do not change during propagation and make up waveguide modes. An example of a waveguide mode is shown in Figure 2.10(a) — a simulated HE_{11} fundamental mode of a free-standing hexagonal

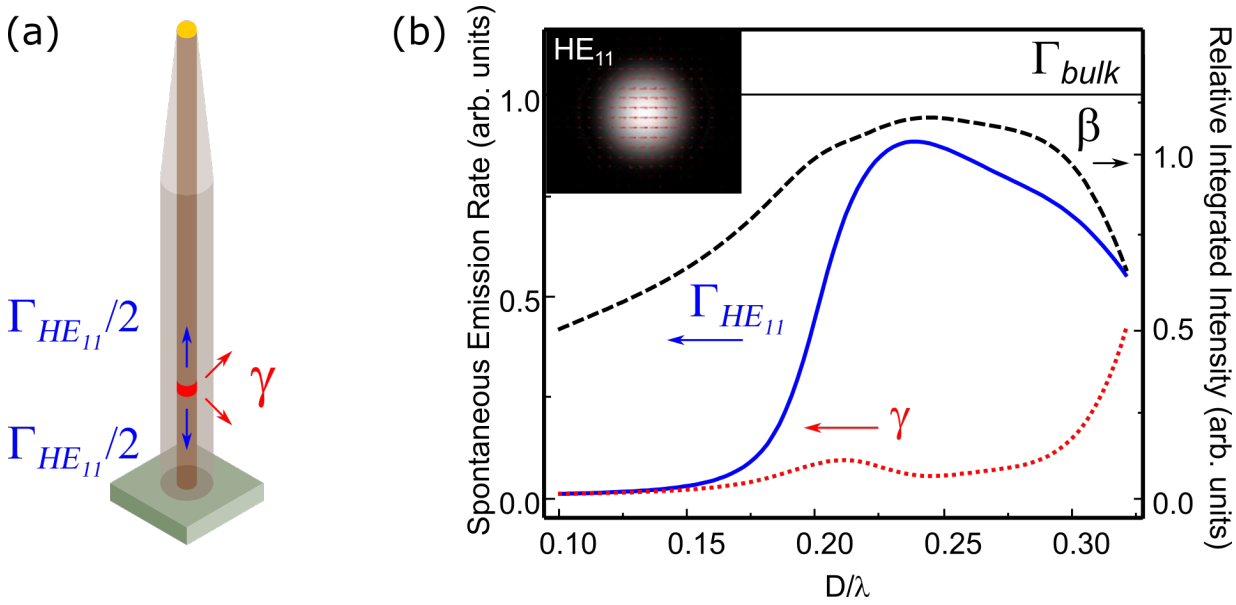

Figure 2.11: (a) Tapered nanowire showing emission into confined $\Gamma_{\mathrm{HE}_{11}}$ and leaky γ modes. (b) Calculated normalized spontaneous emission rates into each mode for an InP nanowire at $\lambda = 950$ nm. Inset shows the electric field intensity of the HE_{11} mode. Adapted from [34].

nanowire waveguide. There are two degenerate modes (i.e. they have the same effective index) typically labelled as HE_{11x} and HE_{11y}, both propagating through the hexagonal nanowire. This mode is maintained throughout the length of the nanowire of the same diameter and does not spread as much in the transverse direction as it would in vacuum [95].

We use nanowire waveguides to confine the modes in which the quantum dot can emit. The geometry of the nanowire has a strong effect on its efficiency as a single photon source, and therefore needs to be grown so that it can effectively couple the light emitted from the quantum dot through its shaft [34]. To determine how well quantum dot emission couples into the nanowire waveguide, we wish the determine the source efficiency, η, which is dependent on the percent of total photons collected by an external optical system (at first lens). One of the determining factors is the efficiency with which the emission of the quantum dot couples into an available photonic mode of a waveguide, β_{mode}. Since we are primarily interested in the coupling to the fundamental HE_{11} mode, we define the source efficiency to be

$$\eta = \alpha\beta_{\mathrm{HE}_{11}}\eta_{\mathrm{IQE}} \tag{2.9}$$

where $\beta_{\mathrm{HE}_{11}}$ is the fraction of photons the quantum dot emits into the HE_{11} mode. α is the fraction of those photons collected by the external optical system, and η_{IQE} is the internal quantum efficiency of the emitter. As shown in Figure 2.11 (a), half of the photons emitted in the HE_{11} mode couple upwards (towards the taper) and the other half downwards (towards the base), resulting in a maximum α of 50% collection from either end. This can be mitigated with a metallic mirror at the nanowire base [89]. However, we have not included this reflective surface at the base of our nanowires. The tapering of the nanowire

expands the HE_{11} mode and limits its divergence as it leaves the nanowire.

The HE_{11} mode coupling efficiency, $\beta_{HE_{11}}$, is dependent on the spontaneous emission rate into HE_{11}, $\Gamma_{HE_{11}}$, and into all other modes, γ, as follows:

$$\beta_{HE_{11}} = \frac{\Gamma_{HE_{11}}}{\Gamma_{HE_{11}} + \gamma}. \tag{2.10}$$

Figure 2.11(b) shows the calculated values of $\beta_{HE_{11}}$, $\Gamma_{HE_{11}}$, and γ for an InP nanowire as a function of the normalized diameter D/λ of the photonic nanowire (with a cladding of diameter D) with respect to bulk InP. These values are calculated at an operating wavelength of $\lambda = 950\,\text{nm}$ [41, 34]. The calculations assume the quantum dot is centered laterally in the nanowire, without which coupling to the HE_{11} mode will be less and thus decreasing the efficiency. The graph shows that a strong coupling efficiency $\beta_{HE_{11}} = 95\%$ for $D/\lambda \sim 0.24$ can be achieved. The sharp decrease in the spontaneous emission rate in $\beta_{HE_{11}}$ is due to having an overlap in the optical mode of the nanowire that is too small to couple with the quantum dot. To maximize the spontaneous emission rate, we want the maximum overlap of the optical mode without having a D/λ so large that it supports higher order modes. If higher order modes are allowed in the nanowire waveguide, then the quantum dot emission may couple into those higher order modes which may be harder to collect efficiently from.

Simply put, we know from Figure 2.11(b), the calculated coupling efficiency β is relatively high ($> 90\%$) for a wide range of normalized diameters D/λ. This gives a lot of play in choosing the diameter for the design of the nanowire. However, not all the normalized diameters in this range will give a good spontaneous emission rate relative to the bulk. Notice where $D/\lambda < 0.22$, the spontaneous emission rate $\Gamma_{HE_{11}}$ is low despite the high calculated β. On the other hand, if we design the nanowire waveguide to have $D/\lambda > 0.28$, though $\Gamma_{HE_{11}}$ is still high, there is more loss into leaky modes γ. From the plot, $D/\lambda \sim 0.24$ appears to be the sweet-spot for maximizing both the coupling efficiency and spontaneous emission rate with minimal loss into leaky modes [34].

We have just described the ideal conditions for growing nanowire waveguides maximized for quantum dots emitting at 950 nm with high coupling efficiency. We wish to incorporate these nanowires with other waveguide structures. From our simulations of the HE_{11} mode, we define the leaking of the electric field outside the waveguide as the evanescent field which is important for coupling into other waveguides. It is formed when the waves travelling through the waveguide undergo total internal reflection at the waveguide boundaries as it strikes the walls with an angle greater than the critical angle θ_c and can thus escape. The field that is in the other medium (vacuum, other waveguide, or substrate) is known as the evanescent tail. Evanescent coupling occurs when the evanescent tails of two waveguide modes overlap.

Figure 2.10(b) shows the z-direction of the electric field intensity of a nanowire on a substrate in vacuum. An intensity profile of the HE_{11} mode (see Figure 2.10(c)) shows the field profile of the mode at the centre of the nanowire waveguide. The discontinuity at the boundaries are more evident in this side profile. The evanescent tail is clearly seen at the boundary between the substrate and nanowire (bottom). This tail is important for

the efficient coupling of the nanowire mode into other waveguide structures of interest on a photonic integrated circuit.

2.5 Photonic integrated circuits on chips

So far, we have covered photonic crystal and nanowire waveguide structures. Another type of waveguide structure of interest is the ridge waveguide which is a rectangular slab of dielectric material that guides light along its length. Due to its rectangular cross-section, we no longer define the mode in terms of the HE_{11} fundamental mode like in a waveguide with a circular or hexagonal cross-section. Instead, we look at the different types of waves corresponding to the different elements within the electromagnetic wave. There are two types of modes that can propagate through a rectangular waveguide, the transverse electric (TE) mode and transverse magnetic (TM) mode. The TE mode is characterized by the $\boldsymbol{E}$ field being traverse to the direction of propagation and the $\boldsymbol{H}$ field being perpendicular to the direction of propagation. Conversely, to TM mode is characterized by the $\boldsymbol{H}$ field being transverse to the propagation direction and the $\boldsymbol{E}$ field being perpendicular. As always, $\boldsymbol{E}$ and $\boldsymbol{H}$ are perpendicular to each other. Figure 2.12 shows simulations of the electric field intensities of the first two modes (TE0 (a) and TM0 (c)) and higher order modes (TE1 (b) and TM1 (d)) of a photonic ridge waveguide of dimension 800 nm by 485 nm (same as the dimensions of the SiN waveguides used in this study). Their intensity profiles are shown beside each to illustrate the evanescent tail at the boundary of the waveguides. As with the nanowire waveguide, the intensity of the evanescent tail into the substrate is higher than in vacuum. Our nanowire-waveguide coupling is based on the evanescent field in the two structures. As such, the above indicates that it may be better to place the nanowire on top of the waveguide rather than beside the waveguide. Another reason to place the nanowire on top of the waveguide rather than beside it is that the nanowire cannot be placed at the centre of the mode where the intensity is strongest. It would have to be placed slightly lower which changes the mode coupling between the nanowire and ridge waveguide.

The ultimate goal of this project is to fabricate on-chip photonic integrated structures using nanowire-quantum dots as our single-photon source and SiN waveguides as our medium to guide light through the chip. Having a well designed taper for the nanowire waveguide expands the HE_{11} mode. Not only does this help collection of the quantum dot emission through both a free-space and optical-fibre system, but it also allows for evanescent coupling of the nanowire mode into the rectangular SiN waveguide. The emission from the quantum dot is guided through the length of the nanowire until it reaches the taper where the fundamental HE_{11} mode is expanded radially from the axis as the light continues to travel along its narrowing shaft. The evanescent tail couples into the ridge waveguide and continues to propagate through the SiN waveguide.

We simulate the evanescent coupling of nanowires modes onto an underlying ridge SiN waveguide as show in Figure 2.13(a) using COMSOL. Here, we look at the x-component (up) of the electric field coupling from the nanowire to an underlying waveguide. The confined HE_{11} mode in the nanowire expands along the taper and evanescently couples into the TE or TM modes of the SiN waveguide. Figure 2.13(b) shows the power fraction of the

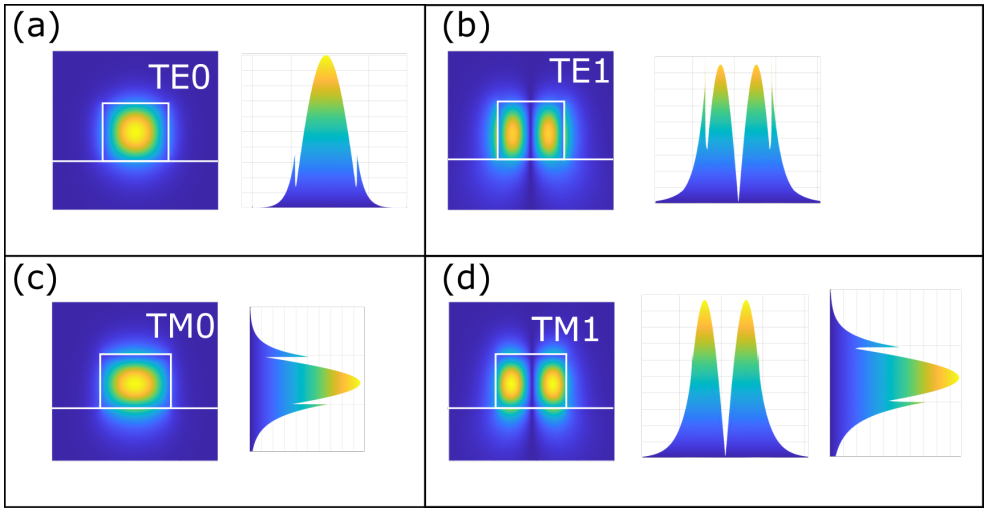

Figure 2.12: **Simulation of ridge waveguide modes.** The intensity of the electric field are shown as a cross-sectional view and side profile of the (a) TE0 mode, (b) TE1 mode, (c) TM mode, and (d) TM1 mode. Simulations courtesy of Dr. David Northeast.

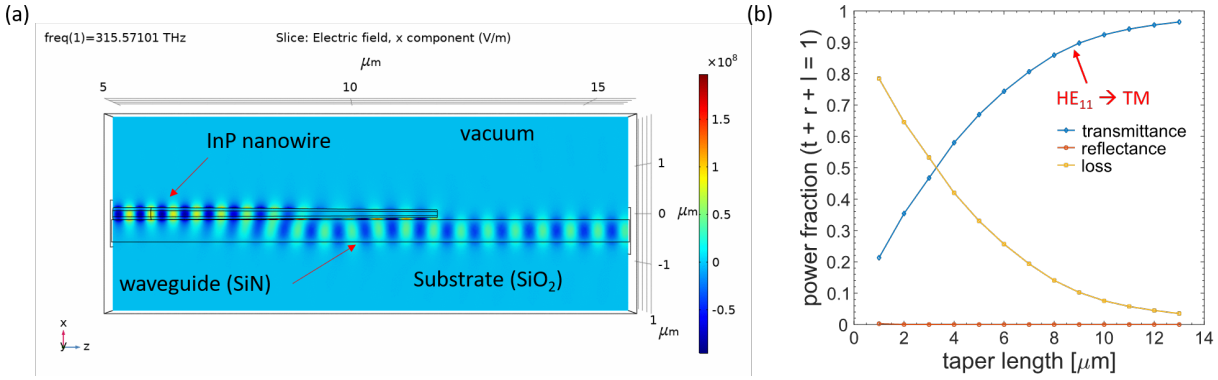

Figure 2.13: (a) Simulation of evanescent coupling of HE_{11} mode into underlying ridge waveguide. (b) Calculated fractional power transmitted, reflected, or loss depending on the nanowire taper length. Simulations courtesy of Dr. David B. Northeast.

energy transfer from the HE_{11} mode of a nanowire to the TM mode of a SiN waveguide as a function of the taper length. For sufficiently long tapers of 10 μm, a coupling efficiency of 90% in the TM mode was obtained with minimal loss scattered into other modes. With even longer tapers, near coupling unity is achievable.

Chapter 3

Experimental Methods

Simulations in Section 2.5 have shown the feasibility of integrating nanowires with SiN waveguides through the evanescent coupling of their modes. In this chapter, we focus on the experimental techniques involved in the growing, measuring, and assembling of the nanowire-photonic integrated circuit.

The first part of this chapter focuses on the fabrication techniques behind the growth of the quantum dot-nanowire devices (Section 3.1) and the foundry process for making the photonic integrated circuit chips (Section 3.2). We then describe the manipulation technique ("pick and place" method) used to integrate quantum dot-nanowire devices with photonic integrated circuits on chip (Section 3.3). We give an overview of the optical measurement techniques used for to characterize the optical properties of the quantum dots (Section 3.4) including the emission spectra, lifetime, single-photon purity, and indistinguishability of the quantum dot emission.

3.1 Nanowire growth

As a reminder from Section 2.3.1, epitaxially-grown quantum dots using the Stranski-Krastanov growth method [102, 9] nucleate into random sizes resulting in a broad range of emission energies from dot to dot. The high-index material of the quantum dot makes it difficult for the emission to travel outside of the medium due to total internal reflection [8] thus decreasing the collection efficiency from the quantum dot. Nanowire waveguides enhance the light emission properties and light collection efficiency from the quantum dot by coupling the emitter to an easy-to-collect optical mode. The nanowire functions to guide the light emitted by the quantum dot through its core. The higher refractive index of the nanowire waveguide ($n \approx 3.37$ at $\lambda \approx 950$ nm [10]) compared to its surroundings allows light travelling through the nanowire to go through total internal reflection at the waveguide edges. Simulations of the waveguide transverse mode in Figure 3.1(a) show the distribution profile of the electric field. This mode (HE_{11}) is maintained without spreading as it traverses the nanowire waveguide. Although the light is mostly confined in the higher refractive index of the material, leaking of the electric field at the boundary of the waveguide

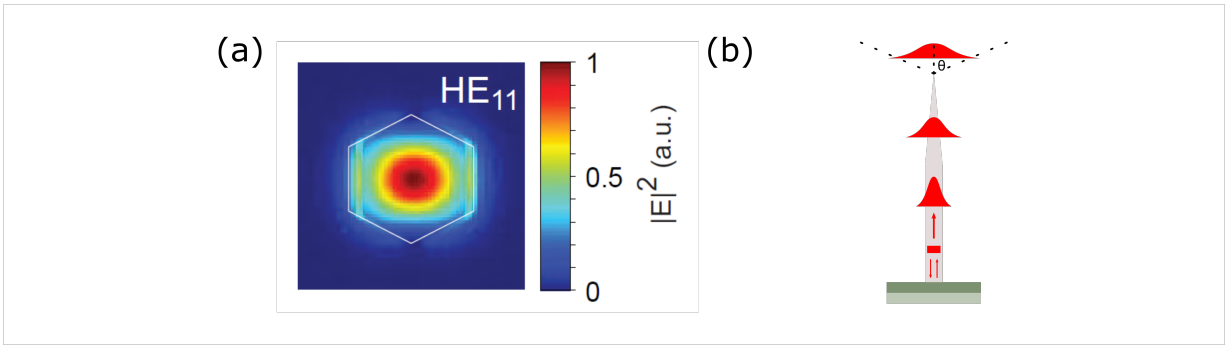

Figure 3.1: (a) Simulation of nanowire waveguide HE_{11} mode. Adapted from Bulgarini, G. (2014). Nanowire-based Quantum Photonics. [23] (b) Expansion of HE_{11} mode as light propagates through taper of nanowire waveguide.

may occur. To limit the divergence of the beam, as the light leaves the nanowire and into the far-field, a tapering of the nanowire by 1-2° [61] is necessary (see Figure 3.1(b)). This also helps reduce possible back-reflection from the tip of the nanowire. The mode couples efficiently into single-mode fibres [22] for an all fibre-based approach.

There are two approaches to growing nanowires embedded with quantum dots, top-down and bottom-up. A top-down approach is capable of obtaining 72% efficiency for a nanowire containing a reflective dielectric mirror at its base [29]. However, the location of the quantum dot may be off the nanowire axis when grown with this method which may lower its single-photon efficiency [17]. Additional quantum dots may also accidentally be embedded in the growth process of the wire which may not be desirable. A bottom-up approach ensures a desired number of quantum dots grown are within the nanowire core [18, 52, 67, 89, 105]. The geometry of the quantum dot is determined by the diameter of the core and the height of the quantum dot layer within the core [16, 34].

3.1.1 Fabrication of nanowire waveguide: Selective-area-vapour-liquid-solid epitaxy

The nanowires were grown with a site-controlled, bottom-up approach using a combination of selective-area (SA) and vapour-liquid-solid (VLS) epitaxy, which we termed SA-VLS epitaxy. The SA approach is performed on a III-V semiconductor coated with a mask [60]. Nanowire growth is promoted only in unmasked areas of the substrate in an axial direction. The VLS approach promotes growth at a metal catalyst to ensure layer-by-layer growth only at the metal-semiconductor interface [34]. The quantum dot is grown by simply switching from the host semiconductor material to the quantum dot semiconductor material. Radial growth is promoted around the nanowire core to create a cladding necessary for efficient quantum dot coupling into the nanowire.

It is necessary to separate the growth process into the two steps to control for distinct geometries required in the nanowire design. The first step serves as a template for the crystalline structure of the InP. For use as a single-photon source, the diameter of the

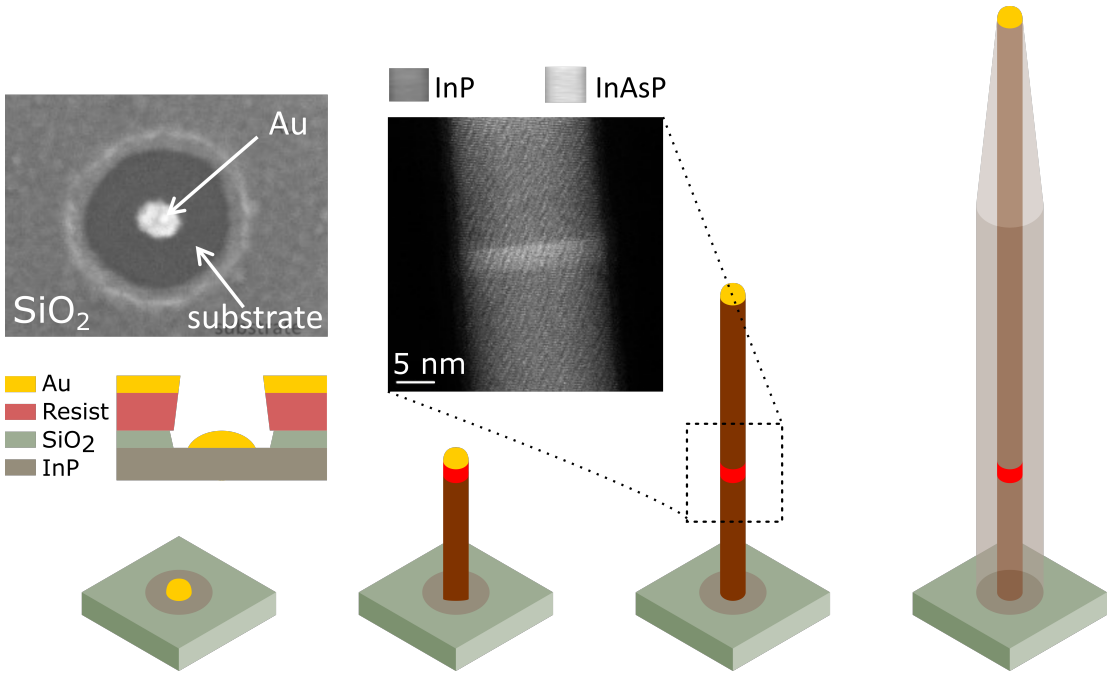

Figure 3.2: **Single nanowire growth process.** A gold catalyst is placed in the centre of the circular opening of a SiO_2 mask. A first growth mode incorporates InP only at the Au-InP interface resulting in a wire with a diameter dictated by the diameter of gold catalyst. AsH_3 is then injected in the system briefly to produce a thin InAsP layer comprising the quantum dot. A second growth mode is used in order to promote growth from the rest of the exposed InP substrate. This creates a shell cladding around the InP nanowire core.

core needs to be sufficiently small to provide strong confinement of the quantum dot. The second step provides a cladding much larger than the core of a diameter that supports the optical mode into which the photons from the quantum dot emit.

Preparation of growth substrate

Starting with an indium phosphide (InP) wafer, a 20 nm layer of silicon oxide (SiO_2) is deposited on a (III)B InP substrate using plasma-enhanced chemical vapour deposition (PECVD). A layer of resist (ZEP-A N-Amyl Acetate) is then deposited over the surface of the InP wafer. Electron-beam lithography is used to pattern the substrate with circular holes of a desired diameter. The diameter of the SiO_2 mask openings define the final diameter of the nanowire waveguide. As mentioned in Section 2.4.1, the base diameter is chosen to confine the HE_{11} fundamental waveguide mode and maximize spontaneous emission rates from the quantum dot. Wet etching with buffered oxide etch (BOE) containing hydrofluoric acid (HF) is used to expose the InP surface within the oxide holes. Fifty angstroms of gold (Au) is deposited through electron beam evaporation. This thickness is chosen to achieve Au nanoparticles of 20 nm diameter inside the mask openings. A lift-off process removes the resist layer along with the unwanted Au while the Au particle inside the holes are intact. The schematic of the intermediate step before lift-off and the final

result from this first stage are shown in the leftmost panel of Figure 3.2. The gold particle is seen in the centre of a dark annulus from InP. The region surrounding the hole is SiO_2.

Growing the quantum dot and nanowire core

The holes containing exposed InP substrate and gold nanoparticles proceed to chemical beam epitaxy (CBE) for growth of InP/InAsP nanowire quantum dots. First, we use selective-area epitaxy to start growing the nanowire in areas with only the exposed InP and Au nanoparticle. The Au acts as a catalyst as a stream of trimethylindium (TMI) and pre-cracked phosphine (PH_3) is injected into the system. This step is done at low growth temperatures of 420 °C $\sim$ 435 °C. The main steps of the growth process are shown in the centre two panels of Figure 3.2. The catalytic growth of the nanowire at the Au-InP interface is controlled by the flux of TMI.

Stacking faults in the nanowire core may arise during this growth process (see Ref. [34, 87]). III-V compounds are expressed in two main crystallographic structures: cubic zincblende and hexagonal wurtzite lattice structures. In the bulk form (such as a wafer), InP demonstrates a cubic zincblende structure. However, the preferred phase of InP nanowires grown with VLS is the hexagonal wurtzite crystalline structure [47]. As the InP grows in the CBE system, occasionally the phase sequence (or rotation of the bilayer of InP with respect to the underlying layer) changes, resulting in a stacking fault. This is where the alternations of the bAaBbA... stacking sequence of the wurtzite phase changes to the cAaBbCcA... stacking sequence of the zincblende phase (see Ref. [4]) and vice versa.

In order to maintain a pure wurtzite crystal phase within the nanowire, a low flux of TMI is used [87]. The pre-cracked PH_3 flow is temporarily stopped as arsine (AsH_3) is introduced into the system. This brief injection of AsH_3 creates a thin layer of InAsP (i.e. the quantum dot). The thickness of the dot is controlled via how long AsH_3 is introduced into the system during the growth process. Figure 3.2 (middle) shows a TEM image of an InAsP quantum dot (light grey) sandwiched between InP material (darker grey).

Cladding of the nanowire core

Another growth mode which employs a higher PH_3 flux and a higher growth temperature selectively promotes radial growth in the exposed InP annulus and creates a cladding around the nanowire core. This cladding has the same crystal structure as the core [33]. During the selective-area radial growth around the nanowire core, VLS has not been inhibited. This results in a photonic nanowire of a height taller than the original core and a taper with the same diameter as the core at the tip. The taper is a consequence of the radial and axial growth of the cladding, and a combination of the two determines the degree of the taper [35]. The schematic of the final tapered nanowire is shown in the rightmost panel of Figure 3.2.

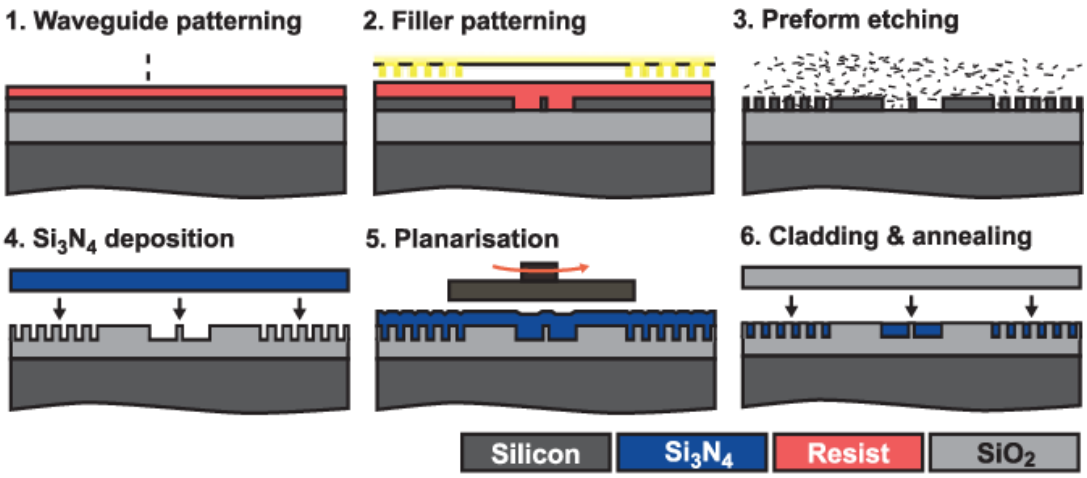

Figure 3.3: **Schematic of Damascene process for fabricating waveguides.** Adapted from Pfeiffer, M., *et. al.* (2018). *Photonic Damascene Process for Low-Loss, High-Confinement Silicon Nitride Waveguides.* IEEE Journal of Selected Topics in Quantum Electronics, 24, 1-11. [84].

3.2 SiN waveguide fabrication

Silicon nitride Si_3N_4 waveguides form the basis of efficient, non-linear photonic platforms [86, 107]. Silicon nitride has a wide transparency range and a band gap of $\sim 5\,\text{eV}$, making them suitable for wavelengths from the visible range all the way to telecom. A main source of loss through these waveguides is scattering loss at the surface of the waveguide due to the roughness of the surface. More detail about losses through waveguides is discussed in 5.1. Using a Damascene process [85] to fabricate the Si_3N_4 waveguides, ultra-smooth waveguides are achieved [86] which greatly help in reducing scattering losses. A schematic of the Damascene process is shown in Figure 3.3. In this process, the waveguide and filler/stress patterns are etched in a layer of resist on silicon. The filler/stress pattern is necessary here for alleviating the high-tensile, Si_3N_4 film stress that may lead to cracking at the SiO_2/ Si_3N_4 interface upon the heating and cooling of the completed patterned substrate. Then, a preform re-flow process anneals the silicon at 1523 K in a oxygen rich environment for 18 hours to smooth out the sidewalls of the waveguide preform. In this process, the etched silicon becomes SiO_2. Next, a low-pressure chemical-vapour-deposition (LPCVD) Si_3N_4 thin film is deposited over the surface of the substrate to fill up the preform. The entire substrate is then mechanically polished to planarize the substrate. Finally, the sample is clad and annealed to protect the newly made waveguides. Small openings are made in the protective oxide layer to expose the underlying ridge waveguide for placement of nanowire devices.

The waveguide structures were designed by Robin L. Williams through simulations in COMSOL and finite difference time-domain simulations which solve Maxwell's equations for the propagation of light in a photonic structure at every point in space defined by a mesh. The chip layouts were drawn by Khaled Mnaymneh using CAD software and sent

to the commercial foundry, LIGENTEC, for development. The individual components of the photonic integrated circuit are ridge waveguide structures made of silicon nitride (Si_3N_4). The ridge waveguides have dimensions 800 nm by 485 nm, taper off to 200 nm over a distance of 600 μm as it approaches the edge, and continues at those dimensions for 10 μm until the edge of the chip. Only the width of the waveguide changes while the height remains fixed at 485 nm. The purpose of the taper is to expand the mode and improve the mode matching between the fibre and waveguide. Without the taper, mode mismatches lead to poor coupling. With the taper, coupling between a lensed fibre and the waveguide can be easily achieved by coupling their Gaussian beam profiles at the optimal position for highest intensity.

3.3 Manipulation for Integration: Nanomanipulator

We describe here how we place our nanowires onto a photonic integrated circuit. Using a scanning electron microscope (SEM) based nanomanipulator, we are able to pick nanowires off from their growth substrate and place them anywhere on a second chip containing SiN ridge waveguides. The nanomanipulator device is shown in Figure 3.4(a). The two probes are free to move in the x, y, and z directions. The stage is only free to move in the x and y directions. Fine movement of the probe and stage are controlled with piezos. Both the growth substrate sample and photonic integrated chip are placed on the same stage between the two probe tips for easy access to both chips.

After connecting the system in the SEM, we locate the nanowire in an array grown using the desired growth conditions. Ideally, the nanowires would have already been characterized prior to picking, but that is not not the case here. To pick up a nanowire, simply breaking the contact between the nanowire and its growth substrate is enough to attract the nanowire through electrostatic forces within the charged SEM environment to the probe tip. Figure 3.4(b) shows a probe tip within an array of nanowires prior to pickup. The nanowire is then transferred to a chip with ridge waveguides. The second nanomanipulator probe is needed to assist in the removal of the nanowire from the first probe and to push the nanowire down onto the waveguide. After the nanowires have been placed on the waveguide, they remain firmly attached on the chip.

Openings in the oxide layer of the chip reveal areas of exposed SiN waveguide. The nanowire can be placed anywhere along the exposed waveguide on the photonic integrated chip. For our purposes, we tried to position the nanowires on top of the waveguide for maximum mode transfer. However, this was not always possible, and some nanowires were placed beside the SiN waveguide. Figure 3.4(c) shows a false-coloured image of a nanowire (purple) on a SiN ridge waveguide (blue). The rest of the waveguide is covered in a protective layer of SiO_2.

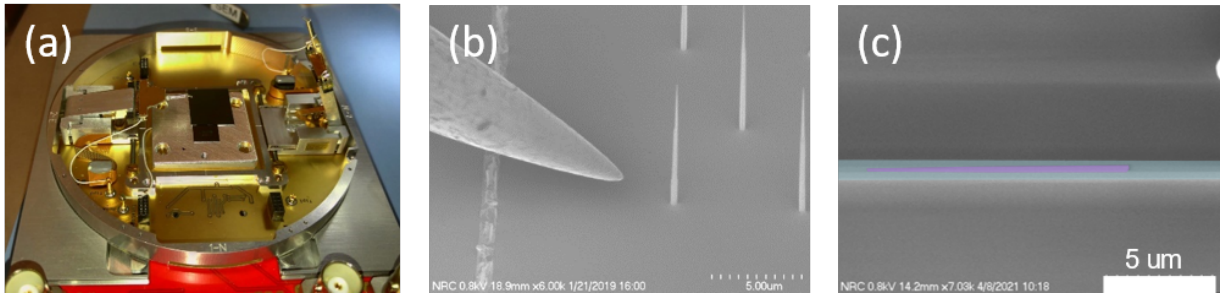

Figure 3.4: (a) Nanomanipulator with probes and chips for transfer securely mounted in the centre stage. (b) SEM of nanomanipulator probe about to pick up one nanowire. (c) SEM of nanowire placed on top of a ridge waveguide with false colours to highlight the nanowire in purple and waveguide in blue.

3.4 Experimental Optical Methods

In this section, we describe the experimental techniques used to characterize the optical properties of the quantum dot nanowires in various configurations to determine if it is a good source of single photons. We are interested in the emission spectra of the quantum dot through photoluminescence spectroscopy, the lifetime of the quantum dot's excitonic complexes through time-resolved photoluminescence, the single-photon purity through taking Hanbury Brown-and-Twiss measurements [51], and the indistinguishability of photons through Hong-Ou-Mandel measurements [54].

3.4.1 Spectroscopy

We are interested in measuring the emission spectra of the quantum dots. In this thesis, we employ three different setups for measuring the spectra from a quantum dot. The first is a free-space setup generally used for measuring a nanowire standing perpendicular to its growth substrate. The latter two are all-fibre-based setups used for collecting the spectra from a chip containing nanowires. All three setups are shown in Figure 3.5(a-c).

Free-space setup

In a free-space setup (see Figure 3.5(a)), light from an excitation laser is directed towards a sample in a cryostat via a beam splitter and focused on the sample with a microscope objective (100×, numerical aperture (NA) = 0.81). As such, this type of setup is called a micro-PL. Light is absorbed by the nanowire, and the emission is collected by the same objective. From there, the collimated beam has two paths it can go: either towards a complementary metal oxide semiconductor (CMOS) camera used to image the sample or towards a fibre-coupler before the emission is sent to a fibre-coupled detector.

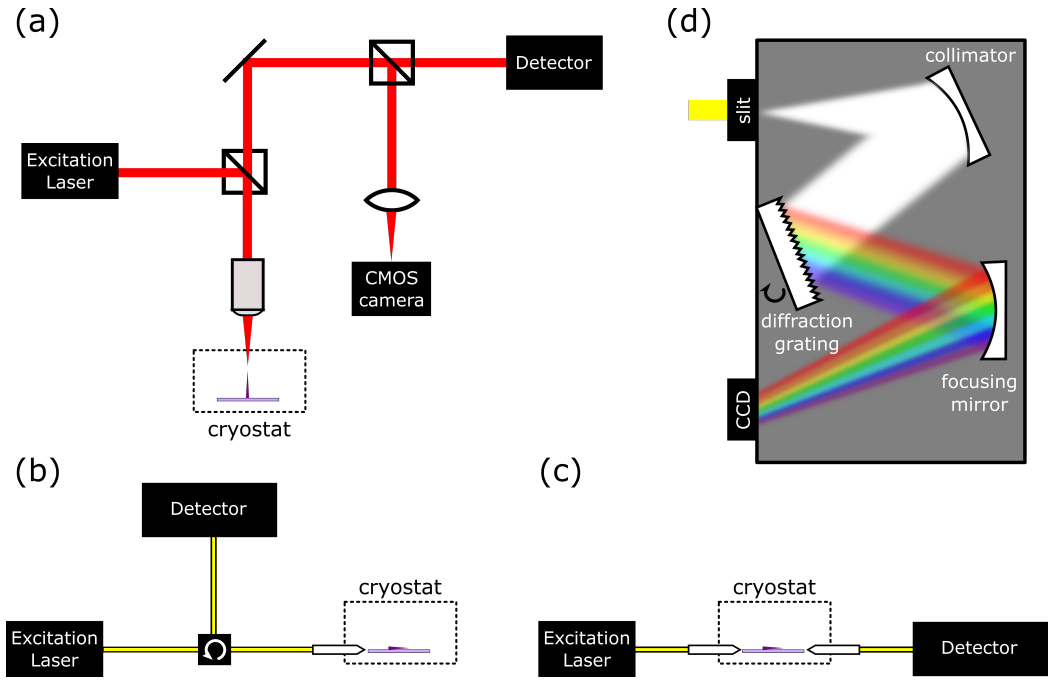

Figure 3.5: **Photoluminescence measurement setups** in (a) free-space for upright nanowires on a growth substrate and in fibre for nanowires on waveguides using a (b) circulator to pump and collect from the same side or (c) two separate fibres to pump and collect at opposite ends of the waveguide. (d) Schematic of diffraction grating spectrometer.

All-fibre-based setup

In the all-fibre-based setup, we measure the emission from nanowire devices coupled to SiN ridge waveguides on chip. Lensed fibres are used at the facets of the ridge waveguides to couple the light to and from the waveguides for the purpose of pumping and collection. Lensed fibres with a radius of curvature 3.5 μm were chosen for optimal mode matching with the tapering of the waveguide at 950 nm. To optimize coupling between the lensed fibre and waveguide facet, the lensed fibres are attached to piezo-controlled stages for precise movement. The nanowire waveguide mode couples into the ridge waveguide and continues to propagate through the waveguide until it reaches the collection lensed fibre. Instead of an objective, the emission collected through the fibre is sent straight to a detector system.

We use two pump/collection setups. The first (see Figure 3.5(b)) setup uses a circulator or fibre-coupled beam splitter to direct laser light towards the waveguide. Emission from the quantum dot is collected through the *same* input fibre. The circulator redirects the light from the circulator towards the detector. The second (see Figure 3.5(c)) setup uses separate fibres for pump and collection of quantum light emission from either end of the waveguide. The first method is good for situations were collection from the opposite facet is not possible. This may be due to defects at one facet or if the chip is designed to only allow collection from one side of the chip (see Figure 5.1(c)). In both these methods, we use the CMOS camera to image the surface of the sample.

We employ two different types of detectors, the first utilizes a monochromator and

silicon-based charge-coupled device (CCD) camera, and the second uses a single-element avalanche-photo-diode (APD) detector.

Diffraction grating spectrometer

The first detection method uses a diffraction grating spectrometer with specifications as show in Table 3.1. The schematic of the diffraction grating spectrometer is shown in Figure 3.5(d). As light enters the slit, it diverges. A collimating mirror is used to collimate the light and direct it to the diffraction grating. Here, the polychromatic incident light is dispersed so that each wavelength is reflected from the grating at a slightly different angle. The angle of the grooves in the grating influences the wavelength range the grating is optimised for. This dispersion of the grating is understood with the grating equation

$$n\lambda = d(\sin\theta_i + \sin\theta_d) \tag{3.1}$$

where n is the order of diffraction, λ is diffracted wavelength, d is the distance between successive groves, $\sin\theta_i$ is angle of incidence, and $\sin\theta_d$ is the angle of diffraction. The larger the number of grooves, the smaller the wavelength range but higher the resolution. The dispersed light is then focused with a mirror onto the CCD detector. We typically operate the CCD in graph mode by binning the 100 pixels (in the y-axis) to acquire the final intensity counts at each wavelength. For the 1200 g/mm grating, we have a resolution of 0.08 nm.

Pylon:100BR_eXcelon	
pixel array	1340 × 100
pixel size	20 μm x 20 μm

SpectroPro HRS-500	
focal length	0.5 m
grating	150 or 1200 g/mm

Table 3.1: Specifications of the nitrogen-cooled spectrometer used in our lab.

Single-element detector

We employ a single-element detector containing a monochromator and an APD detector, both of which are fibre-coupled devices. Since there is no spectral resolution with the APD detector, a tunable filter with a bandwidth of 0.076 nm (24 GHz) at 945 nm is employed to spectrally select specific lines of interest. The filtered emission is sent to the APD detector.

3.4.2 High-resolution spectroscopy

Due to the limited resolution of the grating spectrometer, it is difficult to measure the actual linewidth of each emission peak. To measure the linewidth of a single emission line

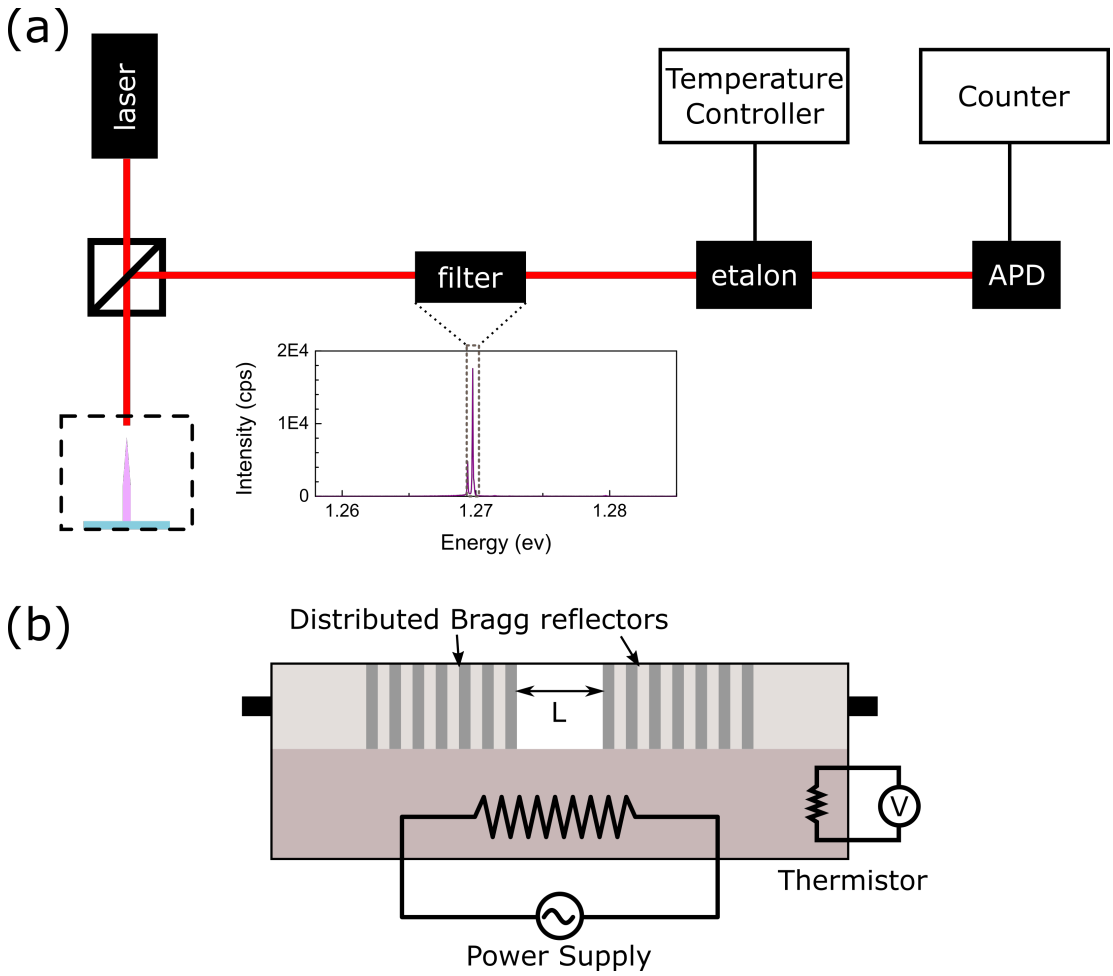

Figure 3.6: **Schematic of high-resolution PL spectroscopy** with an etalon. (a) An excitation peak of interest is selected through a tunable filter. The emission is sent to an etalon set to a specific temperature. The count rate at each temperature is measured by an APD detector to recreate the emission spectrum. (b) The etalon consists of two distributed Bragg reflectors and a cavity of length L controlled by a power supply and thermistor.

at much higher resolution, we use a temperature-controlled, fibre-coupled, Fabry–Pérot interferometer, also known as an etalon, as a filter with an APD detector. First, the emission from the exciton is filtered through the 24 GHz tunable filter before going through the etalon (BW = 0.5 GHz). The etalon is temperature-tuned and APD counts are measured at each temperature. The line profile of the emission peak is then reconstructed from the temperature with its corresponding APD counts. The schematic of this setup is shown in Figure 3.6(a).

The fibre-coupled, Fabry–Pérot etalon consists of two distributive Bragg reflectors separated by some distance L which make up the optical cavity as shown in Figure 3.6(b). The free-spectral range (FSR) is the frequency space between consecutive transmission peaks and is inversely proportional to L. For our particular fibre-coupled, Fabry–Pérot etalon, it has an FSR of 100 GHz. Additionally, light can only escape the cavity if its optical mode is

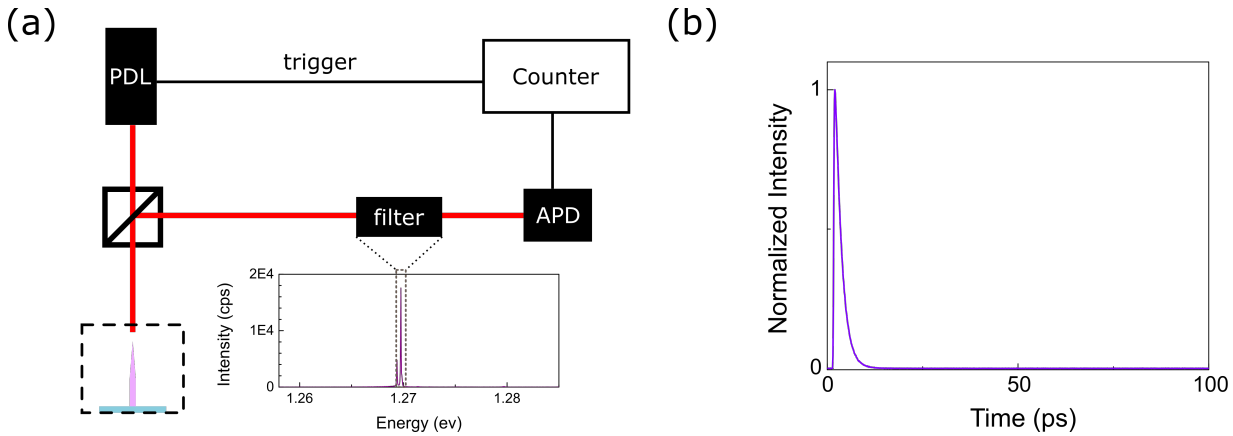

Figure 3.7: (a) Schematic of lifetime measurement using a pulsed diode laser for excitation and as trigger. (b) Typical lifetime measurement of an exciton.

in resonance with the optical cavity. Therefore, by changing the length of the cavity, we are able to control the wavelengths transmitted through the cavity. The heating and cooling of the system expands and contracts the spacing between the two distributive Bragg mirrors, thus changing the spacing between the optical cavities and the allowed frequencies able to pass. A thermistor is used to read the temperature of the etalon in a feedback loop to control the spacing between the cavity.

By scanning a variable laser with a very narrow linewidth through the etalon and measuring the count rate with an APD detector, an instrument response function (IRF) of 1.3 GHz was measured. Due to the IRF, the linewidths measured with the etalon correspond to a convolution of the actual linewidth of the emission and the IRF.

3.4.3 Time-resolved spectroscopy

The time it takes for an exciton to decay to the vacuum state by producing a photon is a defined as the radiative recombination lifetime. The re-excitation of the quantum dot excitonic state is only limited by its lifetime. The shorter the lifetime, the faster the source can be operated. To measure the radiative lifetime, we use time-resolved photoluminescence.

Time-resolved photoluminescence measurements are commonly carried out by time-correlated single-photon counting. This method measures the time between which a laser pulse is sent and the time it takes for an emitted photon to reach the detector. In order to measure the lifetime of a particular excitonic state in our setup, we first filter the emission peak associated with that state. Then we pump the nanowire with a 670 nm, pulsed diode laser with a 20MHz repetition rate. The 20MHz is necessary to allow the quantum dot enough time to completely relax into the ground state before the next pulse is applied. The setup requires a trigger signal ("start") from the pulsed diode laser to tell the counting card, Swabian Instruments TimeTagger, when a pulse has been applied to the system. The TimeTagger then waits for a filtered signal ("stop") from the quantum dot to register a count on the APD detector. After many repetitions, the time difference between the

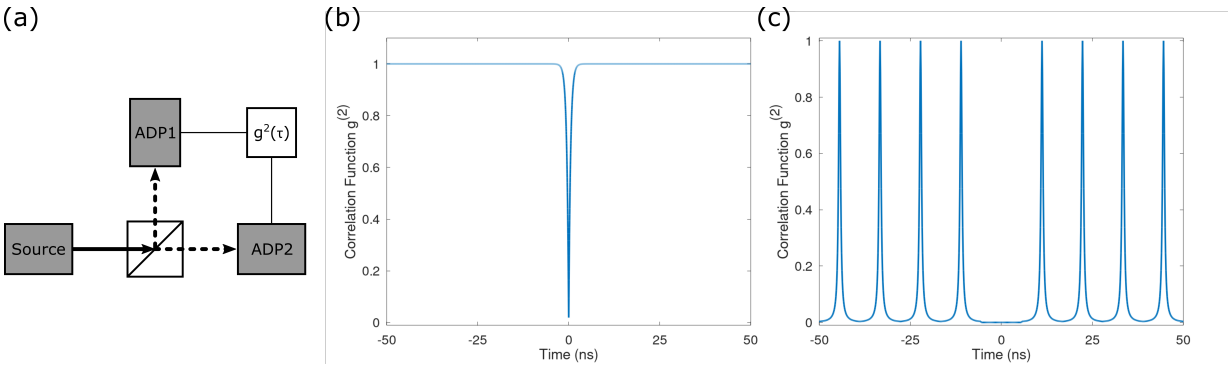

Figure 3.8: (a) Hanbury Brown and Twiss experimental setup. Idealized examples of autocorrelation measurements $g^{(2)}(\tau)$ of photons emitted from the recombination of an exciton confined in a quantum dot excited with (b) a continuous wave and (c) a pulsed laser.

trigger and the photon's arrival build up a histogram that reveals the average decay of the particular exciton. The exponential fit of this decay gives the lifetime of the excitonic complex such that

$$f(t) = A \exp\left(-\frac{t}{T_1}\right) \tag{3.2}$$

where T_1 is the exciton lifetime. Figure 3.7(a) shows the experimental setup used to measure radiative lifetimes of excitonic complexes as shown in (b).

3.4.4 Hanbury Brown and Twiss effect

The Hanbury Brown and Twiss (HBT) effect looks at the time correlation and anti-correlation effects of a stream of photons arriving at two detectors. The light from a quantum dot is split into two paths by a beam splitter each going to separate detectors. A correlation count is registered when a photon arrives at the start detector and another at the stop detector. Thus, if the source is indeed only producing single photons, there should not be any correlation counts registered at zero time delay ($\tau = 0$). The schematic of an HBT measurement is shown in Figure 3.8(a) along with typical graphs for an idealized case of single photon emission from a quantum dot excited with either a continuous wave (b) or pulsed laser (c).

The intensity-autocorrelation function $g^{(2)}(\tau)$ given in Eq. (2.3) can be rewritten as

$$g^{(2)}(t, \tau = 0) = \frac{\langle n^2(t)\rangle - \langle n(t)\rangle}{\langle n(t)\rangle^2} \tag{3.3}$$

where $\langle n(t)\rangle = \langle b^\dagger(t)b(t)\rangle$, and $\langle n\rangle$ and $\langle n^2\rangle$ are first and second moments of the photon statistics. Eq. (3.3) can be further reduced to $g^{(2)}(t, \tau = 0) = 1 - 1/\langle n\rangle$. When interpreting $g^{(2)}(\tau)$ data collected showing anti-bunching, if we take $\langle n\rangle$ as the average number of photons measured before the beamsplitter at $\tau = 0$, for pure single photons $\langle n\rangle = 1$, $g^{(2)}(0) = 0$. When there are more than one photon $\langle n\rangle \geq 2$, $g^{(2)}(0) > 0$ and tends towards

1 as $\langle n \rangle$ approaches infinity. A $g^{(2)}(0) < 0.5$ thus indicates single photons. For a single-photon source, it is convenient to use $1 - g^{(2)}(\tau = 0)$ to estimate the single-photon purity of the source.

A counting card from Swabian instruments called a TimeTagger is used to register the counts from each APD detector. There are, however, limitations in the system due to the detectors. The detectors we use have a 67 ns dead time which is the time between when a photon hits the APD and when the detector has recovered. During this time, the detector cannot see another photon. The dead time limits the maximum number of photons that can be detected per second to 15 Mcps. The resolution of the detector is limited to a 0.2 ns jitter.

3.4.5 Hong-Ou-Mandel effect

Hong-Ou-Mandel (HOM) effect looks at the visibility of two photon interference. The measurement itself is used to determine the indistinguishability of photons emitted from a source. The visibility is given as

$$V(\tau) = \frac{g_{\perp}^{(2)}(\tau) - g_{\parallel}^{(2)}(\tau)}{g_{\perp}^{(2)}(\tau)} \tag{3.4}$$

where $g_{\parallel}^{(2)}(\tau)$ is measured when the two interfering photons have the same polarization and $g_{\perp}^{(2)}(\tau)$ is measured with the polarization of interfering photons offset by 90°. Indistinguishable photons have a $V = 100\%$ meaning they are identical in spectral bandwidth, pulsed width, polarization, carrier frequency, and mode profile when the photons meet at a beamsplitter. Spectral-diffusion fluctuations cause shifts in the emission wavelength from the quantum dot, resulting in a lower distinguishability.

The typical setup for HOM measurements use a Mach–Zehnder interferometer to look at photons from the same source but delay sequential photons so that we can interfere them in time. When the two photons arrive at the beams splitter, each photon can either be reflected or transmitted. Figure 3.9(a) shows a schematic of the possible outcomes when the two photons meet. If the two photons are distinguishable, the paths of the photons are independent of each other, and their paths will take any of the four possible outcomes. If two photons are indistinguishable, then when they combine at the beamsplitter, the two photons will interfere and leave from the same port. Measuring correlations between the photons at the two output ports of the beamsplitter results in either Figure 3.9(b) in the distinguishable case or (c) in the indistinguishable case. Since the two indistinguishable photons must leave from the same port, there arises a dip at zero time delay.

We used an all-fibre HOM experimental setup to measure a nanowire placed on a straight ridge waveguide, a schematic of which is shown in Figure 3.10. An excitation laser is used to pump the quantum dot in nanowire. The quantum dot is excited and emits a photon upon relaxation to lower-energy states. The emission from the dot travels through the nanowire then evanescently couples into the underlying ridge waveguide before being

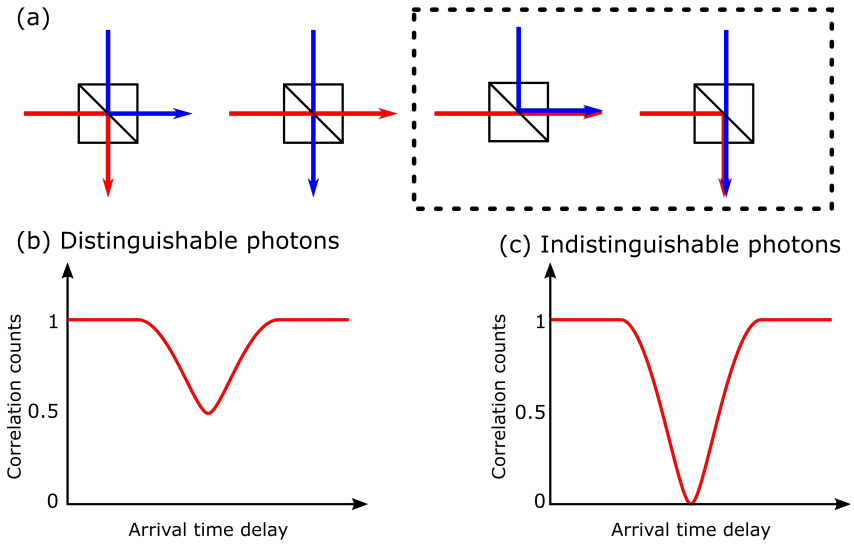

Figure 3.9: (a) Possible paths taken in a Hong-Ou-Mandel (HOM) experiment when two photons arrive at a beamsplitter. (b) Distinguishable photons may take any of the four paths. At zero time delay, the HOM dip is 0.5 since half the outcomes exit the same port. (c) Indistinguishable photons exit the same port resulting in a HOM dip of zero at zero time delay.

collected through a lensed fibre at the edge of the chip. To ensure linear polarization going through the rest of the system, two polarizers are used. The light is then sent through a 887 nm long-wave-pass filter and a tunable filter set to a specific wavelength corresponding to a specific emission peak from the quantum dot. The light is first polarized to ensure linear polarization before passing through a beam splitter. In the first arm of our Mach–Zehnder interferometer, a half wave plate is placed to offset the polarization of the photons that meet at the beamsplitter. Ideally, when the two photons arrive, if the two photons have the same polarization, $g^2_{\parallel}(\tau) = 0$. If the two photons have a polarization offset of 90°, then they will be completely distinguishable from each other and $g^2_{\perp}(\tau) = 0.5$. In the second arm, a compensation delay fibre is used to ensure the photons of this arm travel the same distance as through the half-wave plate arm. A second fibre is used to add a delay for the photon to travel before the photons of the two arms meet again at the input of the beamsplitter. The output from the beam splitters are sent to two APD detectors connected to a time tagger.

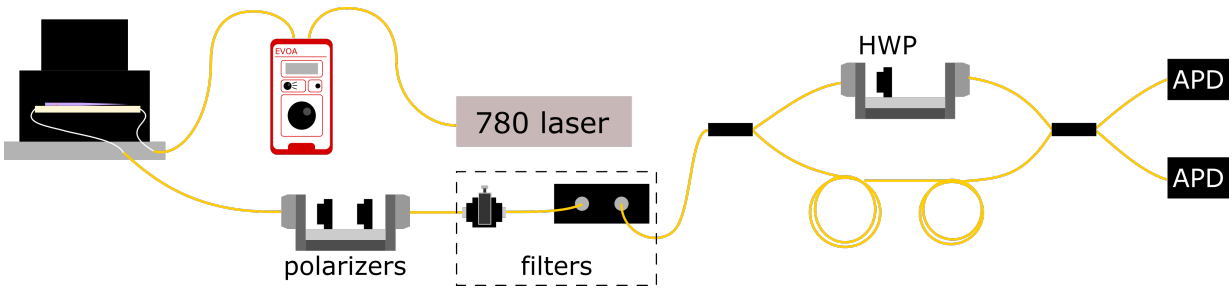

Figure 3.10: All fibre Hong-Ou-Mandel setup based on a Mach–Zehnder interferometer with polarization control on one arm to control the degree of distinguishability.

Chapter 4

Optical Properties of Quantum Dots on Growth Substrate

Nanowires are long, thin nanostructures exhibiting many useful electrical and optical properties. In particular, they can be easily manipulated and incorporated with other devices for use in quantum optics and nano-scale electronics. Embedding quantum dots in nanowires allows for the directional guiding of light emitted from a quantum dot into the nanowire core with minimal loss. An advantage of using a bottom-up growth approach is that nanowires may be grown at specific locations on a growth substrate through the lithographic technique described in 3.1 which allows the controlled individual pumping and collection from single nanowires. To collect the quantum dot emission, we use a free-space to fibre approach. A nanowire of interest is located under a microscope and individually pumped with a laser. As only the one nanowire is excited, we are able to collect emission from the one nanowire. The emission is collected through the objective and directed towards a fibre-coupler for compatibility with our fibre-coupled tunable filter, APD, and CCD spectrometer setups.

In this chapter, we discuss the optical properties of free-standing quantum dot embedded nanowires measured whilst still on the growth substrate. We first look at a regular photoluminescence spectrum of a nominal quantum dot in a nanowire in Section 4.1 and describe the emission peaks typically found in a full spectrum. This includes the two crystal phases of InP, stacking faults arising from changes in the two phases, donor-acceptor complexes in the nanowire, and emissions from the discrete energy levels of the quantum dot. We focus first on how to characterize a single emission from a quantum dot including its photoluminescence spectrum, efficiency, lifetime, spectral purity, and single photon purity. Section 4.1.2 discusses excitonic radiative lifetimes and how they limit the maximum emission rate of the devices.

Not all the photons collected at a specific wavelength corresponding to a quantum dot emission are single photons. Since the goal is to fabricate a pure, single-photon source, in Section 4.2, we measure the actual single photon generation rate of the quantum dots and give an overall efficiency of single photons generated by the quantum dot.

In the latter half of the chapter, we examine more complicated quantum dot spectra.

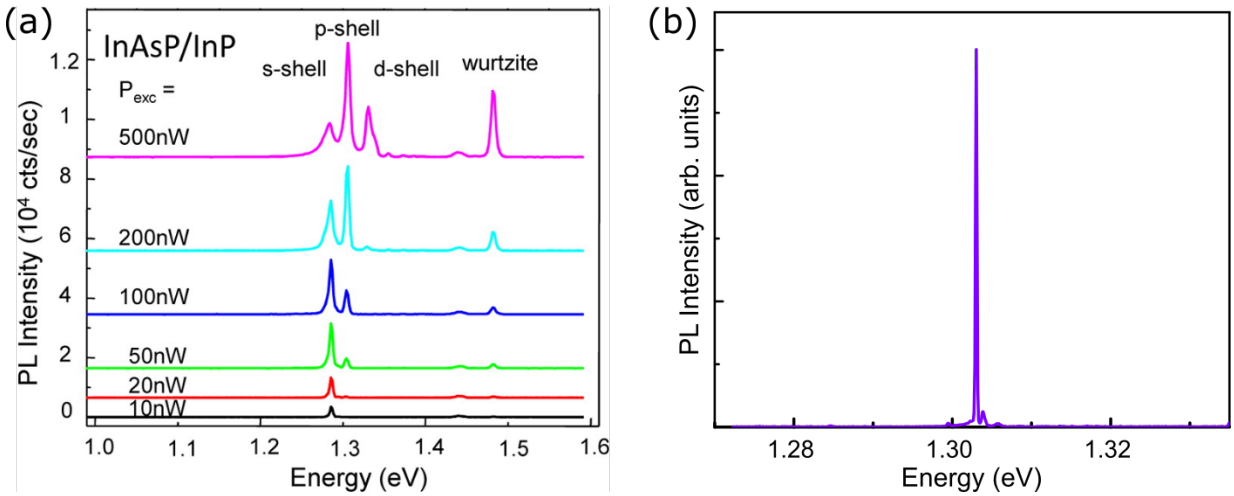

Figure 4.1: **Photoluminescence spectra.** (a) Power-dependent PL of a single nanowire containing an InAsP quantum dot. Adapted from *Nano Lett.* 2012, 12, 11, 5919-5923. (b) High resolution PL of low pump power excitation of a quantum dot.

Section 4.3 focuses on the emission peaks, particularly in the s-shell region of the quantum dot where neutral excitons, charged excitons, and biexcitons are formed. We describe how to distinguish between excitonic complexes and what methods are used for characterization.

4.1 Photoluminescence

We conducted micro-PL measurements to analyse single nanowires. The micro-PL setup involved a 100× microscope objective with a numerical aperture of 0.81 and either a 780 nm laser or a 632 nm helium-neon (HeNe) laser for excitation. The sample containing multiple arrays of nanowires embedded with quantum dots is placed inside a closed-cycle, He cryostat cooled to 4 K. Since a major factor leading to the broadening of the linewidth of quantum dot emissions is phonon absorption and emission [34, 59], which is especially prominent at higher temperatures, we measure our quantum dots at 4 K. Figure 4.1(a) shows power-dependent PL spectra from a single InP nanowire containing an InAsP quantum dot. A free-space set-up (Figure 3.5(a)) is used to measure all the nanowires studied in this chapter.

As mentioned previously in Section 3.1, the nanowires we use are grown with SA-VLS epitaxy. Due to the deterministic positioning of the quantum dot-nanowire devices on the growth substrate, we know that only one nanowire device is excited at a time with the excitation laser. A complementary metal oxide semiconductor (CMOS) camera installed in the path of the quantum dot-nanowire emission is used to image individual nanowires of interest and assist in focusing the laser on the wire. Wurtzite emission from the nanowire can be seen on the camera showing which nanowire is being excited.

Through the SA-VLS growth process, two crystal phases, called wurtzite (WZ) and zincblende (ZB), arise in the InP core. The WZ crystal phase is the favoured growth

during VLS [47], and as such, is the predominant emission from the nanowire itself where $\lambda \sim 832\,\text{nm}$. ZB, which is much less common, emits at $\lambda \sim 875\,\text{nm}$. Typically the ZB emission seen in the nanowire PL spectra is from the substrate. However, between the emission of the WZ and ZB phases are other emission features. These arise from stacking faults which consist of the ZB phase inserted into the dominant WZ phase. The stacking faults give rise to quantum confinement of carriers along the length of the nanowire. As such, ZB stacking fault emissions are seen at less than 875 nm. Close to a quantum dot, the stacking faults act as charge traps. These lead to spectral diffusion which lower the coherence of the quantum dot emission [76, 96] leading to a broadening of the linewidth. A great deal of effort has been undertaken to identify growth conditions that produce defect-free WZ nanowires. This was achieved by Dalacu *et. al.* [32] who successfully grew nanowires with minimal stacking faults allowing for multi-photon emission from the quantum dot to be below 1%. Since the crystal structure purity of the nanowire core determines the crystal phases of the shell, careful control of the core growth mode is necessary in fabricating stacking-fault free nanowires.

Not all the emissions found between 832 nm to 875 nm are from stacking faults. Donor-acceptor levels arising from impurities in the InP account for a series of close, weaker peaks around 860 nm [43]. These impurities may take the form of missing In or P atoms in the WZ crystal lattice, causing a doping effect.

The confined orbitals (s, p, d-shells) of the quantum dot ($\sim 1.3\,\text{eV}$) are clearly seen emerging as the power is increased. The weak WZ emission at low pump power shows how efficiently the free carriers are captured by the quantum dot. We are interested in the emissions at around 950 nm which is the s-shell of the quantum dot and where we will focus on for the rest of the chapters.

A spectrum of a quantum dot emission is obtained using a nitrogen-cooled CCD detector with 1200 grooves/mm grating. At low pump powers, the emission from the quantum dot is quite clean like the PL shown in Figure 4.1(b). A peak is seen at 1.30 eV (952 nm). Even with this spectrometer, measuring the actual linewidth of a single emission peak is limited by the resolution of the spectrometer of $50\mu\,\text{eV}$ or 12.5 GHz. From a fit of this particular spectrum, a centre energy of ∼1.32 meV and a linewidth of 0.18 meV (0.13 nm) is obtained.

On a second growth chip, we looked at a sample of a hundred nanowires under the same growth conditions and took PL spectra of each. These nanowires house a cylindrical $InAs_xP_{1-x}$ quantum dot of diameter $D_{dot} \sim 20\,\text{nm}$ and height $H_{dot} \sim 4\,\text{nm}$. The dot is approximately $\sim 1\,\mu\text{m}$ above the base of the nanowire and has a composition $x \sim 20\%$. The clad nanowires have a base diameter of 250 nm tapered to 20 nm over a length of $\sim 10\,\mu\text{m}$. A spread of all 100 PL spectra from one array is shown in Figure 4.2(a). It is currently unknown why, despite the same growth conditions as the previous chip, there is a shift in the expected average s-shell excitation energy from 1.3 eV ($\sim 950\,\text{nm}$) to 1.26 eV ($\sim 980\,\text{nm}$) for this particular sample as shown in Figure 4.2(b). Again, it is difficult to resolve the actual linewidths as they are limited by the resolution of the CCD detector and grating. The PL spectra from all one hundred nanowires consist of narrow peaks which verify the monochromatic nature of our dot emission. We discuss more on how to resolve

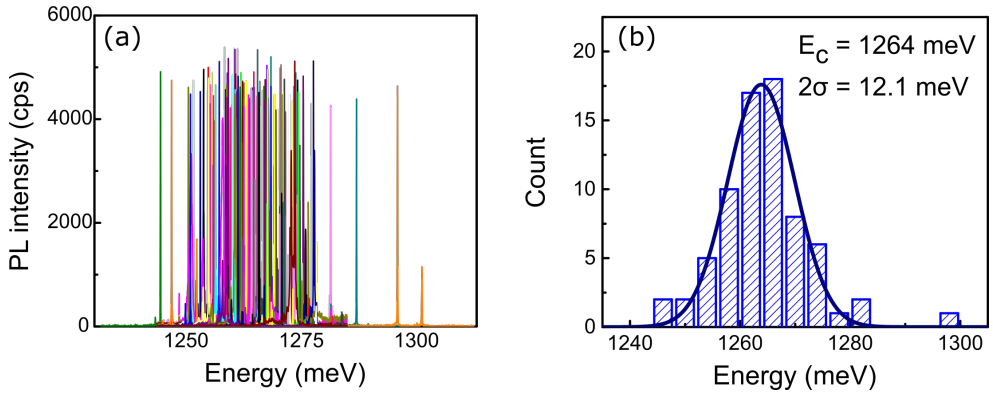

Figure 4.2: (a) Photoluminescence of 100 InP nanowires each with a InAsP quantum dot from the same array. (b) Energy of sixty-two quantum dots at the most prominent emission peak at low pump excitation power.

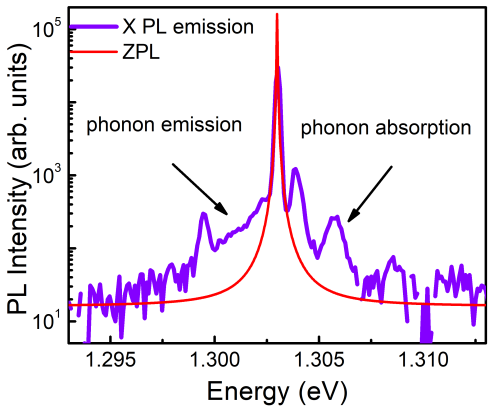

Figure 4.3: PL spectrum of a quantum dot with a logarithmic y-axis showing phonon emission and absorption sidebands. A fit of the zero-phonon line is shown in red.

the actual linewidth of the quantum dot emission in Section 4.1.2.

We employ two methods to find the count rate from a single emission peak. The first method is to simply take the PL of the dot emission and use a Lorentzian fit to calculate the integrated counts of the PL peak. This Lorentzian fit is known as the zero-phonon line (ZPL) because it negates the emission into the phonon sidebands which can account for up to 20% of total counts at 4 K [34]. Figure 4.3 is the same PL spectrum from Figure 4.1(b) except with a logarithmic y-axis to clearly show the phonon sidebands. The second method is to use a single-photon avalanche photodiode (APD) detector and tunable filter. The fraction of photons counted depends on the filter used which has a full-width half maxima (FWHM) bandwidth (BW) of 0.076 nm (24 GHz) at 975 nm. In comparison, the linewidth measured at the peak shown is 0.13 nm or 43 GHz. The filtered emission is sent to the APD and a counting card is used to tally up the number of photons hitting the detector. Comparing the integrated counts with the APD counts yields relatively similar

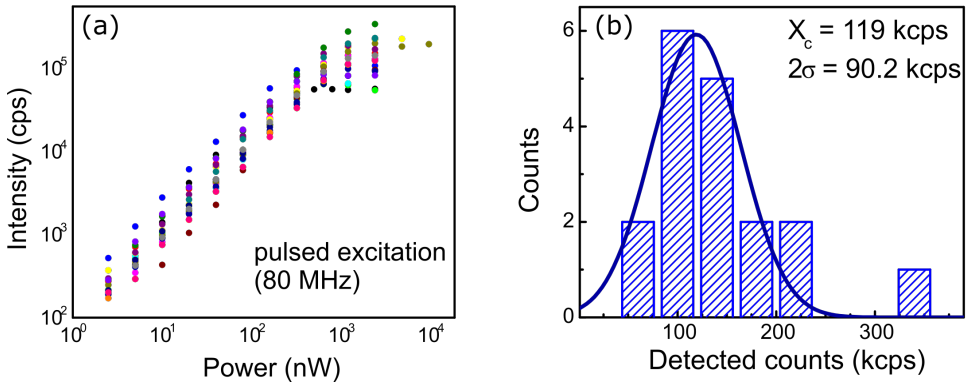

Figure 4.4: (a) Power-dependent intensities of a eighteen nanowires. (b) Histogram of maximum detected counts at saturation P_{sat}.

results with the integrated counts typically being $80 \sim 90\%$ of the APD counts on average.

Total counts using a continuous wave (CW) above-band laser typically yields much higher emission rates than with a pulsed laser. This is because the emission rate is lifetime-limited in the CW case as opposed to the repetition rate of the pulsed excitation laser. With a pulsed excitation laser, the highest count rate obtained was 342 kcps whereas with a CW excitation laser, the highest count rate was up to 1.2 Mcps.

4.1.1 Efficiency

To determine the efficiency of the source, we must first calculate the efficiency of the system. We focused on eighteen nanowires from the sample of a hundred nanowires grown under the same conditions to calculate the average source efficiency across the hundred nanowires. Since a fibre-based single-photon APD detector was used, the emission from the quantum dot had to be filtered through a tunable filter and set to the wavelength of the emission peak of interest. The eighteen nanowires chosen showed a bright dominant peak at low powers and had emission wavelengths of interest within the range of the tunable filter. A log-log graph of the APD count rate as a function of the pump power is shown in Figure 4.4(a).

The source efficiency η can be determined experimentally by exciting the nanowire with a pulsed laser to obtain the average number of photons emitted per excitation pulse. To ensure the emitter is excited with each pulse, the quantum dot is pumped at a power that saturates the emission, P_{sat}. For example, if we use an 80 MHz (12.5 ns) pulsed laser to excite a nanowire (assuming there is one photon per pulse), and we detect eighty million counts, then we have 100% source efficiency. In a recent growth sample containing 100 nanowires, using a 670 nm, 80 MHz, pulsed diode laser, we detected an average maximum count rate of $C_m = 119 \pm 45$ kcps from the exciton. This is shown in the histogram of Figure 4.4(b) by taking the maximum count rate at saturation of the exciton emission. Since a pulsed laser is used with a repetition rate greater than the radiative lifetime of the

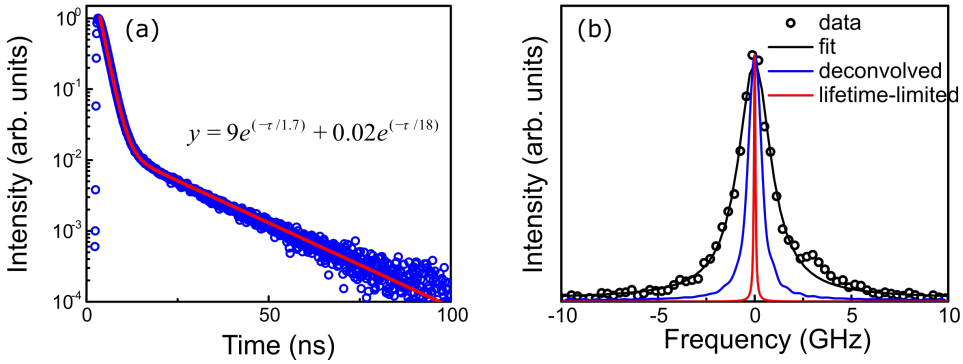

Figure 4.5: (a) Radiative lifetime of exciton complex. (b) Linewidth of the single exciton emission.

exciton ($\sim 2\,\text{ns}$) that allows enough time for the exciton to relax before the next pulse. As such, unlike with a CW laser, when pumping the quantum dot with a pulsed laser above the saturation of the two-level system, the count rate levels off as shown in Figure 4.4(a).

Taking into account the optical system efficiency ($\eta_s = 0.078$) and the detector efficiency ($\eta_d \approx 0.15$), we obtain a total loss $L = \eta_s \eta_d$. The counts at "first lens" can be calculated as C_m/L which is how many photons are present before passing through the first objective or lens of the system after emission from the quantum dot. From there, we calculate the source efficiency η as

$$\eta = \frac{C_m/L}{f_{\text{rep}}}, \tag{4.1}$$

where the pulse repetition rate $f_{\text{rep}} = 80\,\text{MHz}$. In our quantum dots, we calculate an average source efficiency of $\eta = 0.127$ for the eighteen nanowires.

We can also calculate the collection efficiency η_{coll} defined as the fraction of photons emitted from the top of the nanowire that is collected. To estimate the number of photons emitted from the top of the nanowire, recall that half of the quantum dot emission in the HE_{11} mode is directed upwards and the other half downwards, and that for an ideally fabricated device, we have $\beta_{\text{HE}_{11}} = 0.95$. Therefore, the maximum number of photons directed towards the top is the $f_{\text{rep}} \times \beta_{\text{HE}_{11}}/2$. Furthermore, of the photons directed towards the tip of the nanowire, only 0.8 reach the detector since 0.2 are emitted into the phonon sidebands at 4 K and are filtered out. This results in a collection efficiency of 33%. Note that this estimate assumes an internal quantum efficiency of 1 for a high quality quantum dot material.

4.1.2 Time-resolved photoluminescence - lifetimes

A shorter radiative lifetime of an exciton is advantageous for maintaining the coherence of the emission by limiting the timescale at which spectral diffusion [96] and acoustic phonon-mediated pure dephasing [104] occur.

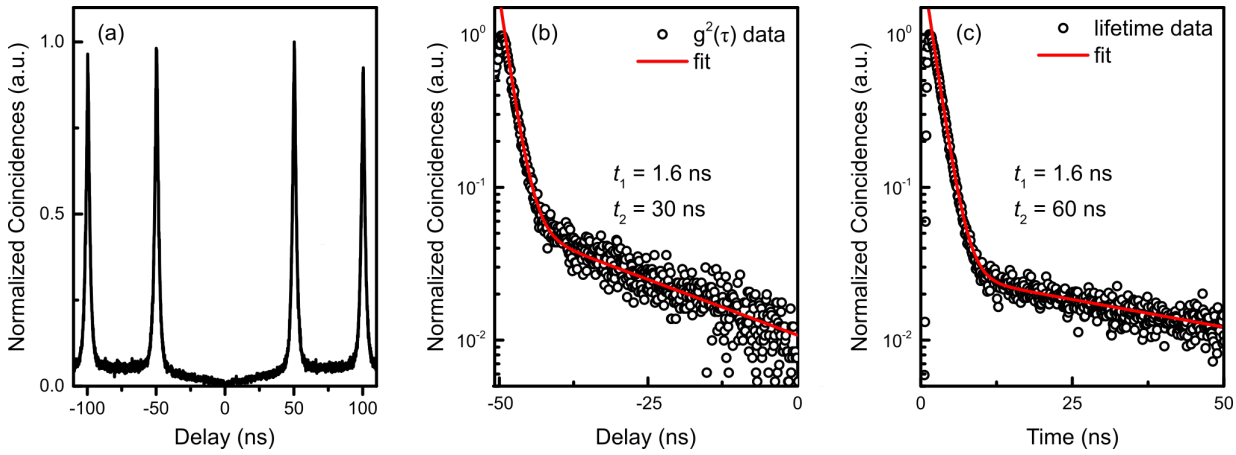

Figure 4.6: (a) Pulsed autocorrelation measurement of an excitonic complex at low pump power. (b) Semi-log pulsed autocorrelation showing only half a peak. (c) Lifetime measurement of the same exciton complex. Lifetime is extracted with a fit showing bi-exponential decay.

Typically, the results of a lifetime measurement for a neutral exciton look like a simple decay exponential function e^{-t/τ_x}, where τ_x is the lifetime of the neutral exciton. However, a two-phase exponential decay function may also be observed such as in the plot of the lifetime from one of the neutral excitons in the hundred nanowires as shown in Figure 4.5(a). Here, the dot displays a bi-exponential decay $y(t) = Ae^{-t/\tau_x} + Be^{-t/\tau_2}$ where τ_2 accounts for the much slower component in the radiative lifetime. The slow component corresponds to the dark exciton where spin flips are required for recombination to occur due to selection rules. This will be explained in greater detail in Section 4.3. It is important to note that since the y-axis is a log plot, the effect of the slow component may look exaggerated. We calculate the lifetime of this particular exciton to be $\sim 1.7\,\text{ns}$ which is similar to the bulk emission lifetime of $\sim 2.5\,\text{ns}$ for a normalized diameter of $D/\lambda = 0.24$ [34].

Using a pulsed laser, it is also possible to extract the lifetime of an exciton emission from its autocorrelation measurement (discussed later). Here, we extract the lifetime from an autocorrelation measurement by using a pulsed laser with a 20 MHz repetition rate. In Figure 4.6, we observe such an exciton with a long bi-exponential lifetime.

The nonzero background correlation counts are due to the long exciton lifetime of the slow component as seen in Figure 4.6(a). Coincidence counts do not have time to go to zero before the onset of the next excitation pulse. It does reveal itself at $\tau = 0$ in the absence of the centre peak due to the single-photon nature of the source. The slow-component is typically only observed at sufficiently low pump powers where the re-excitation probability is much lower.

Taking a fit of both the autocorrelation and the lifetime measurements yields similar τ_x values of 0.6 ns, whereas the fitted lifetimes of the slow components were quite different. We suspect that the slow component may be more sensitive to the pump power as the lifetime measurement is typically taken at a lower pump power compared to the pulsed

$g^{(2)}(\tau)$ measurement.

One way to overcome the limitations due to exciton recombination lifetimes and increase emission rates is to fabricate a nanowire with multiple quantum dots [67]. This type of multiplexed, single-photon source is possible with a bottom-up nanowire growth approach where each quantum dot is optimally positioned for maximum coupling to the same optical mode supported by the nanowire structure. If the quantum dots are placed too close together, a quantum molecule may be formed [11]. To avoid dot to dot electronic coupling, the quantum dots were spaced over 50 nm apart. The emission wavelengths in the nanowires were controlled by changing the flux of AsH_3 into the CBE system during the growth of each quantum dot layer. It should be possible to grow the quantum dots identically emitting at the same wavelength, however, our recent study of a hundred nanowires grown under the same conditions had varying emission wavelengths all within a close range to each other (981 ± 10 nm). For the purpose of this study, we were interested in knowing if five quantum dots embedded within the same nanowire could still emit single photons. Not only did the quantum dot maintain a high level single photon purity with $g^{(2)}(0)$ ranging from $0.012 \sim 0.094$, but the total detected count rate from one of the nanowire devices was greater than 2.2 Mcps with equal collection efficiency from each dot.

Spectral purity

Quantum key distribution protocols such as BB84 require a high rate of single-photon generation. Other secure communication schemes such as measurement-device-independent quantum key distribution [70], quantum repeaters for quantum networks [69], and quantum computing not only require a high rate of single-photon generation, but also require that the single-photons need to be indistinguishable. This indistinguishability means that they are identical in all degrees of freedom such as polarization, wavelength/ energy, coherence, and have a large wave-packet overlap [97]. Factors such as spectral dephasing can impact the degree of indistinguishability of the emitter. We look now at measuring the spectral purity of the emitter as one aspect in helping determine its degree of indistinguishably.

A fibre-coupled Fabry–Pérot etalon is used to take high-resolution PL of individual emission peaks. A linewidth of a single exciton emission shown in Figure 4.5(b) is 2.03 ± 0.04 GHz. Instead of four points that make up the peak emission with a linewidth of 0.13 nm or ~ 41 GHz, now there are over twenty points that reveal a much narrower linewidth (~ 0.006 nm). Since the linewidths in units of nanometers is so small, it is simply more convenient to discuss linewidths in terms of frequency (GHz) using $\Delta\nu = c\Delta\lambda/\lambda^2$ where $\Delta\lambda$ is the linewidth as a wavelength and $\Delta\nu$ is the linewidth as a frequency.

To determine the actual linewidth, the measured linewidth must be deconvolved from the IRF of 1.3 GHz discussed in the previous chapter. The blue line in Figure 4.5(b) shows the deconvolved linewidth which was calculated using a MATLAB routine. Linewidths of fourteen different quantum dot emissions were taken using the high-resolution PL setup with the etalon. After deconvolving the linewidths measured across the fourteen emissions, we arrive at the histogram shown in Figure 4.7(a). Ignoring the three at 2.02 GHz, the average deconvolved linewidth is 0.87 ± 0.36 GHz.

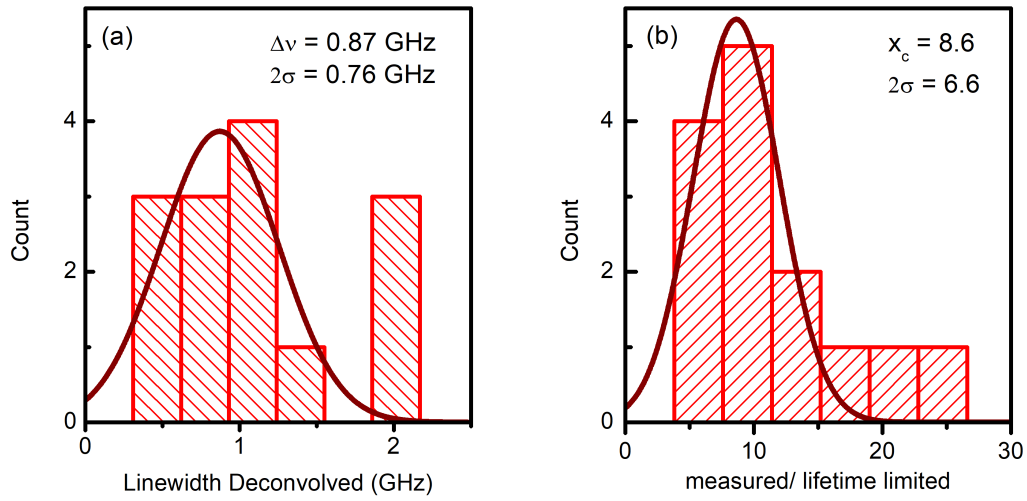

Figure 4.7: (a) Histogram of deconvolved linewidths taken from fourteen nanowires. (b) Histogram of ratios of the measured linewidth to lifetime limited linewidth.

Information about the coherence of the emitter can be obtained by fitting the spontaneous emission spectrum using a Lorentzian line profile. The homogeneous coherence time T_2 of a photon source is given as [90].

$$\frac{1}{T_2} = \frac{1}{2T_1} + \frac{1}{T_2^*} \tag{4.2}$$

where T_1 is the exciton lifetime and T_2^* is the pure dephasing term. Contributors of dephasing include charge-fluctuation noise and spin noise from the coupling of exciton spins and a fluctuating distribution of the charge environment around the quantum dot [66] which result in a broadening of the ZPL. The ideal case is the lifetime-limited linewidth shown in red of Figure 4.5(b). This is obtained by taking the Fourier transform of the lifetime equation $f(t) = A\exp(-t/\tau)$. The real part of the Fourier transform yields

$$g(\nu) = \frac{A}{\sqrt{2\pi}} \frac{1/\tau}{\left(\frac{1}{\tau}\right)^2 + \nu^2} \tag{4.3}$$

where ν is a frequency and $\tau = 2T_1$ is twice the lifetime of an excitonic complex. Previously, we defined the lifetime of an exciton to be τ_x, but here T_1 is for a nonspecific excitonic complex. This Fourier transform equation yields the Lorentzian shape of the linewidth determined by the spontaneous emission lifetime and dephasing time [71]. When pure dephasing is absent, $1/T_2^* = 0$ [71], $T_2 = 2T_1$. This shows a linear dependence of the coherence time on the lifetime of the emission. As such, when plotting the lifetime-limited spectrum of a single excitonic emission, $\tau = 2T_1$.

Of particular interest is comparing the measured linewidth with the calculated lifetime-limited values as shown in the histogram of Figure 4.7(b). Ideally, the ratio of the measured linewidth to lifetime-limited linewidth is 1. A number of factors can play a role in measuring a broadened linewidth. However, since we were able to fit Lorentzians across the

linewidths of all fourteen nanowires, we know that the broadening is not caused by spectral wandering or else that would result in a Voigt profile [90]. Spectral wandering causes random fluctuations in the Lorentzian peak resulting in a Gaussian distribution. We are currently working on understanding the dephasing mechanism causing the broadening on the emission linewidths.

Since the lifetime of the exciton is close to the lifetime of the bulk ($\sim$ns), we can conclude that an adequate normalized diameter was chosen for the growth of this set of nanowires. The lifetime, $T_1 = 1/\Gamma$ is the inverse of the spontaneous emission rate into all the modes of the emitter [34, 71].

Another method to find the single-photon coherence of the exciton emission is to perform a HOM measurement as discussed in section 3.4.5. The results of a HOM measurement give the degree of indistinguishability of the emitter. Dephasing mechanisms lowers the indistinguishability of the emitted photons. The degree of indistinguishability can be defined as $I = T_2/2T_1$. Since photons are only indistinguishable if they are fully coherent, it is an indirect method for measuring the coherence of the emission. The advantage of the HOM indistinguishability measurement is that it is not as strongly affected by the slow component of the lifetime like the one shown in Figure 4.5(a) since it looks at photons emitted consecutively. Due to time constraints, HOM measurements were not taken for the free-standing nanowires discussed in this chapter.

4.2 Single-photon Purity

A pulsed autocorrelation measurement was conducted using a pulsed, above-band excitation (670 nm) with a repetition rate of 40 MHz. The emission from the exciton radiative recombination was spectrally filtered and split into two streams to be measured at two single-photon APD detectors. A coincident count is registered when detection events occur at the start t then stop $t + \tau$ counter. Of particular interest is at zero-delay $\tau = 0$ as $g^{(2)}(\tau = 0)$ gives us the single photon purity of the emitter.

A typical pulsed autocorrelation measurement is shown in Figure 4.8(a) [67]. For an emitter pulsed at a 40 MHz repetition rate, laser pulses are seen 25 ns apart. As the pump power increases, the centre peak also increases. To fit the experimental data, the $g^{(2)}(\tau)$ in the zero-delay peak is simulated using a stochastic model. The model assumes an above-band pulse will always elevate an exciton from the vacuum state to an excited state. In this process, excess free-carriers are generated in the bulk InP material and find their way to the quantum dot where the carriers become trapped. After an exciton recombines and emits, the re-excitation lifetime is the time it takes for another pair of trapped electrons and holes to relax to the s-shell. With increased pump power, the re-excitation probability increases as more free-carriers are generated in the bulk InP and are queuing up to re-populate the quantum dot. This re-excitation accounts for the side lobes around $\tau = 0$ seen in Figure 4.8(b). At $\tau = 0$, for an ideal single-photon source, the dip will go down to zero. As soon as the exciton emits, another pair will quickly try to re-occupy the space. The inner walls of the dip show a probability distribution of this re-excitation lifetime. The outer walls of

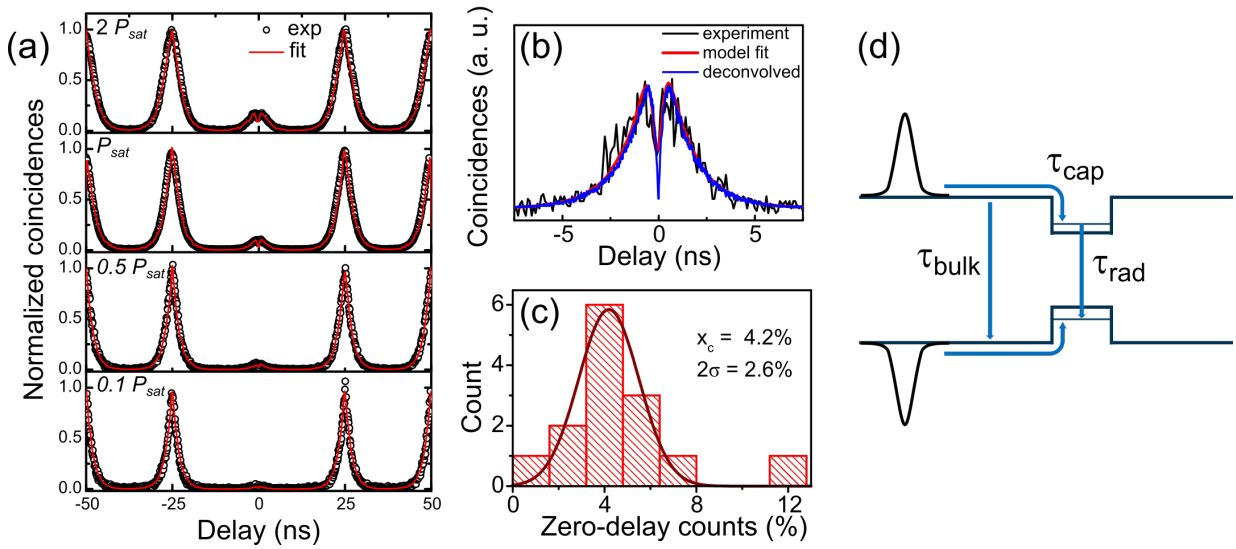

Figure 4.8: **Pulsed autocorrelation measurements**. (a) Power-dependent pulsed autocorrelation measurement of an exciton. (b) $g^{(2)}(\tau)$ measured at P_{sat} showing short-delay bunching. (c) Histogram of coincidence counts at zero-delay normalized to the counts of the side peaks pumped at saturation P_{sat}. (d) Schematic of the re-emission process of carrier decay into lowest level of the quantum dot.

the lobe are associated with the band-to-band recombination which is also referred to as the carrier-decay lifetime. This overall re-emission of photons from the quantum dot varies from dot to dot. This process is shown in the schematic of Figure 4.8(d).

The background corrected $g^{(2)}(\tau)$ in the zero-delay peak for the emission in Figure 4.8(a) is given in Table 4.1. This particular nanowire was chosen as an example to clearly

power	X $g^{(2)}(0)$
$0.1P_{\text{sat}}$	0.026
$0.5P_{\text{sat}}$	0.051
P_{sat}	0.094
$2P_{\text{sat}}$	0.165

Table 4.1: Background corrected $g^{(2)}(\tau = 0)$ for a single quantum dot excitonic complex

show the increase around $\tau = 0$ delay as a function of the pump power. Across the fourteen nanowires in the hundred nanowires array, we measure an average $g^{(2)}(\tau = 0)$ of 0.04 ± 0.03 at saturation pump power P_{sat} as shown in the histogram of Figure 4.8(c). After deconvolving the spectrum with a 200 ps jitter in the detector response time, it was found that at zero-delay, the coincidence counts were all nearly zero after a background subtraction which is expected of single-photon emitting sources. From this, we also know that there is little spectral pollution from neighbouring quantum dots.

4.3 Excitonic complexes

There are more complexes than the one we have looked at so far as mentioned previously in Section 2.3.4. We see in the top panel of Figure 4.9 higher resolution spectra of typical quantum dots pumped at different powers. Within the same growth sample, under the same conditions, with the same nominal geometries, there are differences in the optical properties of the quantum dots. This is due to strong local fluctuations in confining potentials and strain fields [31].

We chose to focus on peaks with three clear, distinct emissions that we believe correspond to the exciton, charged exciton, and biexiton. This section on the identification of each type of excitonic complex will be loosely based on a recently published paper [68] where we looked at 42 nominally identical quantum dots in nanowires with similar emission spectra. Figure 4.10(a) shows a spread of the energy distribution of the 42 quantum dot's complexes. We find that the emission energy of X is $E_X = 1301 \pm 5\,\text{meV}$, for X^- is $E_{X^-} = 1296 \pm 5.6\,\text{meV}$, and XX is $E_{XX} = 1300 \pm 4.3\,\text{meV}$.

At low excitation power, the neutral exciton X and charged exciton X^- are present. Typically X is the dominant intensity at low power [1], however this may not always be the case depending on the charge environment of the nanowire. As the power is increased, the intensity of X^- emission exceeds that of X emission, while the XX emission appears between the X and X^- emissions and overtakes both emission lines. X^- and XX emissions saturate at higher powers, and emission from the p-shell starts to make an appearance. The second column in Figure 4.9 shows an example of a quantum dot behaving as such. As seen in the other three graphs, the X^- emission does not necessarily have to overtake the X emission before it reaches saturation. In fact, the X emission may not be the dominant peak at lowest pump power. Factors that contribute to an extra charge in the quantum dot system include shifts in the Fermi level due to doping of the InP and surface pinning. Potential defect states may provide trapped charge states permanently in the system depending on the proximity of the trapped states to the quantum dot.

There are various different types of experiments that can be performed to determine the identity of each peak. We used power-dependent photoluminescence, auto-correlation $g^{(2)}(\tau)$, and cross-correlation $g^{(2)}(\tau)$ measurements to aid in categorizing the three most common complexes found in our quantum dots. To provide the reader with a fuller picture of the different techniques used to identify excitonic complexes, additional techniques including polarization-sensitive photoluminescence for resolving the fine-structure splitting in certain complexes, photoluminescence excitation (PLE), and gate-control [91] will also be discussed. With the exception of polarization PL discussed later, these methods were not employed in this thesis.

4.3.1 Determining excitonic complexes through photoluminescence spectra

The lower panel of Figure 4.9 shows the PL integrated intensities of each of the three dominant peaks as a function of pump power in a log-log plot. Here, we denote the

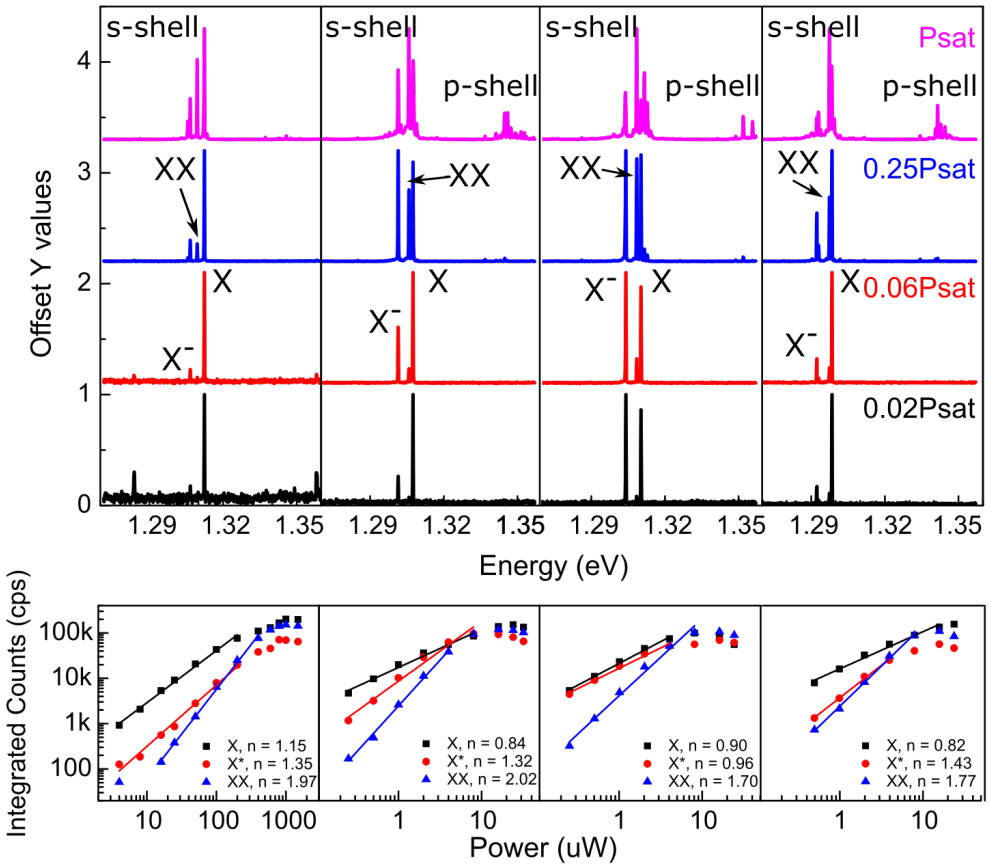

Figure 4.9: **Power-dependent photoluminescence spectra of InAsP quantum dots** grown under the same conditions. The first quantum dot was pumped with a HeNe and others were pumped with a 780 nm laser.

exponent of the exponential fit to the power-dependent peak intensity curve as n. A simplified Poissonian model [1] may be used to calculate the occupation probability of a certain level. It is assumed the PL intensity I_{PL} for a given excitation is proportional to the occupation probability N_n of that level, so

$$N_n = \frac{\langle n \rangle^n}{n!} e^{-\langle n \rangle} \tag{4.4}$$

where n is the energy level filling in which when $n = 1$, N_1 describes the energy filling of X, and when $n = 2$, N_2 describes the energy filling of XX. Note that this n is different from the one used to describe the exponent of the fit for the power-dependence curve above. $\langle n \rangle$ is the average number of excitons created in the quantum dot defined by $\langle n \rangle = N_R \tau_{\text{rad}} \tau_{\text{cap}}$. This value depends on the number of electron-hole pairs N_R created in the quantum dot, the radiative lifetime of the excitonic complex τ_{rad}, and the exciton capture rate τ_{cap} (see Figure 4.8(d)).

Using the relationship $I_{PL} \propto N_n$, we can experimentally obtained N_n, and in so doing, calculate $\langle n \rangle$. This value can be related back to the Poissonian model with

$$\langle n \rangle = \beta P_{\text{exc}}^{\alpha} \tag{4.5}$$

where α and β are constants characterizing the capture mechanism. The constant α here is directly related to the exponent n we obtain from the exponential fits from Figure 4.9(lower) for the X and XX. Typically $\alpha(X) \sim 1$ for X, $\alpha(XX) \sim 2$. However, this Poissonian model does not work for charged excitonic complexes like X^-. We need a correction term γ. Eq. (4.4) then becomes

$$N_n = \frac{(\langle n \rangle^n)^\gamma}{n!} e^{-\langle n \rangle}. \tag{4.6}$$

For the X and XX states, $\gamma = 1$, and for charged states, $\gamma \sim 1.5$ where it can be thought of as one and a half excitons and lies between the X and XX states. Typically $\alpha(X^-) \sim 1.5\alpha(X)$. However, sometimes X and X^- photons can have very similar power dependencies resulting in $\gamma \sim 1$ when the the extra carrier comes from a donor/acceptor impurity.

For the majority of the 42 quantum dots we measured, we were able to make reasonable assumptions on which peak corresponded to what excitonic complex based on their exponent values, n, which loosely matched the theory. A histogram of the slopes we measured for each complex is shown in Figure 4.10 (b). Generally, the biexciton XX photon was the easier to pick out as it only appeared at relatively higher powers and had the largest slope of the three. However, for a few of the nanowires, X and X^- photons had very similar exponents such as the one shown in the third column of Figure 4.9 where $\alpha(X) = 0.90$, $\alpha(X^-) = 1.07\alpha(X)$, and $\gamma = 1.07$.

The power-dependent spectrum is not the most reliable mechanism for characterizing the complexes. One way to distinguish between X and X^- is to look at the anisotropic exchange interaction-induced fine-structure splitting of X. Unfortunately, due to high symmetry of the WZ nanowire quantum dot [31, 100], a spectrometer of much higher resolution than a mere grating spectrometer with a CCD detector is needed to resolve these splittings. An etalon has much higher resolution as discussed previously and can resolve the fine-structure splittings (see Figure 4.12).

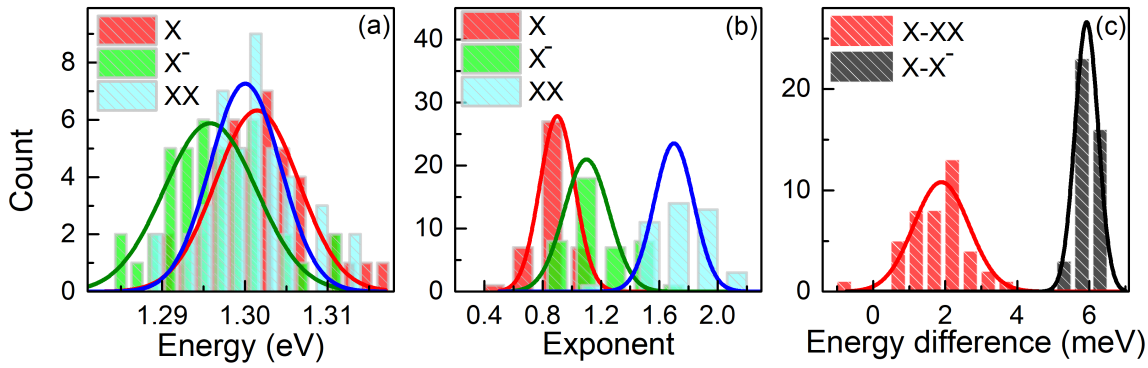

Figure 4.10: **Histogram of excitonic complex distributions.** (a) An energy distribution of different complexes extracted from 42 quantum dots. (b) Histogram of the slopes measured from the integrated intensity of each complex. (c) Histogram of the energy difference between the X-X$^-$ and X-XX emission lines.

4.3.2 Autocorrelation measurements for distinguishing excitonic complexes

To distinguish between the X and X$^-$ states, additional correlation measurements are taken. It is useful to have the image from Figure 2.8 in mind when trying to interpret the results of correlation measurements. Picture spins in the s-shell. A negatively charged exciton X$^-$ has two trapped electrons of different spins and a hole. A neutral exciton has an electron and a hole. If the electron and hole have different spins, they can recombine and emit a photon. The biexciton is made up of two electrons and two holes. By the Pauli-exclusion principle, the electrons and holes at their own respective levels have different spins. Since the biexciton has two recombination pathways, it typically shows a lifetime twice as short as the neutral exciton.

The top panel of Figure 4.11 shows the autocorrelation measurements taken for one quantum dot. Each excitonic complex has its own signature autocorrelation and cross-correlation shapes [63, 98]. The XX photon shows strong bunching at short time delays as the power decreases. The X$^-$ photon also shows bunching at short time delays, however, it is not as drastic as the XX photon. Typically, bunching behaviour is not seen for X photons. However, the width of the anti-bunching dip widens with lower powers. The curves shown for X photons are consistent with the expected behaviour in a two-level system for the ground and excitonic state with $g^{(2)}(\tau) = 1 - e^{-(R+\Gamma)\|\tau\|}$ where R is the pump rate and Γ is the excitonic radiative lifetime [98]. This model predicts that as the pump rate approaches zero, the half-width of the dip is the inverse of the radiative lifetime $1/\Gamma$. On the other hand, as the pump power increases, the width of the dip narrows.

Strong single-photon purity was observed across all three complexes with the X photon having a $g^{(2)}(0) = 0.049$, the X$^-$ photon having $g^{(2)}(0) = 0.058$, and the XX photon having $g^{(2)}(0) = 0.20$.

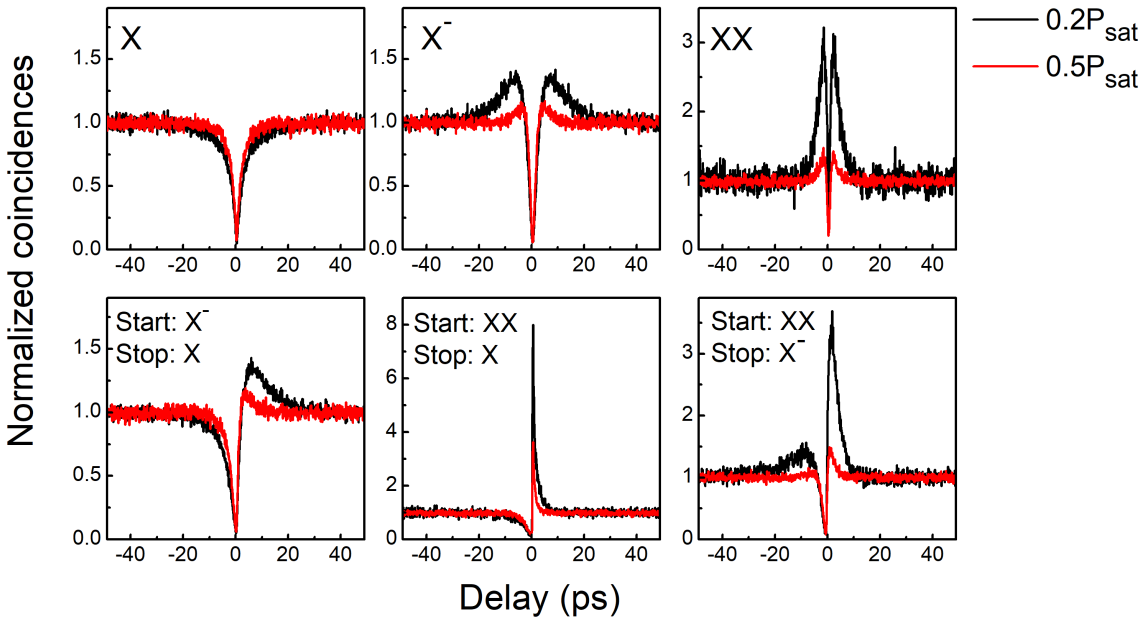

Figure 4.11: **Autocorrelation (top) and cross-correlation (bottom) $g^{(2)}(\tau)$ measurements** of X, X$^-$, and XX. Published in *Appl. Phys. Lett.* 2021, 118, 161107.

4.3.3 Cross-correlation measurements for distinguishing between excitonic complexes

Additional cross-correlation measurements may help distinguish between the X and X$^-$ photons. The lower panel of Figure 4.11 shows the cross-correlation of the complexes from the top panel. The setup for the cross-correlation measurement splits the light emitted from a quantum dot through a beam splitter and send each arm into a tunable filter connected to an APD detector. As before, one detector is the start while the other is the stop. One must be mindful of which detector is set as the start and which is the stop detector to be able to determine which complex corresponds to which emission line. Each tunable filter is set to the emission wavelength corresponding to a complex of interest. If the wavelengths of both filters are set to the same emission line, this is essentially the same as a regular autocorrelation measurement.

A power-dependent cross-correlation is needed to determine the identity of each complex. For each correlation experiment, measurements were taken at pump powers of the exciton P_{sat}, $0.5\,P_{\text{sat}}$, and $0.2\,P_{\text{sat}}$. Since the measurements at P_{sat} exhibit similar bunching behaviour across all three combinations, they were not included in Figure 4.11. Things become more interesting at lower pump powers relative to P_{sat}. We found that, on average, the saturation power of X and X$^-$ were relatively similar but with the X$^-$ having a slightly higher saturation power. XX typically saturate at double the saturation of power of the X photon.

The lower left panel of Figure 4.11 shows the cross-correlation between X and X$^-$ photon.

The X^- photon is sent to the start detector. This means that if we observe a start click, the dot has one electron in it. The X photon is sent to the stop detector which means, given that the dot has a single electron in it, only a single hole has to be captured to register a count. However, for long positive delays, there is no longer a guarantee that the dot has an electron in it, and at very low pump powers, the dot is likely empty. This means that the dot has to capture an electron-hole pair to register a count which is less likely than just capturing a hole. Hence, we see a pump power-dependent bunching at short positive delays. Similarly, at negative delays, no bunching is observed as the dot is empty having just detected an X photon.

The lower middle panel shows a cross-correlation between an XX and X photon. The XX photon is sent to the start detector and the X photon is sent to the stop. In this case, we observe an asymmetric bunching behaviour expected from a cascaded emission process [78, 80]. The XX photon are emitted first, followed by the X photon such that at $\tau = 0^+$, the emission is bunched, whilst at $\tau = 0^-$, the emission is antibunched. In other words, having just detected an XX photon, it is very likely that we will detect an X photon. Conversely, if we have just detected an X photon, the dot is empty, and the emission is antibunched. Similar observations were reported in [98, 78, 63].

Lastly, the lower right panel shows the cross-correlation between the X^- and XX photons. In this case, the XX photon is sent to the start, and the X^- photon is sent to the stop. For positive delays, given that we have just detected an XX photon, the dot contains one electron-hole pair and requires the capture of an electron to populate the dot with X^-. This is more likely than the case of an empty dot which requires the capture of two electrons and a hole such as in the case at $\tau \gg 0$. Hence we see a power-dependent bunching at short positive delays. Similarly, for $\tau < 0$, having just detected an X^- photon, the dot contains one electron and requires two electrons and a hole to populate XX. This is more likely than the case of an empty dot which requires the capture of two electrons and two holes as is the case at $\tau \ll 0$. Hence we see a power-dependent bunching at short negative delays.

4.3.4 Other methods for characterizing excitonic complexes

There are still more ways to distinguish between the neutral X, charged X^*, and XX excitonic states including measuring the exchange splitting found in X and XX (but not in charged excitons), using resonant excitation, and gate-controls. We perform the first and briefly describe the latter two, as it is important to consider other experimental methods to help us gain a broader understanding of the properties of each complex.

Fine structure splitting

It has already been mentioned that it is rather easy to identify the XX photon distinctly from the X and X^- photons by simply taking a power dependent PL of the quantum dot emission. The biexciton photon typically shows up later and quickly rises relative to the other two peaks. There are yet more ways to distinguish between X and X^- photons using

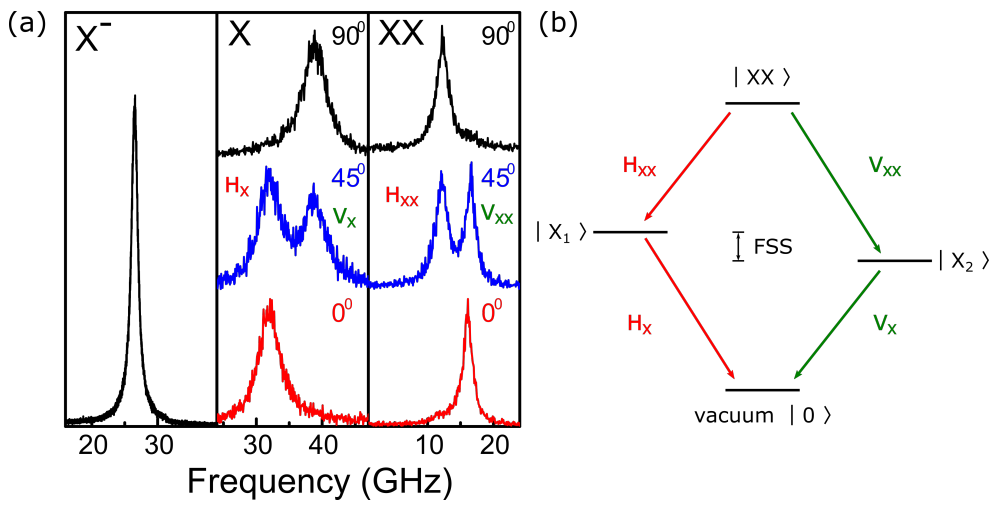

Figure 4.12: **Fine-structure splitting.** (a) High-resolution spectrum of the X^-, X, and XX of a quantum dot taken at three different polarizations showing the fine-structure splitting of the latter two. (b) Schematic of biexciton-exciton cascade. The exciton state is split into two polarization states $|X_1\rangle$ and $|X_2\rangle$ with a fine-structure splitting between the two states.

PL thanks to electron and hole exchange interactions [71]. Both the exciton (X) and biexciton (XX) have anisotropic exchange splittings whereas the charged exciton (X^-) does not [12]. We show this splitting in Figure 4.12(b). The CCD detector with a 1200 g/mm grating is unable to resolve this splitting in X and XX whereas an etalon with a detector can [49].

Incorporating the use of polarization-sensitive PL measurements is one way to resolve the fine-structure splitting of excitonic doublets. The peak of each doublet corresponds to orthogonally (horizontal H and vertical V) polarized emissions (see Figure 4.12(a)). By using a half-wave plate in front of a polarizer to control the angle while tracking the peak energies, a sinusoidal change in the peak energies can be observed. The fine-structure splitting of the two complexes can then be calculated by taking the height of the sinusoid [32]; no such sinusoidal behaviour is observed when tracking the peak emission of a charged exciton [12, 32, 91]. Typically, this splitting is in the few μeV range [49].

Quasi-resonant and resonant excitation

For strictly resonant excitation, the basic principle involves tuning a laser energy to directly generate an electron-hole pair inside the quantum dot. In this scenario, the only possible states are an empty-dot state $|0\rangle$ and an excited one-exciton state $|X\rangle$. Typically, a charged exciton is not possible in this pumping regime unless a trapped state in the WZ crystal of the nanowire is supplying the quantum dot with either an extra electron or hole.

Two-photon excitation can also be performed to coherently populate the biexciton. Recall in Figure 2.8, a biexciton has two electron-hole pairs. An excitation laser of energy half that of the energy between the biexciton $|XX\rangle$ and ground $|0\rangle$ states is used to promote

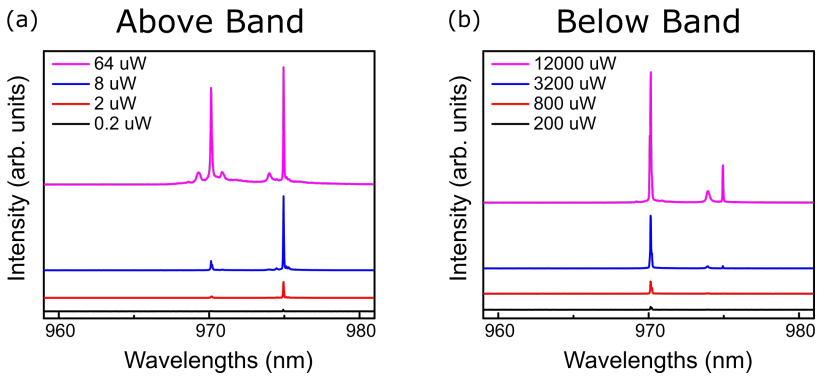

Figure 4.13: **Quasi-resonant excitation.** (a) Above-band power-dependence of a quantum dot. (b) P-shell pumping power-dependence of the same quantum dot.

electrons from the ground state $|0\rangle$ [55]. In a biexciton–exciton cascaded emission process, the rate at which X and XX are detected is the same as a function of pump-power [72]. It should be noted that charged excitonic states are still possible in a two-photon excitation regime.

A quasi-resonant excitation measurement was taken for a quantum dot from the array of a hundred nanowires from the first half of this chapter. To perform quasi-resonant excitation, the pump power is tuned to the p-shell of the quantum dot. This reduces the number of relaxation processes the trapped electron and holes have to undergo to reach a ground state. The power-dependent PL spectra of one of the quantum dots is shown in Figure 4.13 for above (a) and below (b) band excitation. In above-band excitation, the quantum dot was excited using a CW 780 nm laser whereas the below-band excitation used a tunable laser set to one of the p-shell emission peaks. Peaks are found at 970 nm and 975 nm. From the power-dependence, it appears that the 970 nm emission is the charged exciton, and the 975 nm peak is the neutral exciton. However, that would mean the charged exciton is dominant in the below-band excitation case even at low powers, whereas the neutral exciton emission is greatly suppressed. More research needs to be done to better understand what may be the potential cause. What we do know is that the average charge occupation of the dot is dependent on the excitation scheme.

Quasi-resonant pumping is not without its flaws. During this multi-step relaxation process, lattice defects and doping within the nanowire may create trapped states energetically located between the p and s-shell. As a result, electrons or holes may be held at these traps and injected into the system at a random time. Further studies need to be conducted to better understand why trapped states are possible during quasi-resonant excitation. To eliminate the possibility of charge states, resonant pumping with a laser of the same energy as X reduces this back to a single-step relaxation process.

Gate-controlled quantum dot

Reimer *et. al.* [91] were able to control the electron charge within an InAsP/InP quantum dot using four Schottky metallic gates around an InP pyramidal nanotemplate. By tuning

the reverse-bias voltage, the discrete changes in the excitonic emission corresponding to the neutral exciton, the singly charged exciton, and the doubly charged exciton were observed.

4.4 Summary

In this chapter, we measured the emissions from 100 nominally identical nanowires with quantum dots designed to emit around 980 nm. This set of quantum dots had an average collection efficiency of 31.2%. An etalon was used to measure the average linewidth of $\Delta\nu = 0.87 \pm 0.36$ GHz across the set. The set had an average $g^{(2)}(\tau = 0)$ of 0.04 ± 0.03 which translates to a single-photon purity of $96 \pm 3\%$.

We also discussed the different types of excitonic complexes found in the quantum dot system. Particular attention was paid to quantum dots that emitted three distinct emission peaks corresponding to the neutral exciton, charged exciton, and biexciton. There are different ways to distinguish between the different complexes. The two methods we employed included 1. comparing the exponential increase in the intensity as a function of pump power between different emission lines, and 2. using the characteristic autocorrelation and cross-correlation behaviours to determine the identity of the complex.

Nanowires on a substrate are limited to a vertical emission direction. However, most current integrated photonic circuit designs are planar. By placing the nanowires horizontally on SiN ridge waveguides, it is possible to optically pump the nanowires on chip from multiple directions including from the tapered end as before, from the base, or even sideways. The realization of such a design is discussed in following next chapter.

Chapter 5

Optical Properties on Waveguides

Optical waveguides are to optical integrated circuits as metallic strips are to electrical integrated circuits. It is a fundamental element that connects various devices forming an optical integrated circuit. Instead of electrical current flowing through its circuits, optical waves in distinct modes travel through optical waveguides. In the case of a rectangular waveguide, a wave propagates along its length and is confined by the difference in the refractive index to its surroundings. The number of modes supported in the waveguide depends on the effective index, the dimensions of the waveguide, and the wavelength of the injected light.

An integrated photonic platform is a practical way to move quantum technologies out of the lab and into the real world. A properly designed waveguide for the integration of pure single-photon sources is necessary for widespread implementation of more complex photonic integrated circuits. A free-space, optical setup requires regular alignment which makes it difficult for transitioning outside the lab setting. Switching to an all-fibre setup allows for the transmission of light over long distances. A fibre-based integrated photonic platform is more stable, scalable, and portable than a free-space setup. In particular, a waveguide-fibre coupled approach opens the door for manipulating light in a photonic integrated circuit. On-chip integrated sources include quantum dots coupled to ridge waveguides, nanobeams, and photonic crystal waveguides. We use a hybrid approach of deterministically place a III-V nanowire made of InP with an embedded InAsP quantum dot on a SiN ridge waveguide. In this chapter, we will discuss whether our integration approach is a viable platform for generating single photons. We will first discuss losses which include coupling, scattering, and absorption losses, of which the last two fall under propagation losses. Coupling losses occur at the fibre-SiN waveguide facet interface. These losses, as well as techniques used to maximize coupling, are presented in Section 5.1. We then discuss how this loss changes when a III-V nanowire is placed on to the waveguide structure. Particularly, we are interested in knowing if the source efficiency of the device is impacted after transfer. We conduct much of the same measurements as in **Chapter 4** and discuss whether the optical properties of the quantum dot emission are maintained.

5.1 Loss in Optical Waveguides

5.1.1 Types of loss through a waveguide

Loss in a waveguide is generally attributed to three mechanisms including scattering, absorption, and radiation [56]. Depending on the material of the waveguide, different contributors of the loss dominate. For example, scattering losses are usually predominate in glass and dielectric waveguides, absorption losses predominate semiconductor and crystalline material waveguides, and radiation losses occur when a waveguide is bent through a curve. It is helpful to understand these losses by thinking of light quantum mechanically.

Scattering Losses

The two types of scattering loss in an optical waveguide are volume scattering and surface scattering.

Volume scattering occurs due to light scattering off the imperfections within the volume of the waveguide. These imperfections come in the form of voids, contaminant atoms, and crystalline defects. The loss per unit length is proportional to the number of imperfections inside the waveguide per unit length and the relative size of the imperfections themselves compared to the wavelength of the guided light. For modern waveguides, this is typically a negligible problem since the volume imperfections are negligible compared to the surface scattering loss.

Surface scattering losses, as the name suggests, occur on the surface of the waveguide. They can be significant even for relatively smooth surfaces because propagating waves interact strongly with the surface of the waveguide especially at higher order modes or modes that are not well-confined. To understand why, imagine a light ray bouncing within a waveguide. Scattering loss occurs with each reflection the ray undergoes. The number of reflections from each surface the ray bounces off of is given by

$$N_R = \frac{L}{2t_g \cot\theta_m} \tag{5.1}$$

where N_R is the number of reflections from each surface of a waveguide, L is the length of the waveguide, t_g is the thickness of the waveguide, and θ_m is the angle at which the wave is travelling relative to the direction of propagation. Generally, θ_m is larger for higher order modes thus resulting in greater surface scattering losses. For our waveguides with thickness $t_g = 485\,\text{nm}$, $L = 5\,\text{mm}$, and using $\cot(\pi/2) = 1$ for simplicity, we calculate $N_R = 5155$ reflections. Since losses occur with every reflection, the total surface scattering loss quickly adds up. Generally, the intensity of at any point in the waveguide is described as an exponential decay

$$I(z) = I_0 \mathrm{e}^{-\alpha z}, \tag{5.2}$$

where I_0 is the intensity at $z = 0$ and α is an attenuation coefficient [56]. This type of loss is more prevalent in dielectric film waveguides than semiconductor waveguides. For semiconductor waveguides, such as SiN waveguides, absorption losses are much larger compared to surface scattering losses.

Absorption Losses

Absorption losses occur when the signal is dissipated through the conversion from electromagnetic energy into other forms of energy as it interacts with the material of the waveguide [56]. There are several types of absorption processes (e.g. intraband, interband, defects) that can lead to losses. Ideally, a high, optical-quality material should be used at appropriate operating wavelengths where the transmission is very high.

Radiation Losses

Radiation losses occur when photons are emitted into the surrounding media of the waveguide. Typically, this type of loss is negligible for well-confined modes. As the waveguide becomes larger and supports higher-order modes, this type of loss becomes more prevalent. However, radiation losses are more prominent at the curve of a ridge waveguide [56]. This is notably the case when handling fibre optics where introducing a bend less than the allowable radius of curvature of the fibre not only potentially damages the fibre but also causes more loss of power transmitted through the fibre. When designing ridge waveguides on chip with a curve, a quick and easy way to analyze the potential radiation loss is with the equations [73, 56]

$$\begin{aligned}(R + X_r)\frac{d\theta}{dt} &= \frac{\omega}{\beta_0}, \\ R\frac{d\theta}{dt} &= \frac{\omega}{\beta_z},\end{aligned} \tag{5.3}$$

where R is the circular bend of the waveguide, $(R + X_r)$ is maximum allowable bend in the radius before the phase velocity of the medium exceeds the velocity of the of unguided light in the material surrounding the waveguide, β_z is the propagation constant of light within the guiding material, β_0 is the propagation constant of the unguided light in the surrounding material, and X_r is defined as $X_r = (\beta_z - \beta_0/\beta_0)R$. A large difference in the index of refraction between the waveguide medium and surrounding medium helps minimize the effects of radiation loss.

5.1.2 Measured loss through SiN waveguides

When coupling an optical fibre to a ridge waveguide, there will naturally be losses in the system. All measurements in the following are made on high-quality LPCVD SiN waveguides fabricated using the Damascene process from a commercial foundry (LIGENTEC). The LPCVD method ensures low absorption. The coupling of the mode from a fibre to the waveguide may not be perfect. The resulting loss is referred to as insertion loss and can occur at the interface between fibre to fibre or fibre to waveguide. Insertion loss is either caused by alignment errors (i.e. lateral offset, a tilt, or a gap) or mode mismatch [65].

There are three main approaches for achieving a high coupling efficiency between an optical fibre and a ridged waveguide on chip [101]. The first is using a grating coupler

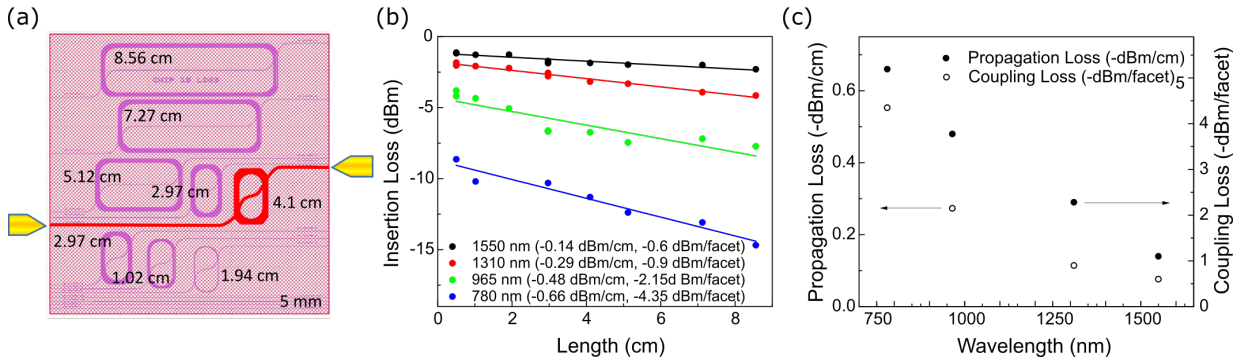

Figure 5.1: **Loss through a waveguide.** (a) Layout of chip used to calculate the propagation loss for an waveguide of given lengths. A path is shown in red to highlight how lensed fibres are used to pump and collect light from one such path. (b) Insertion loss as a function of the length of the waveguide. (c) Extracted propagation (left) calculated from the slope in (b) and the coupling loss at each facet (right) as a function of the wavelength.

where light from the optical fibre is launched at a diffracting grating at an oblique angle. The light is collected by the grating and injected into the waveguide [27]. This method is typically used to launch light from a single-mode, optical fibre to a multi-mode waveguide. A mode converter at the other end of the waveguide converts the light into the single mode necessary for coupling back into an optical fibre. However, extra losses are incurred in the process [111]. To combat this issue, the second approach for achieving high coupling efficiency uses a waveguide tapered at both ends. This design is based on the matching of the mode profiles between the fibre and waveguide. This can be implemented using either a cleaved fibre having a flat 90° face placed flush against the waveguide facet or using a lensed fibre. The third approach uses the evanescent coupling of a lensed (single-sided conically tapered) fibre placed next to a SiN waveguide [79]. Due to the ease of coupling, we use lensed fibres with tapered, SiN waveguides for the following experiments.

For our experiments, we use a narrower definition of insertion loss. We consider the loss through the two lensed fibres coupled together to be the system loss (typically $-0.2 \sim -0.4$ dBm). By inserting the SiN waveguide between the fibres, we introduce an insertion loss. First, we are interested in knowing the insertion loss through waveguides of varying lengths. We send 1 mW of laser light through one lensed fibre into the waveguide, and measure the power collected into a second fibre to obtain the total measured loss. Figure 5.1(a) shows a schematic for the type of chip used to measure the loss through waveguides of lengths ranging from 5 mm to 8.56 cm. One such waveguide complex is highlighted in red to show the path the laser light travels as it enters through one facet and out the other. We used four different lasers of wavelengths 780 nm, 985 nm, 1310 nm, and 1550 nm. For each wavelength, different fibres were used to measure the wavelength dependence through each waveguide, the results of which are shown in Figure 5.1(b) and (c). These four laser wavelengths were chosen because 780 nm is the typical laser used throughout our experiments for above-band excitation of a quantum dot, 985 nm is close to the emission wavelength of the quantum dots of interest we studied, and 1310 nm and 1550 nm are typical telecom wavelengths of interest. Although some quantum dots emitting in the

telecom range were studied, they are not discussed in this thesis. The insertion loss was calculated by subtracting the system loss from the total loss measured through the system. Propagation and coupling loss at each facet can be derived for each wavelength. The propagation loss in the form of scattering, absorption, or radiation is the loss incurred as the laser light travels through the length of the waveguide. This is obtained using the slope of the insertion versus length graph. Coupling loss per each facet is calculated by taking half the y-intercept of each fit. For our waveguide structures, we find that the insertion losses are generally lower with longer wavelength lasers due to better mode matching for those lensed fibres-tapered waveguide combinations.

5.2 Directional dependence of nanowire coupling to SiN waveguides

Much work has been done characterizing the optical properties of nanowires on their growth substrate [32, 34, 67]. It was mentioned in Section 2.4.1 that half the emission from the quantum dot that couples into the fundamental HE_{11} mode of the nanowire waveguide is emitted towards the base and the other half towards the taper. Since our nanowires do not have a reflective coating at the base, normally the half emitted downwards towards the base is counted as loss. However, with the nanowire now placed planar on the ridge waveguide, collection from both ends of the nanowire becomes available. We also mentioned in Section 2.5 that the length of the taper plays an important role in the coupling of nanowire mode to the ridge waveguide mode. The quantum dots are placed ~ 1 μm up from the base of the nanowire. The base of the nanowire does not have a taper, so it would be expected to have a much lower collection efficiency at the base than the at the taper. In this section, we attempt to verify this hypothesis that there is a strong dependence on the collection efficiency based on the collection direction from the nanowire.

5.2.1 Evanescent Coupling

Previous attempts to integrate III-V nanowires with SiN waveguides include etching the waveguide around a nanowire placed on a SiO_2-coated silicon substrate and encapsulating the nanowire in SiN [38, 110]. This method resulted in collection efficiencies of $\sim 24\%$. The authors found similar collection efficiencies from both ends of the nanowire. Note the nanowire is *in* the waveguide and hence does not utilize taper-mediated, evanescent coupling as we do here.

Simulations of a tapered, InP nanowire on a SiN waveguide in Figure 2.13 showed that a sufficiently long taper ($> 10\,\mu$m) is necessary for the efficient coupling ($> 90\%$) of the nanowire mode into an underlying waveguide with minimal scattering into higher order modes. We investigate this theory by measuring and comparing the collection efficiency of the quantum dot emission from both ends of the nanowire after it has been placed on the waveguide. Knowledge of the loss through the waveguide is needed when calculating the efficiency of the overall system and calculating the brightness of the quantum dot emission.

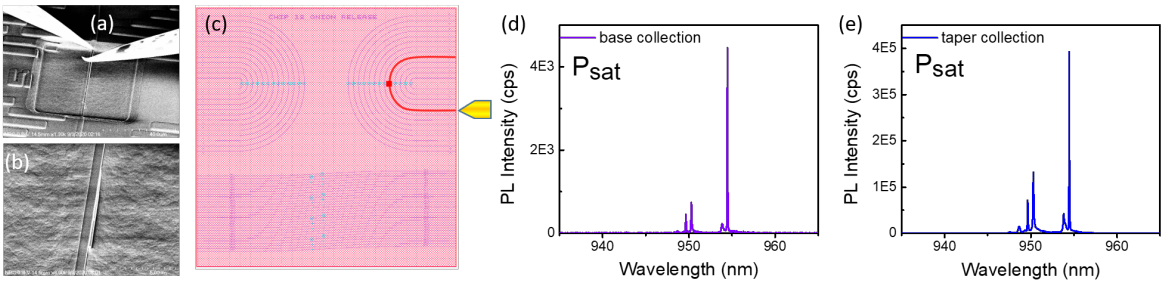

Figure 5.2: **Photoluminescence spectra of a quantum dot nanowire on a curved SiN waveguide** measured at saturation. (a) SEM of a nanowire placed in an exposed section of a SiN waveguide. (b) SEM of nanowire on a SiN waveguide at higher magnification. (c) Design of the chip containing semi-circular ridge waveguides. Unmasked sections of SiN waveguides are shown in blue boxes. Laser light was pumped and dot emission was collected from the same lensed fibre. (d) PL of quantum dot emission from base end of nanowire. (e) PL of quantum dot emission from taper of nanowire.

In the aforementioned method, the group used a micro-manipulator to position their nanowires, and their waveguides were fabricated in house. Our approach uses nanomanipulator probes to precisely place the nanowires directly on waveguides fabricated by a specialized foundry (LIGENTEC). To protect the waveguides, a layer of SiO_2 is deposited over the surface of the entire chip. Openings are made to expose parts of the waveguide. It is at these openings that we place the nanowires. An advantage to this method is having the photonic integrated circuit fabricated by external companies specialized in SiN foundries techniques. The waveguides and facets exhibit less loss than the ones made in house at NRC. Details regarding the waveguide fabrication process can be found in Section 2.5.

To ensure the propagation loss is the same when collecting from either end of the nanowire, the nanowire is placed inside an opening in the SiO_2 located at the centre between the ends of the curved and straight waveguides shown in Figure 5.2(c).

5.2.2 Photoluminescence

Photoluminescence collection from taper and base of nanowire

Figure 5.2(d) and (e) show the spectra of one of the nanowires on a curved waveguide of $L = 0.32\,\text{cm}$ measured at saturation from the base and taper, respectively. A Lorentzian fit is taken of the peak of interest to calculate the integrated intensity of the peak. The width of the emission lines are $\sim 0.04\,\text{nm}$, though this is limited by the resolution of the silicon CCD spectrometer. From the base, the brightest peak at 954 nm has an integrated PL intensity of 12.3 kcps, and from the taper, the brightest peak has an integrated intensity of 1057 kcps. This gives a factor of $\sim 86\times$ greater coupling efficiency from the taper versus the base. From 16 different nanowires placed along the middle of a waveguide, we found that the collection from the tapered end of the nanowire was always greater. Of the three

nanowires on curved waveguides we measured, this factor ranged from 30 $\sim$ 86×. Table 5.1 summarizes the integrated intensities obtained when collecting from the base and tapered ends of the nanowire.

Nanowire (#)	from taper (kcps)	from base (kcps)	ratio (taper/base)
1	145	3.24	45
2	191	6.27	30
3	1057	12.3	86

Table 5.1: Intensity of InAsP quantum dot X emission from three different wurtzite InP nanowires on a curved SiN waveguide comparing the collection from the base versus the tapered end of the nanowire.

We focus on the brightest of the three nanowires to obtain the collection efficiency of the quantum dot. Instead of using the a silicon CCD spectrometer, here we use a tunable filter set to the brightest emission line (954 nm) and an APD detector to measure the count rate. Figure 5.4(a) shows the same spectrum as before, but this time indicating that we are interested in one particular wavelength $\lambda = 954$ nm. As a comparison with the spectrometer, we again pump the system with a 780 nm, CW laser to obtain the integrated counts versus pump-power curve as shown in Figure 5.4(b).We obtain 1112 kcps from the taper and 12.6 kps from the base which gives a ratio of $\sim$ 88× which is fairly consistent with the value above of 86× obtained by integrating the CCD PL counts.

Loss through fibre

The initial evaluation of the efficiency of nanowire-waveguide structures was performed using a nanowire on a curved waveguide as in Figure 5.2. We pump the nanowire through the taper with the pulsed diode laser operating at a wavelength of 670 nm and a repetition rate of 80 MHz. We collect from the same facet and measure 88 kcps at saturation. To estimate the relevant efficiencies, we first determine all the losses in the optical setup. To do this, we use a 965 nm laser set to 1 mW and measure the loss of laser power through each fibre component using a ThorLabs PM100D optical power monitor. The conversion between loss in dBm (x) and transmission as a percentage (k) is given as $k = 10^{x/10}$ or $x = 10 \log_{10} k$.

First, we consider the facet loss and the propagation loss through the curved waveguide (from facet to waveguide opening in which the nanowire is placed) with a length $L/2 =$ 0.16 cm. From Figure 5.1(b), this corresponds to a facet loss of -2.15 dBm and a propagation loss of $L/2 \times -0.48$ dBm/cm $= -0.077$ dBm.

Next, we consider losses related the fibre mating sleeves and fibre feedthroughs. There was a loss of ~ -2.0 dBm from each lensed fibre going into the cryostat setup (feedthrough loss). To measure the system loss, we maximized the coupling of laser light going from the tip of one lensed fibre to the other and measured the loss to be ~ -8.8 dBm. Since we are only considering collection through one facet with one fibre, the loss through the fibre and feedthrough is halved (-4.4 dBm).

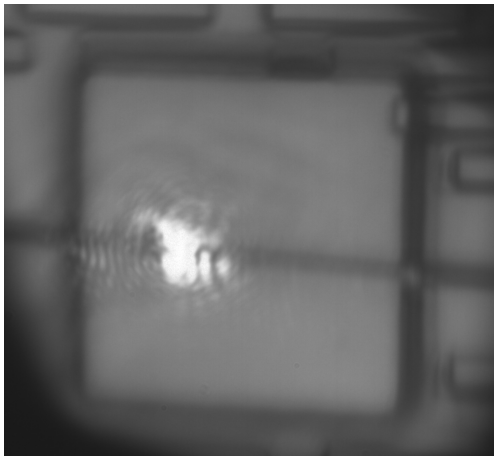

Figure 5.3: **Optical image showing laser light scattered off a nanowire on a straight SiN waveguide.**

Finally, we have to include the throughput of the tunable, optical filter from WL Photonics Inc. which has a loss of $\sim -2.54\,\mathrm{dBm}$ (56% transmission). These losses are summarized in Table 5.2. Both the percentage of light transmitted and the loss in terms of -dBm are provided to give the reader a sense of how to interpret between the two.

If we multiply the percentages of transmitted emission through the optical system, we have a resulting throughput transmission of $\eta_t = 12.1\%$. We also have to include the APD detector efficiency which is wavelength-dependent. In the case of the 955 nm emission from the quantum dot, this efficiency is $\eta_d = 25\%$. Factoring all the losses from our system, we measure a total transmission of 3.0%. To calculate the source efficiency, we take the total number of emitted photons at first lens ($0.088\,\mathrm{Mcps}/0.030 = 2.91\,\mathrm{Mcps}$) and divide by the repetition rate of the pulsed laser (80 Mcps). This gives a resulting source efficiency of 3.6%.

Source of loss	Transmission (%)	Loss (-dBm)
detector efficiency	25	6.021
propagation loss	98.2	0.077
loss at facet	60.95	2.15
loss through fibre + feed through	36.3	4.4
tunable filter (950 nm)	55.7	2.54
throughput	12.1	9.17
Optical system efficiency	3.0	15.19
emission direction	50	3.01
$\beta_{\mathrm{HE}_{11}}$	95	0.223
filtered phonons	80	0.97
Factor for calculating η_{coll}	1.15	19.4

Table 5.2: Losses through the system when measuring a nanowire on a curved waveguide of length $L/2 = 0.16\,\mathrm{cm}$. (For an operating wavelength of 955 nm)

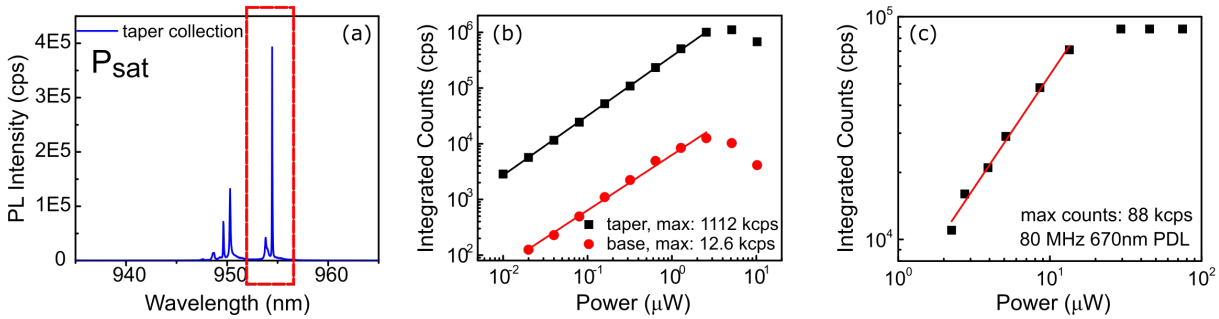

Figure 5.4: **Photoluminescence of a quantum dot-nanowire device on a semi-circular waveguide.** (a) PL spectra of nanowire pumped above band at saturation power. (b) Log-log power-dependent intensity of emission (red box) collected from the taper (black) and base (red) pumped above-band with a CW laser. (c) Log-log power-dependent intensity for the same emission peak pumped above-band at a 80 MHz repetition rate with a pulsed laser.

We also want to know what percentage of emitted photons from the collection end of the nanowire make it to the detector. To calculate the collection efficiency from the nanowire-SiN waveguide hybrid device, we need to consider three other factors. First is the loss of half the emitted photons due to emission in either direction of the nanowire, second is that $\beta_{\mathrm{HE}_{11}} = 95\%$ and corresponds to the percentage of dot emission coupled to the nanowire waveguide HE_{11} mode, and third is that only 80% of the emission reaches the detector due to a filtering out of 20% emitted into phonon sidebands. Taking into account all these, we arrive at a total transmission of 1.15%. Using this transmission, we calculate the total number of emitted photons by the quantum dot at 955 nm to be (0.088 Mcps/0.0115 = 7.65 Mcps). Again by dividing this total by the repetition rate, we get a collection efficiency of 9.6%.

It is difficult to make the same calculations for base collection because of the way the nanowires are broken at the base upon extraction from the growth substrate with a nanomanipulator probe. The growth process of the nanowire may also cause asymmetry at the base. Though effort was make to avoid using nanowires with an obvious asymmetry, we were only able to make our judgement based on viewing the nanowires from one side. It is also possible that the base did not break off cleanly thus causing more scatter into higher order modes as it couples into the waveguide. Overall, the nanowires were simply not designed to be collected from the base. It is unknown why there is such a huge discrepancy between maximum counts from quantum dot to quantum dot even when collecting from the tapered end.

Further studies were conducted on nine different nanowires on straight waveguides. The nanowires were placed either beside or on top of SiN waveguides during the transfer process. There was no significant difference in the count rates between the two orientations. However, in every case, collection from the tapered end of the nanowire showed a much higher ($10 \sim 240\times$) collection efficiency from the tapered end. From the results, it is clear that the taper is vitally important for maximizing the collection efficiency from the

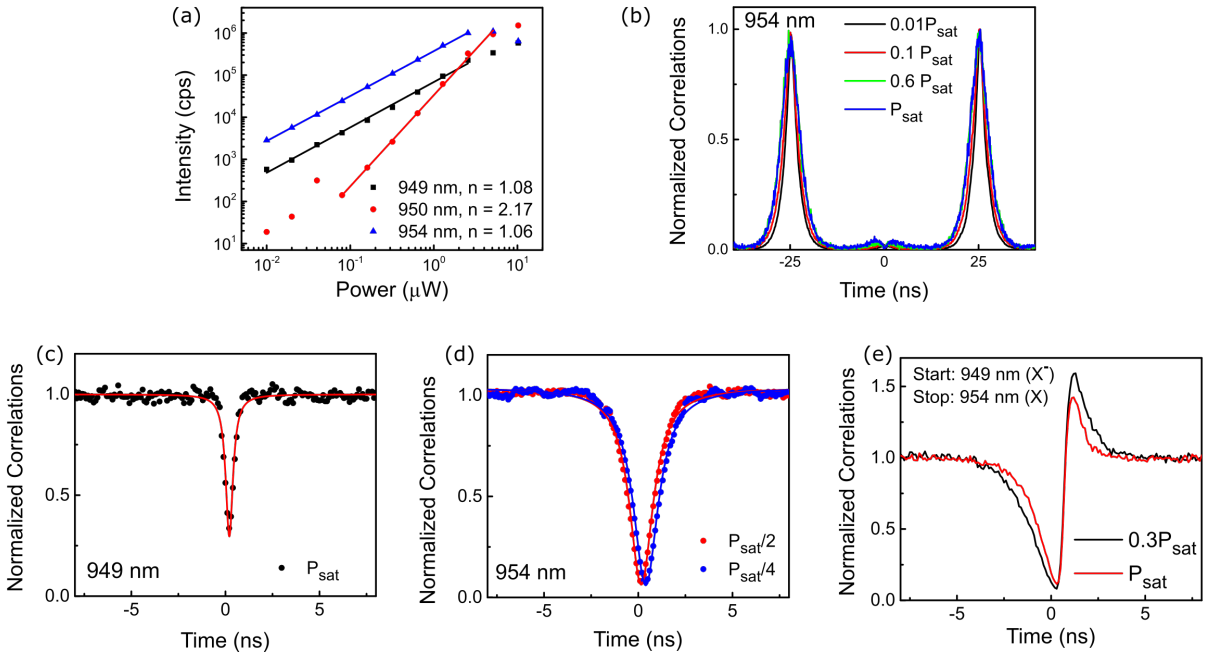

Figure 5.5: (a) Power-dependent PL integrated intensities of 3 dominant peaks X, X^-, and XX. (b) Power-dependent pulsed auto-correlation measurement of X complex. Power-dependent second-order autocorrelation measurement of (c) exciton and (d) charged exciton. (e)Power-dependent cross-correlation between X and X^- for a quantum dot on a curved SiN waveguide.

quantum dot to the SiN waveguide.

5.2.3 Autocorrelation measurements

We continue to investigate the brightest quantum dot on the curved waveguide by looking next at the single-photon purity of the emitted photons. A power-dependent pulsed auto-correlation measurement on the brightest peak (954 nm) is shown in Figure 5.5(b). It can be seen that the quantum dot shows strong anti-bunching with a $g^{(2)}(0) = 0.046$ at saturation indicating it is working as a good single-photon emitter with a purity $> 95\%$. Using a CW laser to excite the quantum dot, we measure $g^{(2)}(0)) = 0.040$ for the same emission peak at saturation, consistent with the pulsed $g^{(2)}(0)$ measurement.

There appears to be three dominant peaks at 949 nm, 950 nm, and 954 nm. Taking a power-dependent PL spectrum yields integrated intensities with exponents $n_{949\text{ nm}} = 1.08$, $n_{950\text{ nm}} = 2.17$ and $n_{954\text{ nm}} = 1.06$, respectively, as shown in Figure 5.5(a). Since the biexciton peak is not prominent until higher energies, the first three measurements at lower energies are omitted from the fitting routine. Apart from the biexciton at 950 nm, it is difficult to determine the identity of the other two complexes through a power-dependent PL alone. To determine the identity of the remaining two complexes, auto-correlation measurements were taken. Typically, the neutral exciton has a wider dip in the $g^{(2)}(0)$

than both charged excitons and biexcitons as seen in Figure 5.5(d). From the power-dependent PL measurement, we know the peak at 950 nm is most likely a biexciton. A bunching effect at $\tau = 0$ is not always evident in a $g^{(2)}(0)$ measurement of the charged exciton. Only the $g^{(2)}(0)$ at saturation was taken for this peak as shown in Figure 5.5(c) which makes it difficult to conclude the identity of this complex.

A power-dependent cross-correlation measurement was taken of the two complexes to determine which is the neutral and which is the charged exciton and shown in Figure 5.5(e). The 954 nm emission was chosen to be the start and 950 nm emission was chosen as the stop. There is some ambiguity in whether we were actually on the 949 nm peak or 950 nm peak since their emissions are quite close. Without further measurements at even lower powers, it is difficult to definitively say whether the 949 nm peak is a charged exciton or biexciton. We are inclined to believe that this is a charged exciton because the $g^{(2)}(\tau > 0)$ should increase more drastically with lower pump powers if it were a biexciton.

5.3 Study of wurtzite InP nanowire with embedded InAsP quantum dot on straight SiN waveguide

So far, we have shown a directionality associated with the efficient coupling of a nanowire to a SiN waveguide from the taper and base. Half racetrack shaped waveguides were used in the above experiments to minimize the collection of scattered laser light travelling in the oxide layer of the chip. Collection from the taper showed at least 10 times higher coupling efficiency compared to collection from the base. We proceed to do a more in-depth analysis of a nanowire on a "straight" SiN waveguide to compare with the free-space measurements taken in the previous chapter. From Figure 5.2(c), it is evident that the waveguide is not actually straight, but has a gradual bend around the centre. It shares the similar purpose of reducing coupling of the scattered laser light in the oxide layer to the lensed fibre. For the sake of simplicity, it shall be henceforth referred to exclusively as the "straight" waveguide.

The quantum dot-nanowire device chosen for this study shows the brightest emission peak of all the other nanowires studied so far with the benefit of a relatively clean emission, making it a good candidate to study. We again perform PL measurements with both a spectrometer and etalon to measure the quantum dot's brightness and linewidth. Additionally, time-resolved PL measurements are used to determine the emission's lifetime and the lifetime-limited emission linewidth in an ideal case. We also perform auto-correlation measurements to determine the quantum dot's single-photon purity. Lastly, we measure the quantum dot's indistinguishability through a HOM measurement which was not present in the previous chapter. Through these experiments, we hope to show the effectiveness of coupling our nanowires to SiN waveguides.

5.3.1 Photoluminescence

The photoluminescence of the quantum dot tells us a lot about the quality of the emitter. The power-dependent PL of the quantum dot of interest is shown in Figure 5.6(a). There

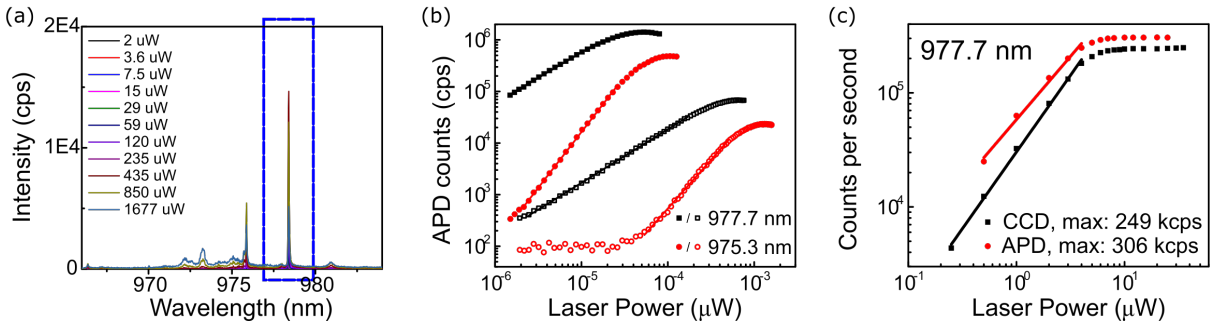

Figure 5.6: (a) Power-dependent PL of a nanowire on a straight SiN waveguide. (b) Power-dependent APD counts of a the two prominent peaks (975.3 nm and 977.7 nm) excited with a 780 CW laser comparing collection from taper (solid) and base (open) collection. (c) Power dependent measurement of the integrated intensities of X emission from a nanowire on a straight SiN waveguide pumped with a 670 nm pulsed diode laser at 40 MHz. The collection with a Si CCD spectrometer and APD is compared.

are two main peaks in this quantum dot at 977.7 nm and 975.3 nm. The broad emissions at wavelengths less than 975.3 nm only appear at higher power where the quantum dot is over-saturated giving rise to additional, albeit weaker, complex emissions.

To see how bright the quantum dot can be, a CW 780 nm laser is used to excite the quantum dot-nanowire device. The summary of the count rates measured from the two peaks at both the taper and base are shown in Table 5.3. There is a consistent $\sim 20\times$ brighter collection from the taper than the base that appears to be independent of complex. This factor is similar to the ones observed previously. We note that the observed shift in pump-power indicates that, similar to coupling from the nanowire to the waveguide, coupling from the waveguide to the nanowire is also more efficient from the taper. In other words, evanescent pumping, like evanescent coupling, is more efficient than coupling by scattering. Based on the slope from the log-log plot (Figure 5.6(b)) of the emissions, it appears that the peak at 975.3 nm is a biexciton ($n = 2.02 \pm 0.03$) and 977.7 nm may be either a neutral or charged exciton ($n = 1.01 \pm 0.01$). In the previous chapter, we mentioned that for a three peak quantum dot system, the neutral exciton photon usually has a shorter wavelength than the charged exciton photon (see Figure 4.10(a)). However, since this particular quantum dot being studied is not a three-peak system, the same observations do not apply. The biggest hint to this being a neutral exciton is the presence of the biexciton at higher powers. Due to the biexciton-exciton cascade, there should always be a neutral exciton whenever a biexciton is present [26]. Further discussion will be made on why the peak at 977.7 nm is most likely a neutral exciton. Since the brightest peak (977.7 nm) yielded over 1 Mcps when pumped with the CW laser when collected from the taper, we focus the rest of the section on analysing this peak.

To calculate the coupling efficiency of the system, the quantum dot was excited with a 670 nm, pulsed diode laser with a 40 MHz repetition rate. In the previous chapter, we calculated a difference of approximately 20% in the coupling efficiency between using the integrated Lorentian fit of a spectrum (1200 g/mm grating with a CCD detector) versus

Wavelength (nm)	taper (kcps)	base (kcps)	ratio (taper/base)
975.3	483	23.5	20.5
977.7	1414	68.1	20.8

Table 5.3: Collection of quantum dot emission from a nanowire from a straight SiN waveguide pumped with a 780 nm CW laser

the raw counts detected using the tunable filter and APD detector setup. Here, we also compare the integrated counts to the detected APD count rate for the 977.7 nm emission as shown in Figure 5.6(c). The results from this nanowire are consistent with the free-space results with the integrated counts (249 kcps) being 81% of the APD counts (306 kcps).

Source of loss	Transmission (%)	Loss (-dBm)
detector efficiency	18	7.45
propagation loss	97.3	0.12
loss at facet	60.95	2.15
loss through fibre + feed through	36.3	4.4
tunable filter (950 nm)	55.7	2.54
throughput	12.0	9.21
Optical system efficiency	2.2	16.7
emission direction	50	3.01
$\beta_{\mathrm{HE}_{11}}$	95	0.223
filtered phonons	80	0.97
Factor for calculating η_{coll}	0.82	20.9

Table 5.4: Losses through the system when measuring a nanowire on a straight waveguide of length $L/2$ =0.25 cm. (For an operating wavelength of 977 nm)

As before, we calculate the transmission of the system using measurements of each source of loss (listed in Table 5.4). We obtain a throughput of $\eta_t = 12.0\%$. If we include a detector efficiency of $\eta_d = 18\%$ at 977 nm, we obtain an optical system efficiency of $\eta_t\eta_d = 2.2\%$. We again use the counts at saturation for the 977.7 nm emission line (306 kcps, 40 MHz rep. rate laser) to calculate a source efficiency of 35%.

If we take into account the additional sources of loss (Table 5.4(bottom half)), we arrive at a factor of 0.82% which is required to calculate the collection efficiency. From this, we calculate a collection efficiency of $\eta_{\mathrm{coll}} = 93\%$. We reiterate that this value corresponds to the percentage of photons directed towards the tapered end of the nanowire that couple to the SiN waveguide. This efficiency approaches predicted values based on COMSOL simulations discussed in Section 2.4.1. This efficiency is much higher than that of the previous sample on the curved waveguide possibly because this quantum dot emits only from a single charge state as opposed to emitting from both the X and X^- complexes.

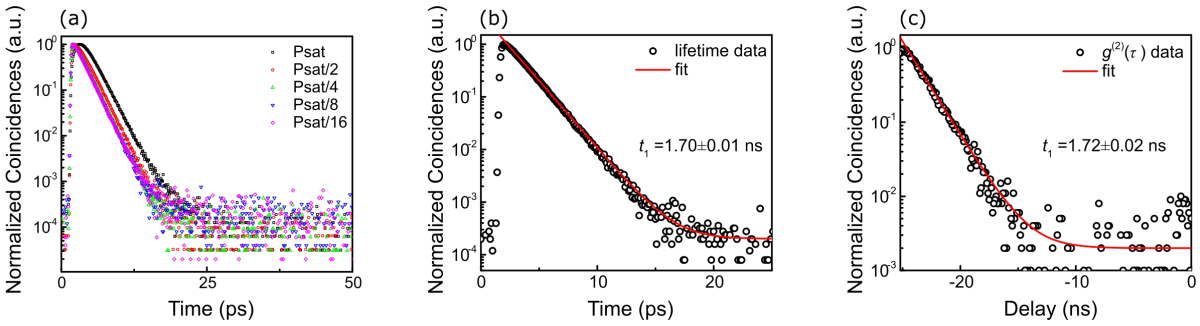

Figure 5.7: (a) Power-dependent lifetime of X emission pumped at 20 MHz. (b) Lifetime measurement at low power $P_{\text{sat}}/16$. (c) Zoom in on one side of a $g^{(2)}(\tau)$ measurement at $P_{\text{sat}}/16$ and extracting the lifetime through a fit.

5.3.2 Time-resolved photoluminescence - Lifetime

Time-resolved PL measurements are used to determine the lifetime of an excitonic complex. In this particular case, we continue to investigate what we believe to be a neutral exciton. For many of the neutral excitons we have studied, there is no observed second decay component even at very low pump powers. However, though many of the charged excitons studied have shown a second decay component in the lifetime, this is not always the case. Thus it is not possible to conclude the type of complex based purely on the lifetime of the emitter.

Figure 5.7(a) shows a semi-log power-dependent lifetime measurement of the emitter pumped between P_{sat} to $P_{\text{sat}}/16$. Throughout the different pump-powers, there is no obvious second decay component. With increasing pump power, the onset of recombination shifts to longer times since ground state emission is necessarily delayed due to the population of higher excited states which need to empty before observation of the ground state emission. This accounts for the shift seen right after $t = 0$ although the lifetime of the exciton remains the same.

The behaviour exhibited by the emitter is consistent with that of lifetime measurements collected in free-space, yielding a lifetime $T_1 \sim 1.7\,\text{ns}$. Since the calculated lifetime is close to the bulk lifetime of InP, as before, we can conclude that this set of nanowires are grown with a good normalized diameter $D/\lambda = 0.24$ and that coupling into the additional ridge waveguide does not have a detrimental effect on the lifetime of the emission. In other words, the rate at which the photons are generated within the quantum dot has not been impacted.

5.3.3 Spectral purity

We again use a temperature-controlled etalon to measure the linewidth of the 977.7 nm emission. The quantum dot was pumped above-band with a CW 780 nm laser. First, the 977.7 nm peak was passed through a tunable filter. The temperature-controlled etalon in combination with an APD detector was used to scan through the filtered emission and

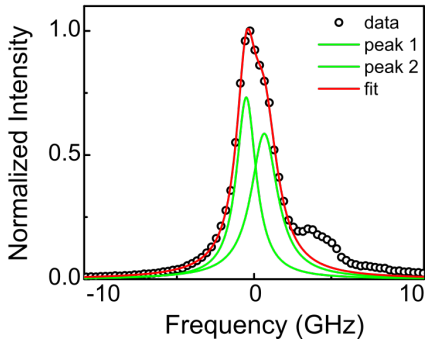

Figure 5.8: **High-resolution PL spectrum of a single neutral exciton in an InAsP quantum dot.** Two Lorentzian peak fits used to measure convolved linewidths of 1.54 GHz and 2.1 GHz, respectively.

measure the count rate to reconstruct the emission peak with a much higher resolution. There is a birefringence associated with this particular etalon which we deal with by using a polarizer at the output of the etalon. Without the polarizer, two distinct peaks can be seen that may mislead one to believe that it is the fine-structure splitting of the neutral exciton. The polarizer was adjusted to minimize one of the two peaks.

Figure 5.8 shows a PL measurement where the emission is evidently asymmetric. We fit the emission using double Lorentzian peaks showing what may be evidence of fine-structure splitting found only in the neutral and biexciton emissions. This splitting observed is very narrow ($\sim$ 1.1 GHz). The second bump in the linewidth (on the right) is a residual peak from the birefringent polarization of the etalon itself despite efforts to minimize its effects. Linewidths of 1.54 GHz and 2.10 GHz were measured from the fit of the two peaks. After deconvolving the peaks with a 1.3 GHz IRF, the deconvolved linewidths are 0.2 GHz and 0.9 GHz. This is in agreement with the range of potential linewidth measured from the hundred free-standing nanowires.

Plastic deformation causing structural defects in the nanowire can potentially affect the spectral purity of the quantum dot emission. The extraction of the nanowire from the growth substrate is typically a quick and easy process. However, during the placement phase of the operation, the nanowire may be damaged by the probes as one probe is used to pin down the nanowire on the waveguide, and the other is used to adjust the angle of the nanowire so that it sits parallel atop the waveguide. Surprisingly, the spectral purity of this particular nanowire does not appear to be affected by the transfer process. More experiments need to be conducted to verify if this remains consistent across all other nanowires placed on the SiN waveguides through our "pick and place" technique. Additionally, the coupling into the waveguide itself has not been shown to have a strong effect on the spectral purity of the emission either.

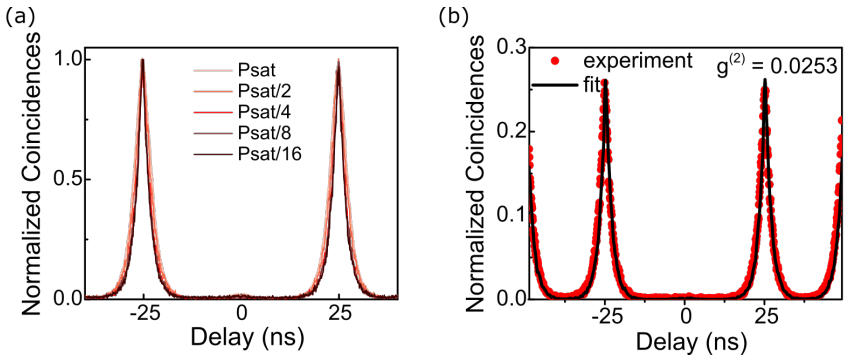

Figure 5.9: (a) Power-dependent autocorrelation measurement of the 977 nm emission line with a 670 nm pulsed diode laser at 40 MHz. (b) Autocorrelation measurement at saturation with a model fit with $g^{(2)} = 0.0253$.

5.3.4 Single-photon purity

So far, we have observed that the efficiency of the device, the spectral purity, and the lifetime of the emitter is not greatly impacted by the transfer process and coupling to the SiN waveguide. The main interest is still whether the nanowire devices are still good sources of single photons. Since we are primarily interested in the single-photon purity, we only took pulsed autocorrelation measurements of the 977 nm emission peak.

A power-dependent autocorrelation measurement is shown for the 977.7 nm emission peak in Figure 5.9(a). Using the stochastic model fit described in the previous chapter, we measure a $g^{(2)}(\tau = 0) = 0.0253$ or a single-photon purity of 97% for the quantum dot pumped at P_{sat} as shown in Figure 5.9(b).

This is in line with the average measured $g^{(2)}(\tau = 0) = 0.04 \pm 0.03\%$ at P_{sat} across the fourteen free-standing nanowires. We can conclude that the single-photon purity is not impacted much after manipulation and placement on the SiN ridge waveguide.

5.3.5 Indistinguishability

In this thesis, the indistinguishability of two photons is concerned with quantum states of sequentially emitted single-photons. If there is a perfect overlap of the states in all degrees of freedom, then the two photons are considered to be perfectly indistinguishable. Two-photon interference (TPI) (i.e. HOM) measurements are conducted to measure the indistinguishability of the emitted photons from the quantum dot. A $\lambda/2$ half-wave plate (HWP) is used to change the polarization of one of the photons hence making it either distinguishable or indistinguishable.

For our experiment, we conducted measurements using both a 670 nm, pulsed diode laser with a 40 MHz repetition rate and a 780 nm, CW laser. Figures 5.10(a) and 5.10(c) show the two-photon interference results pumped at saturation P_{sat} with either a pulsed or CW laser, respectively. A power-dependent HOM two-photon interference measurement was not taken simply because the count rate was too low despite having the strongest

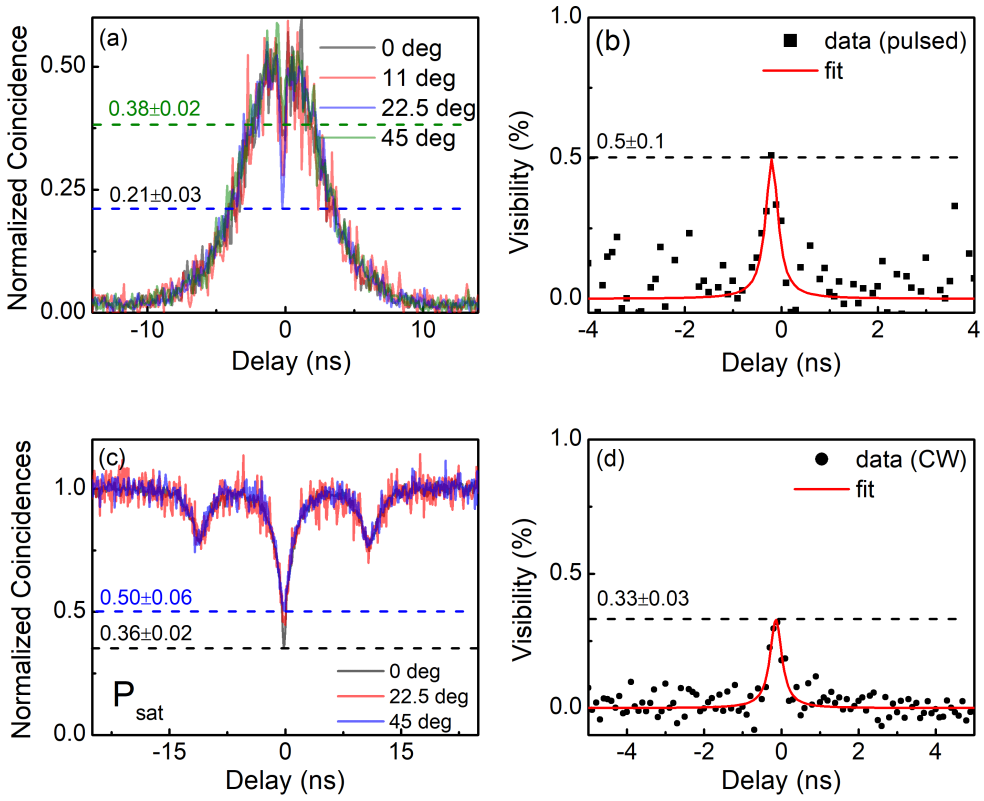

Figure 5.10: **Hong-Ou-Mandel measurement** of a nanowire on a straight SiN waveguide (a) pumped with a 670 nm pulsed diode laser at 40 MHz along with its (b) visibility. (c) HOM measurement pumped with a 780 nm CW laser with an 11 ns delay line. (d) The visibility of the quantum dot from the CW measurement.

intensity in the PL among all the other quantum dots in the set. To ensure the polarization of subsequently emitted photons are the same, a polarizer is placed at the input of the Mach-Zehnder interferometer. A HWP is placed in one of the Mach-Zehnder arms to control the degree of distinguishability (see Figure 3.10). The results for both are shown in Table 5.5.

HWP Angle (°)	Pulsed	CW
0	0.35	0.36
11	0.28	-
22.5	0.21	0.45
45	0.38	0.50

Table 5.5: Zero-delay HOM dip of an exciton excited with either a pulsed or CW laser

We first discuss the pulsed HOM measurement. A ~ 25 ns delay line was added to match the delay between pulses of the 40 MHz pulsed diode laser. As such, unlike a regular HBT $g^{(2)}(\tau)$ measurement where $g^{(2)}(0)$ is nearly zero, for a HOM measurement, we have a pulse

that is half the height of the other pulses at $g^{(2)}(0)$. To calculate the TPI visibility, we use Eq. (3.4), which we rewrite here

$$V(\tau) = \frac{g_{\perp}^{(2)}(\tau) - g_{\parallel}^{(2)}(\tau)}{g_{\perp}^{(2)}(\tau)}. \tag{5.4}$$

In this particular case for the emission in Figure 5.10(a), 0 and 45 degrees appear to have very close zero-delay values. However, 22.5 degrees shows the largest dip, hence we use this value for $g_{\parallel}^{(2)}(\tau)$. Ideally, if we had a measurement at 67.5 degrees, we would have had $g_{\perp}^{(2)}(\tau)$. We did not obtain a measurement at this polarization angle, so we used the closest one we had which is at 45 degrees. By applying Eq. (3.4) using the integrated coincidence counts in the central ($\tau = 0$) peak for angles 22.5 degrees and 45 degrees, we obtain a non-post-selected TPI visibility of 3.0% which is not impressive. Even if we estimate the coincidence counts that would have been obtained had we had the 67.5 degree measurement, it would still only be 4.1%. We can also look at the post-selected TPI visibility by applying Eq. (3.4) to each time bin of the histograms in Figure 5.10(a). This is plotted in Figure 5.10(b) from which a TPI visibility of 50% is obtained at $\tau = 0$ for the case of 22.5 and 45 degrees.

We also conducted a CW measurement of the same emission line with a similar setup but with an 11 ns delay. Since the count rate using the pulsed diode laser were so low, we opted for a CW laser to maximize the count rate. Again, the experiments were conducted at P_{sat}. Unlike a regular $g^{(2)}(0)$ conducted with a HBT setup, there are additional side dips corresponding to the delay (δ) between the two Mach-Zehnder arms. The reason for this is similar to why there is a dip at $g^2(0)$ in an HBT measurement except the delay forces a shift $g^2(\tau = \pm\delta)$. Table 5.6 shows the possible paths two sequentially emitted photons that can take. These paths are schematically shown in Figure 5.11.

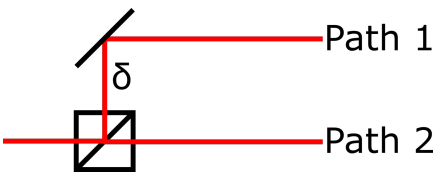

Figure 5.11: Schematic of possible paths taken by single photons incident on a beam-splitter.

Start	Stop
Path 1	Path 2
Path 2	Path 1
Path 1	Path 1
Path 2	Path 2

Table 5.6: Possible paths taken by two photons in a $g^{(2)}(\tau)$ measurement.

Let's say the first path (Path 1) has a delay of δ while the second path (Path 2) does not. Recall a count is only registered when a photon reaches the start and another reaches the stop detector. A count cannot be registered at the special times δ unless there were two photons entering the two arms at the same time, which is not possible for a single photon source. This eliminates either of the last two options. Hence, at $t = \delta$, there are only three possible outcomes. This results in a dip of 0.75 intensity as seen the two side dips of Figure 5.10(c).

Conversely, at $t = 0$, the two photons will only arrive at the same time if it takes the latter two paths. This reduces the possible outcomes to two out of four which gives us a dip of 0.5. If we also take into account the effects of indistinguishability, when the photons interfere again at the beam splitter, if the two photons are distinguishable, then they can take any of the outcomes from Figure 3.9, and the dip remains at 0.5. However, if two interfering photons are indistinguishable, then the only option is for them to leave the beam splitter from the same port. As such, no counts are registered at $t = 0$, and the dip goes down to zero.

For this particular CW HOM shown in Figure 5.10(c), we see a dip at $g_{\perp}^{(2)}(0) = 0.5$ which is consistent for the distinguishable case. Since the dips at the delay $\tau = \delta$ and $\tau = 0$ have $g^{(2)}(\tau = \delta) \sim 0.75$ and $g_{\perp}^{(2)}(\tau = 0) \sim 0.5$, we know the single-photon purity of the emission has not been compromised. Using the $g_{\perp}^{(2)}(\tau)$ and $g_{\parallel}^{(2)}(\tau)$, the visibility is calculated using Eq. (3.4) and shown in Figure 5.10(d). The resulting experimental visibility of $V(0) = 0.33 \pm 0.03$ was calculated from the fit of the data. Since this was a CW experiment, this represents a post-selected TPI visibility at $\tau = 0$ which can be compared with Figure 5.10(b).

Improvements

The results presented thus far are only preliminary. We encountered problems with the stability of the system while taking measurements because non polarization-maintaining (PM) fibres were used for the setup. In future experiments, it would be beneficial to have the entire setup use PM fibres. This way, it would be easier to control the polarization of photon at the point where they interfere.

We note that the low TPI visibilities obtained are most likely due to the use of above-band excitation and of rather long delay lines. By shortening the delay lines, Kalliakos et al. [62] found that the TPI visibility increased exponentially between the Mach-Zehnder arms. The exponent extracted from the curve of the visibility versus the time delay gives the coherence time of the emitter. We can therefore assume the low TPI visibility obtained here is due to a short coherence time.

Two ways to improve the indistinguishability in the HOM measurement are to pump either resonantly or quasi-resonantly as this diminishes the influence of charges from the environment. This limits the relaxation steps for exciton formation and reduces the excitation jitter which in turn improves the photon coherence [53, 90]. To acquire a high photon coherence, pumping resonantly is the best option.

5.4 Stability of the InP nanowire-SiN waveguide system

After placing the nanowires on the waveguides, the nanowires remained firmly stuck onto the waveguide. After a session of transferring nanowires to the waveguide, the entire

nanomanipulator setup was taken out the SEM. Subsequent revisits of the site of the nanowire on waveguide show that the nanowire has not moved from where it was placed. Even the angle at which it sits on the waveguide is unchanged.

Not all the nanowires were placed perfectly parallel to the waveguide as some had a slight angle to them with respect to the waveguide. Although it may have affected the efficiency of the coupling of the nanowire to the waveguide, it was beneficial for determining if the nanowire may have moved while being placed into the cryostat system. In fact, we were able to observe the nanowire-waveguide alignment by imaging the scattering of laser light on a CMOS camera. From these optical images of the nanowire, we were able to compare the angle of the nanowire with that of SEM images. After optical characterization in a cryostat, we looked at the site of the nanowires on-chip again under the SEM and found that they remained unchanged.

This a promising evidence that the nanowire-chip system is quite stable and robust. This leaves only the occasional realignment of the lensed fibre to the edge of the chip as the remaining source of instability to the system. To improve on the stable coupling through the lensed fibre at the facet of the chip, glue can be applied at the fibre-to-chip edge interface. With a more stable setup, we can manufacture on-demand, high-purity, single-photon devices that are "plug and play".

5.5 Summary

In summary, we demonstrate a process to efficiently couple single-photons from an InAsP quantum dot in an InP photonic nanowire waveguide to a ridge SiN waveguide on chip. Through various experiments, we show that the optical properties of the nanowire device have not changed even after manipulation and placement on a SiN waveguide. The emission range and complexes from PL spectra, the spectral purity, the lifetime of the emitter, and the single-photon purity of the quantum dot remain consistent with the results from free-standing nanowires on their original growth substrate. Amazingly, we were able to achieve a coupling efficiency of 93% with a $g^{(2)}(\tau = 0) = 0.0253$ from one of the hybrid devices. This is very promising for the larger integration of these nanowires as single-photon sources on-chip. We can imagine a future where multiple nanowires can be placed on-chip allowing for a large packing density of single-photon sources on a single chip.

Chapter 6

Conclusion and Future Outlook

In the past two years as a student at the National Research Council of Canada, I developed the technique to transfer InAsP quantum dot-InP nanowire devices from their growth substrates to chips containing SiN waveguides using a "pick and place" method. I was involved in the testing of the optical properties of these quantum dot-nanowires devices both for sets on substrate and sets transferred on-chip. Preliminary tests of the nanowires transferred to different waveguide structures will be used to improve the design of the SiN waveguide structures for future devices.

In this chapter, we conclude with a summary of our achieved results and provide an outlook into other types of waveguide structures needed to access different properties of the quantum dot emitters. Next, the results from a preliminary study with ring resonators in the lab are presented. Lastly, we explore ways to scale up the manufacturing of these hybrid nanowire-SiN waveguide devices.

6.1 Conclusion

We have demonstrated in the previous chapters the optical properties of the quantum dots (brightness, coherence, single-photon purity, and indistinguishability) embedded in nanowire devices. To test each of these properties, we took photoluminescence spectra to determine the emission wavelengths of the quantum dot-nanowire devices, used power-dependent PL of single emission lines to distinguish between excitonic complexes, calculated the efficiency of the emitter using the maximum count rate when pulsed with a laser above-band, measured the time-resolved PL spectra to determine the lifetime of the emitter, used an etalon to obtain high-resolution PL spectra of emission peaks and to determine their spectral purity, and measured the single-photon purity of the emitter using autocorrelation measurements. Indistinguishability measurements were only taken for a single nanowire on a SiN waveguide but not for any on the growth substrate.

For nanowires on the growth substrate, we tested quantum dots designed to emit between $940 \sim 980\,\text{nm}$. From a subset of those quantum dots, we only considered those with a single dominant emission line at lower excitation powers. We measured an average

maximum count rate of 119 ± 45 kcps when pumped above-band with a laser pulsed at repetition rate of 80 MHz. From this result, we calculate a mean source efficiency of 33%. For the neutral exciton, we measured lifetimes of ~ 1.7 ns which is close to the bulk InP lifetime (~ 2.5 ns). This means that the nanowires were grown with the right normalized diameter to maximize the efficient coupling of the quantum dot emission into the HE_{11} fundamental mode of the nanowire waveguide. The measured lifetime was used to calculate a lifetime-limited linewidth of 0.09 GHz. We measured an average deconvolved linewidth of 0.9 ± 0.4 GHz. This shows that, even after deconvolving the measured linewidth, we have linewidths that are on average ten times that of the lifetime-limited linewidth. Lastly, we measured an average $g^{(2)}(0) = 0.04 \pm 0.03$ which translates to a single-photon purity of $96 \pm 3\%$.

On a different set of nanowires, we characterized the emission complexes from a separate set of nanowires showing three dominant peaks near pump saturation power. We found the best way to identify the complexes is to use a combination of autocorrelation and cross-correlation measurements between complexes within the same quantum dot because each complex has a characteristic behaviour as a function of pump power [68].

With this in mind, we wanted to verify how the properties of the quantum dot may be affected after transfer onto a SiN waveguide. This set of nanowires were also designed to emit within the same range ($940 \sim 980$ nm). On average, much higher count rates were achieved by collecting directly from the facets of the chip as opposed to the free-space setup. Minor differences in the transfer process between nanowires may have accounted for the large discrepancy in taper to base collection ratios. Detailed analysis of a nanowire-SiN waveguide device was conducted on the one showing a particularly high count rate of over 1 Mcps when pumped above-band with a CW laser. Its most prominent emission, which we believe to be from an X photon, yielded a lifetime of 1.7 ns. The TPI visibility of the emission was measured to be $\sim$30%.

From our initial findings, we conclude that the transfer process of a nanowire to a photonic integrated circuit does not significantly impact the optical properties of the quantum dot-nanowire device.

6.2 Future Outlook - Move towards more advanced quantum integrated circuits

Since we have found our transfer process to be a promising method of creating hybrid integrated devices, further studies will look into accessing the quantum dot's optical properties with more complicated photonic structures. The many components used in our lab to take PL spectra, HBT, and HOM can all fit on a single chip. Rather than fibres, waveguides can be used to direct light through various components like beam splitters, filters, and detectors all on the same chip. This "lab on a chip" would inherently be more stable than the all-fibre setup and be more robust against the environment.

A broadband waveguide is beneficial for accessing the other complexes in a quantum dot emission. By integrating the broadband nanowire waveguide on a SiN ring resonator

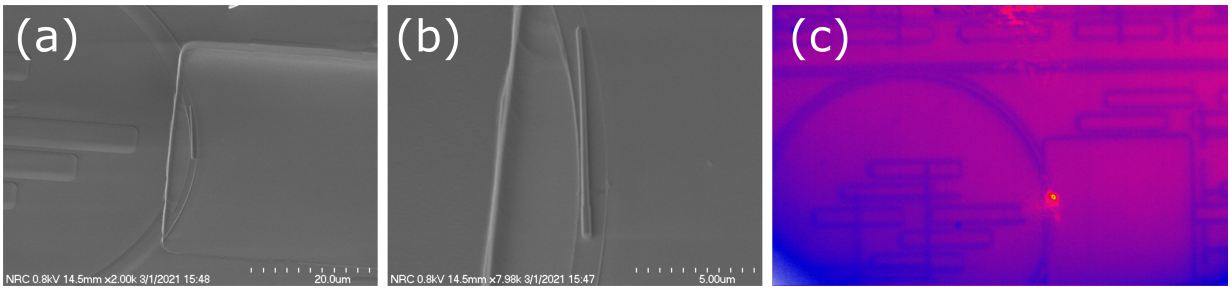

Figure 6.1: **Ring Resonator.** (a) SEM image of a nanowire on a ring resonator within the opening of the oxide layer. (b) SEM of the same nanowire at higher magnification. (c) Optical image of the ring resonator showing scattered light at the site of the nanowire and into the direction of the taper.

waveguide, it is again possible to achieve Purcell enhancement within the resonator cavity [36]. Gates can be used to fine-tune the wavelengths to be enhanced and filtered by the ring resonator. The Purcell enhancement on the lifetime allows for faster emission rates by lowering the lifetime to a few hundred picoseconds or lower.

Ring resonators waveguide structures have a wide range of uses for integrated optics. Not only can they be used for Purcell enhancement but they can also be used for frequency translation and as add-drop filters.

6.2.1 Introduction to ring resonators

A simple ring resonator consists of a looped optical path and an optical access for coupling light in and out of the ring resonator. If the phase shift through the loop is an integer multiple of 2π, resonant conditions are met, and the input field constructively interferes with the resonant cavity of the ring. As the resonant light completes trips around the ring, the intensity builds up. Since only select wavelengths can couple resonantly with the ring, ring resonators can also function as filters. The wavelength spacing between two axial modes of the ring resonator is defined as the free spectral range (FSR) with

$$FSR = \frac{\lambda^2}{n_g L}, \tag{6.1}$$

where λ is the wavelength, $L = 2\pi R$ is the length of the ring with a radius $R = 50\,\mu$m, and n_g is the group index of the ring material. For this particular ring resonator made of Si_3N_4, $n_g = 2.12$ at 935 nm. With this, we calculate an FSR of 1.31 nm, which is consistent with the measured FSR of 1.3 nm from Figure 6.2(c).

Usage as filters

A Purcell enhancement effect was not observed from the measured lifetime of the emission from a quantum dot-nanowire device on a ring resonator waveguide. However, a filtering effect was observed in the PL spectra of the emission as shown in Figure 6.2(b). Recall

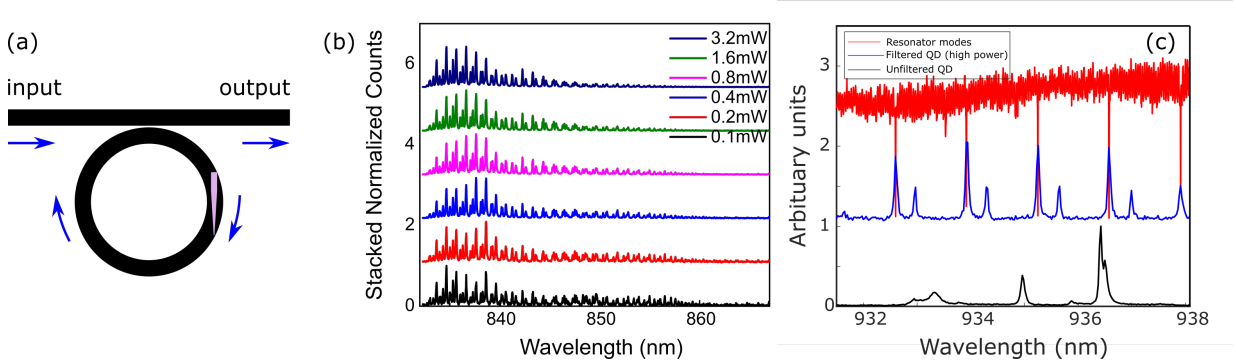

Figure 6.2: **Ring Resonator.** (a) Schematic of a single-port ring resonator. A nanowire is shown in purple on the right side of the ring. (b) Power-dependent PL of wurtzite InP emission from a nanowire. (c) Plot of the ring resonator transmission modes of a SiN waveguide (red), the quantum dot emission filtered through the ring resonator (blue), and the unfiltered quantum dot emission (black).

in Figure 2.7(b) what typical bulk InP emission looks like at higher pump powers. Using the "pick and place" method, the nanowires were placed on the ring resonators. SEM and optical images of a nanowire on a ring resonator are shown in Figure 6.1. We also show a schematic of a ring resonator in Figure 6.2(a).

Four different nanowires were placed on four separate ring resonator waveguide structures. We were only able to find the quantum dot emission from two of the four nanowires. For each nanowire, we observed a comb effect across the bulk InP emission (832-875 nm). Since the nanowire on the ring resonator is pumped above band at much higher power than that shown in Figure 2.7(b), the spectra show a much wider spread of emissions. To better understand this comb effect, we used a tunable laser to measure the transmission through a ring resonator without a nanowire (see Figure 6.2(c)(red)). We found the period of the transmission dips (red) and nanowire emission peaks (blue) align for short wavelength ranges ($\sim$ 10 nm). We measured an FSR of 1.3 nm for both the filtered quantum dot emission and ring resonator modes. Next, we looked at the unfiltered dot emission pumped at much lower powers (black).

Knowing that the quantum dot emission will shift at different temperatures, we took power-dependent PL measurement of the filtered emission at 1 K intervals. At low pump power (0.175 mW), we see in Figures 6.3(a) and (d) that the main emission line does not appear until 7 K. Once the emission line completely passes through that particular tooth of the comb, it is not seen again until a much higher temperature of around 45 K when it has shifted enough to start overlapping with the next mode. Figures 6.3(b) and (e) show a similar filtering pattern is pumped at saturation (1 mW), resulting in higher intensity values. This time, at higher temperatures, evidence of other peaks appear. As the quantum dot was pumped at even higher powers (20 mW), the entire quantum dot becomes flooded (Figures 6.3(c) and (f)). The modes of the ring resonator are clearly seen, and an FSR of 1.3 nm is measured.

Since collection of quantum dot emission from the facets of the waveguide only showed

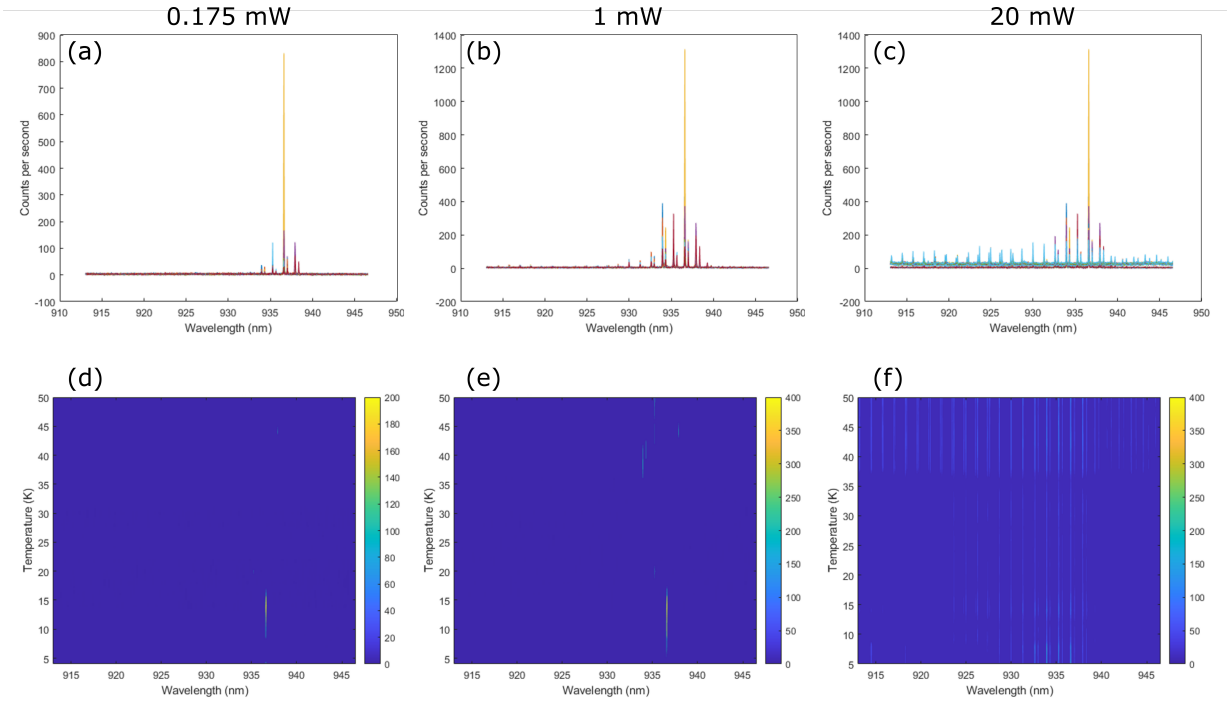

Figure 6.3: **Filter effect as a function of power and temperature.** (a)-(c) PL intensity of filtered emission taken at four different increasing pump powers. (d)-(f) 2D-plot of PL intensities as temperature is increased. Pump powers correspond with those shown directly above in (a)-(c).

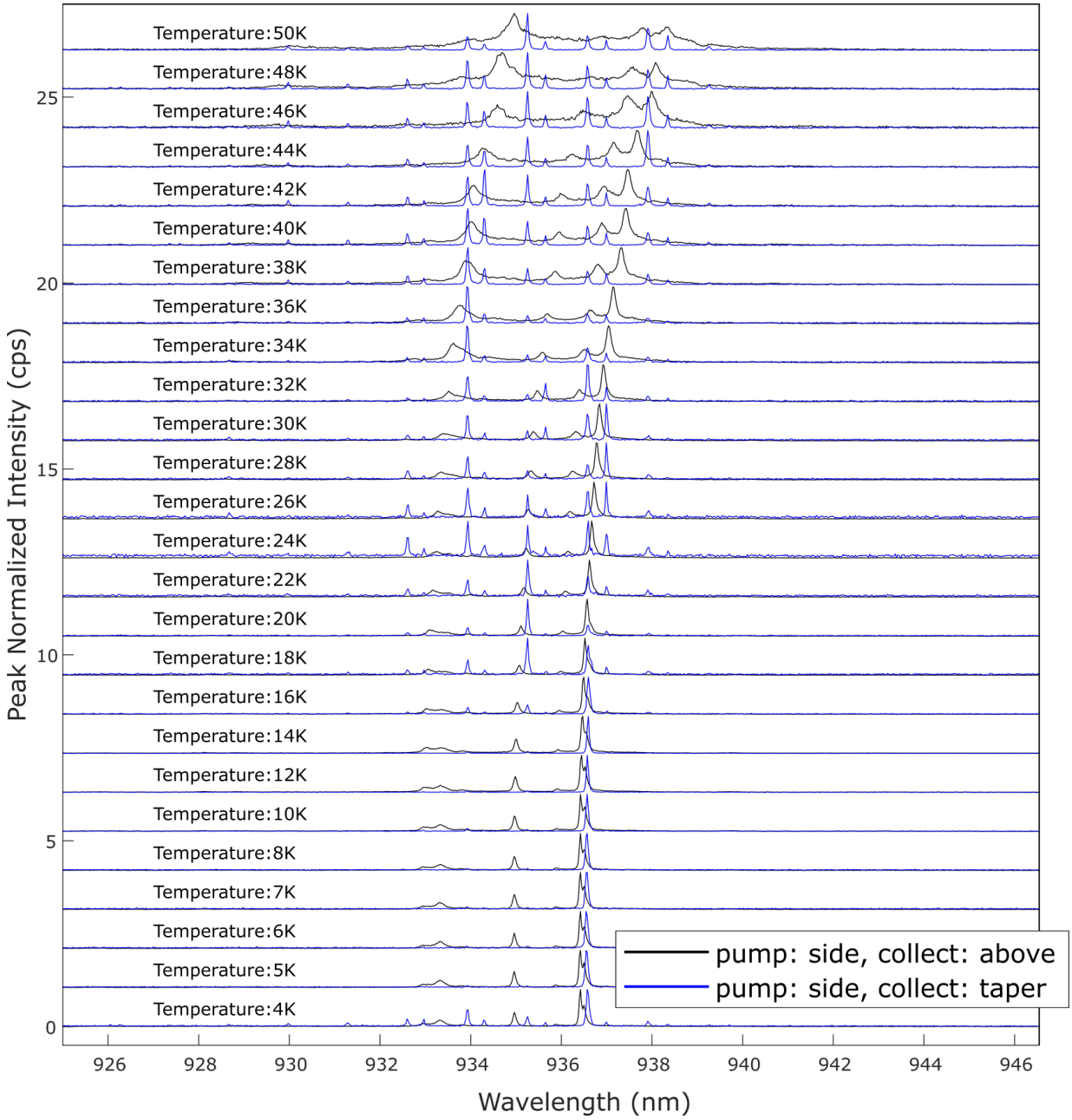

Figure 6.4: **Dot emission as a function of temperature.** Collection from above (black) gives the spectrum of the unfiltered dot. Collection from the side (blue) results in dot emissions only seen when overlapping with the modes of the ring resonator thus acting as a comb/filter.

the resulting filtered emission, we needed to collect the quantum dot emission from above to see the unfiltered emission spectrum. Using the same setup for testing nanowires with free-space optics, we excited the quantum dot by sending laser light through the waveguide and collecting the sideways emission of the quantum dot from above the chip using a microscope objective. The resulting normalized unfiltered emission is shown in black in Figure 6.4. We were also able collect the filtered emission through the waveguide at the same time (shown in blue). As we increased the temperature, the emission from the quantum dot broaden and shift towards longer wavelengths. The intensity of the filtered emission at specific wavelengths would wax and wane as the peaks of the quantum dot emission overlapped the ring resonator modes.

6.2.2 Emission energy tuning

For a wider array of applications, a single-photon source should also be frequency tunable and have the potential to be electrically driven. A simple way to shift the frequency of the quantum dot emission is to simply change the temperature of the system hosting the nanowire. The shift in the emission as temperature is increased is clearly seen in Figure 6.4 (black), but this is clearly not ideal because of the apparent broadening effect at higher temperatures. A second method is to use the frequency translation of the quantum dot emission through a ring resonator. A third method is to use voltage controlled gates.

There have been many studies utilizing electric fields to tune the emission energy of quantum dots [7]. Electric fields applied through gates have been employed to tune the exciton emission energies of quantum dots in nanowires [93]. The task of placing gates on nanowires standing orthogonal on a substrate is difficult due to the high aspect ratio. Recall that the quantum dot is located $\sim 1\,\mu$m above the base of the nanowire, making it difficult to put gates on such a structure. However, this is much easier to realize when the nanowire is laid flat on a substrate. Gates could then be easily added around the nanowire. The gates tune the centre emission wavelength through the Stark effect in which the introduction of an external electric field causes a shift in the degenerate energy levels [58]. Figure 6.5 shows five gates (lighter grey) made of gold with a titanium sticking layer underneath lying perpendicular to a ridge waveguide. This waveguide is similar to the ones in Chapter **5** of the thesis.

Previously, we did not care for placing nanowires in very specific locations on the SiN waveguide, but it did not affect the results as long as the nanowire was placed along a SiN waveguide within the opening of the oxide layer of the chip. With the additional gates, during placement, the nanowire can be nudged gently with a probe tip to desired positions so that the quantum dot is located within the vicinity of a gate. The exact location of the quantum dot may be unknown, but we do know that it is grown $\sim 1\,\mu$m from the base. As such, we expect the "pick and place" method employed previously will be just as straightforward.

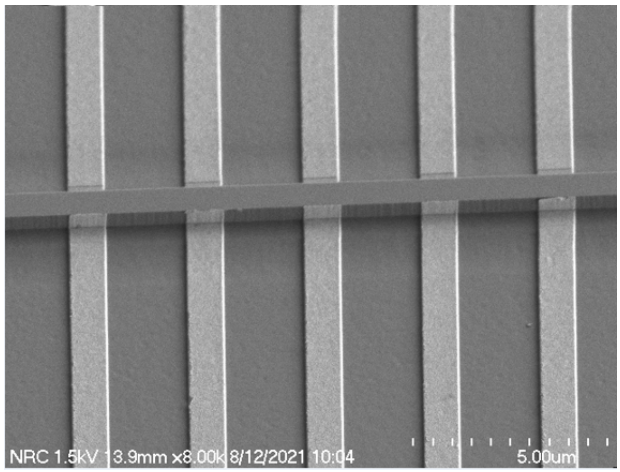

Figure 6.5: SEM of Au gates (light grey) along the side of a SiN ridge waveguide (horizontal grey bar).

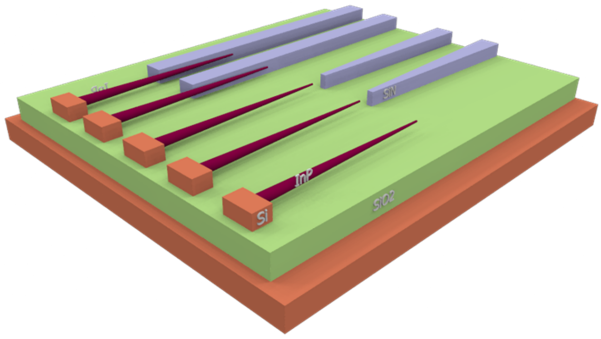

Figure 6.6: **Horizontally grown nanowires** directly onto substrate containing waveguides. Drawn by Dr. Dan Dalacu.

6.2.3 Direct growth of nanowires to SiN waveguide structures

To improve the scalability of this hybrid integrated circuit, we want to be able to grow nanowires directly on the chip itself. Figure 6.6 shows one such proposed chip design. The first major design change to note is that these nanowires are designed to grow horizontally rather than orthogonally to the surface of the chip. The second design change of note is that the nanowires are grown on Si platforms rather than on a InP substrate. Much research has already been conducted in the growing of InP nanowires on silicon substrates [25]. However, the direction of growth has been difficult to control in these trials. It has also been shown with Si nanowires, that it is possible to grow them at a 90 degree angle on a silicon ledge [94, 57]. More research needs to be conducted on how to grow InP nanowires horizontally on a Si ledge.

From Figure 6.6, we number the nanowires from 1 to 5 with 1 being the closest and 5 being the farthest. Nanowire 1 shows a single nanowire grown horizontally from a silicon base. If this first type of nanowire is successful, we can consider coupling the nanowire directly with waveguide structures. Nanowires 2 and 3 are grown so that the mode of the

nanowire can be butt-coupled into the tapered SiN waveguide (purple) much like how we couple lensed fibres at the waveguides facets. Lastly, nanowires 4 and 5 couple into the waveguide using the evanescent tail of the nanowire emission. This last one utilizes the same mechanism as the nanowires placed along waveguides used in this thesis.

If all three structures are achievable, we can imagine a future where we can grow multiple single-photon sources (nanowire devices) directly on a single chip. These chips would have a small footprint, be densely packed with single-photon sources, and be stable; all of which are requirements ideal for quantum computers. It has been shown that these nanowires are capable of producing entangled pairs [106] which are useful for applications such as quantum repeaters. This stable, bright, entangled, multiplexed design would be beneficial for additional applications such as quantum repeaters for a future quantum internet. s

References

[1] Marco Abbarchi, Takaaki Mano, Takashi Kuroda, and Kazuaki Sakoda. Exciton dynamics in droplet epitaxial quantum dots grown on (311)A-Oriented Substrates. *Nanomaterials (Basel, Switzerland)*, 10(9):1833–, 2020.

[2] A. P Alivisatos, M. C Schlamp, and V. L Colvin. Light-emitting diodes made from cadmium selenide nanocrystals and a semiconducting polymer. *Nature*, 370(6488):354–357, 1994.

[3] Susan J Angus, Andrew J Ferguson, Andrew S Dzurak, and Robert G Clark. Gate-defined quantum dots in intrinsic silicon. *Nano letters*, 7(7):2051–2055, 2007.

[4] Roman Anufriev. Optical properties of InAs/InP nanowire heterostructures, 2013.

[5] M. Arcari, I. Söllner, A. Javadi, S. Lindskov Hansen, S. Mahmoodian, J. Liu, H. Thyrrestrup, E. H. Lee, J. D. Song, S. Stobbe, and P. Lodahl. Near-unity coupling efficiency of a quantum emitter to a photonic crystal waveguide. *Phys. Rev. Lett.*, 113:093603, 2014.

[6] A. Badolato, K. Hennessy, M. Atatüre, J. Dreiser, E. Hu, P. M. Petroff, and A. Imamoglŭ. Deterministic coupling of single quantum dots to single nanocavity modes. *Science*, 308:1158–1161, 2005.

[7] M. Baier, F. Findeis, A. Zrenner, M. Bichler, and G. Abstreiter. Optical spectroscopy of charged excitons in single quantum dot photodiodes. *Phys. Rev. B*, 64:195326–1, 2001.

[8] W. L. Barnes, G. Björk, J. M. Gérard, P. Jonsson, J. A. E. Wasey, P. T. Worthing, and V. Zwiller. Solid-state single photon sources: light collection strategies. *Eur. Phys. J. D*, 18:197, 2002.

[9] Arvind Baskaran and Peter Smereka. Mechanisms of stranski-krastanov growth. *Journal of applied physics*, 111(4):044321–044321–6, 2012.

[10] Michael Bass, Casimer DeCusatis, Jay M Enoch, Vasudevan Lakshminarayanan, Guifang Li, Carolyn Ann MacDonald, Virendra N Mahajan, and Eric W Van Stryland. *Handbook of optics*. McGraw-Hill's AccessEngineering. McGraw-Hill, New York, 3rd ed. edition, 2010.

[11] M. Bayer, P. Hawrylak, K. Hinzer, S. Fafard, M. Korkusinski, Z. R. Wasilewski, O. Stern, and A. Forchel. Coupling and entangling of quantum states in quantum dot molecules. *Science*, 291(5503):451–453, 2001.

[12] M. Bayer, G. Ortner, O. Stern, A. Kuther, A. A. Gorbunov, A. Forchel, P. Hawrylak, S. Fafard, K. Hinzer, T. L. Reinecke, S. N. Walck, J. P. Reithmaier, F. Klopf, and F. Schäfer. Fine structure of neutral and charged excitons in self-assembled In(Ga)As/(Al)GaAs quantum dots. *Phys. Rev. B*, 65:195315, 2002.

[13] Manfred Bayer. Bridging two worlds: Colloidal versus epitaxial quantum dots. *Annalen der Physik*, 531(6):1900039, 2019.

[14] C.H. Bennett and G. Brassard. Quantum cryptography: Public key distribution and coin tossing. *Proceedings of IEEE International Conference on Computers, Systems and Signal Processing*, 175:8, 1984.

[15] Jochen Bissinger, Daniel Ruhstorfer, Thomas Stettner, Gregor Koblmüller, and Jonathan J Finley. Optimized waveguide coupling of an integrated III-V nanowire laser on silicon. *Journal of applied physics*, 125(24):243102–, 2019.

[16] M. T. Björk, B. J. Ohlsson, T. Sass, A. I. Persson, C. Thelander, M. H. Magnusson, K. Deppert, L. R. Wallenberg, and L. Samuelson. One-dimesional heterostructures in semiconductor nanowhiskers. *Appl. Phys. Lett.*, 80:1058, 2002.

[17] J. Bleuse, J. Claudon, M. Creasey, N. S. Malikand, J.-M. Gérard, I. Maksymov, J.-P. Hugonin, and P. Lalanne. Inhibition, enhancement, and control of spontaneous emission in photonic nanowires. *Phys. Rev. Lett.*, 106:103601, 2011.

[18] M. Borgström, V. Zwiller, E. Müller, and A. Imamoglu. Optically bright quantum dots in single nanowires. *Nano Lett.*, 5:1439–1443, 2005.

[19] Robert W. Boyd. *Nonlinear Optics*. Academic Press, San Diego, CA, 2nd ed. edition, 2003.

[20] R. Hanbury Brown and R. Q. Twiss. A test of a new type of stellar interferometer on sirius. *Nature*, 178:1046–1048, 1956.

[21] M. Jr. Bruchezm, M Moronne, P Gin, S Weiss, and A. P Alivisatos. Semiconductor nanocrystals as fluorescent biological labels. *Science (American Association for the Advancement of Science)*, 281(5385):2013–2016, 1998.

[22] G. Bulgarini, M. E. Reimer, M. Bouwes Bavinck, K. D. Jöns, D. Dalacu, P. J. Poole, E. P. A. M. Bakkers, and V. Zwiller. Nanowire waveguides launching single photons in a gaussian mode for ideal fiber coupling. *Nano Lett.*, 7:4102–4106, 2014.

[23] Gabriele Bulgarini. Nanowire-based quantum photonics, 2014.

[24] Chloé Bureau-Oxton, Julien Camirand Lemyre, and Michel Pioro-Ladrière. Nanofabrication of gate-defined GaAs/AlGaAs lateral quantum dots. *Journal of visualized experiments : JoVE*, (81):e50581–e50581, 2013.

[25] N. Chauvin, M. H. Hadj Alouane, R. Anufriev, H. Khmissi, K. Naji, G. Patriarche, C. Bru-Chevallier, and M. Gendry. Growth temperature dependence of exciton lifetime in wurtzite inp nanowires grown on silicon substrates. *Appl. Phys. Lett.*, 100:011906, 2012.

[26] N. Chauvin, B. Salem, G. Bremond, G. Guillot, C. Bru-Chevallier, and M. Gendry. Size and shape effects on excitons and biexcitons in single InAs/InP quantum dots. *J. Appl. Phys.*, 100:073702, 2006.

[27] Lirong Cheng, Simei Mao, Zhi Li, Yaqi Han, and H Fu. Grating couplers on silicon photonics: Design principles, emerging trends and practical issues. *Micromachines (Basel)*, 11(7):666–, 2020.

[28] Andreas Christ and Christine Silberhorn. Limits on the deterministic creation of pure single-photon states using parametric down-conversion. *Physical review. A, Atomic, molecular, and optical physics*, 85(2), 2012.

[29] J. Claudon, J. Bleuse, N. S. Malik, M. Bazin, P. Jaffrennou, N. Gregersen, C. Sauvan, P. Lalanne, and J.-M. Gérard. A highly efficient single-photon source based on a quantum dot in a photonic nanowire. *Nat. Photon.*, 4:174, 2010.

[30] Claude Cohen-Tannoudji. *Quantum mechanics.* Wiley, New York, 1977.

[31] Moritz Cygorek, Marek Korkusinski, and Pawel Hawrylak. Atomistic theory of electronic and optical properties of InAsP/InP nanowire quantum dots. *Phys. Rev. B*, 101:075307, 2020.

[32] D. Dalacu, K. Mnaymneh, J. Lapointe, X. Wu, P. J. Poole, G. Bulgarini, V. Zwiller, and M. E. Reimer. Ultraclean emission from InAsP quantum dots in defect-free wurtzite InP nanowires. *Nano Lett.*, 12:5919–5923, 2012.

[33] D. Dalacu, K. Mnaymneh, X. Wu, J. Lapointe, G. C. Aers, P. J. Poole, and R. L. Williams. Selective-area vapor-liquid-sold growth of tunable InAsP quantum dots in nanowires. *Appl. Phys. Lett.*, 98:251101, 2011.

[34] Dan Dalacu, Philip J. Poole, and Robin L. Williams. Nanowire-based sources of non-classical light. *Nanotechnology*, 30:232001, 2019.

[35] Dan Dalacu, Philip J. Poole, and Robin L. Williams. Tailoring the geometry of bottom-up nanowires: Application to high efficiency single photon sources. *Nanomaterials*, 11(5), 2021.

[36] Marcelo Davanco, Jin Liu, Luca Sapienza, Chen-Zhao Zhang, José Vinícius De Miranda Cardoso, Varun Verma, Richard Mirin, Sae Woo Nam, Liu Liu, and Kartik Srinivasan. Heterogeneous integration for on-chip quantum photonic circuits with single quantum dot devices. *Nat. Commun.*, 8:889, 2017.

[37] Guang-Wei Deng, Nan Xu, and Wei-Jie Li. *Gate-Defined Quantum Dots: Fundamentals and Applications*, pages 107–133. Springer International Publishing, Cham, 2020.

[38] A.W.A Elshaari, I.Z Esmaeil Zadeh, A.W Fognini, Michael E Reimer, Dan Dalacu, Philip J Poole, V.G Zwiller, and Klaus D Jöns. On-chip single photon filtering and multiplexing in hybrid quantum photonic circuits. *Nature communications*, 8(1):379–379, 2017.

[39] Saim Emin, Surya P. Singh, Liyuan Han, Norifusa Satoh, and Ashraful Islam. Colloidal quantum dot solar cells. *Solar Energy*, 85(6):1264–1282, 2011.

[40] D. Englund, D. Fattal, E. Waks, G. Solomon, B. Zhang, T. Nakaoka, Y. Arakawa, Y. Yamamoto, and J. J. Vučković. Controlling the spontaneous emission rate of single quantum dots in a two-dimensional photonic crystal. *Phys. Rev. Lett.*, 95:013904, 2005.

[41] I. Friedler, C. Sauvan, J. P. Hugonin, P. Lalanne, J. Claudon, and J. M. Gérard. Solid-state single photon sources: the nanowire antenna. *Opt. Exp.*, 17:2095, 2009.

[42] Akira Furusawa. *Quantum states of light*. SpringerBriefs in mathematical physics, volume 10. Springer, Tokyo, 2015.

[43] E. G. Gadret, G. O. Dias, L. C. O. Dacal, Jr. M. M. de Lima, C. V. R. S. Ruffo, F. Iikawa, M. J. S. P. Brasil, T. Chiaramonte, M. A. Cotta, L. H. G. Tizei, D. Ugarte, and A. Cantarero. Valence-band splitting energies in wurtzite InP nanowires: Photoluminescence spectroscopy and *ab initio* calculations. *Phys. Rev. B*, 182:125327, 2010.

[44] Raja Gajjela and Paul M Koenraad. Atomic-scale characterization of droplet epitaxy quantum dots. *Nanomaterials (Basel, Switzerland)*, 11(1):85, 2021.

[45] Jean-Michel Gérard and Bruno Gayral. Strong purcell effect for InAs quantum boxes in three-dimensional solid-state microcavities. *J. Lightwave Tech.*, 17:2089, 1999.

[46] Christopher C. Gerry and Peter L. Knight. *Introductory quantum optics*. Cambridge University Press, Cambridge, UK, 2005.

[47] Frank Glas, Jean-Christophe Harmand, and Gilles Patriarche. Why does wurtzite form in nanowires of III-V zinc blende semiconductors? *Physical review letters*, 99(14):146101–146101, 2007.

[48] Roy J Glauber. *Quantum Theory of Optical Coherence*. Wiley-VCH, 1. aufl. edition, 2007.

[49] S.V Goupalov, E.L Ivchenko, and A.V Kavokin. Anisotropic exchange splitting of excitonic levels in small quantum systems. *Superlattices and microstructures*, 23(6):1205–1209, 1998.

[50] Philippe Guyot-Sionnest. Quantum dots: An emerging class of soluble optical nanomaterials. *Material Matters*, 2(1), 2007.

[51] R Hanbury Brown and R. Q Twiss. Correlation between photons in two coherent beams of light. *Nature*, 177(4497):27–29, 1956.

[52] J. Heinrich, A. Hugenberger, T. Heindel, S. Reitzenstein, S. Höfling, L. Worschech, and A. Forchel. Single photon emission from positioned GaAs/AlGaAs photonic nanowires. *Appl. Phys. Lett.*, 96:211117, 2010.

[53] M Holmes, S Kako, K Choi, M Arita, and Y Arakawa. Spectral diffusion and its influence on the emission linewidths of site-controlled GaN nanowire quantum dots. *Physical Review. B, Condensed matter and materials physics*, 92(11), 2015.

[54] C. K Hong, Z. Y Ou, and L Mandel. Measurement of subpicosecond time intervals between two photons by interference. *Phys. Rev. Lett.*, 59(18):2044–2046, 1987.

[55] Daniel Huber, Marcus Reindl, Yongheng Huo, Johannes S. Wildmann Huiying Huang and, Oliver G. Schmidt, Armando Rastelli, and Rinaldo Trotta. Highly indistinguishable and strongly entangled photons from symmetric gaas quantum dots. *Nat. Commun.*, 8:15506, 2017.

[56] Robert G. Hunsperger. *Integrated Optics Theory and Technology*. Advanced texts in physics. Springer New York, New York, NY, 6th ed. 2009. edition, 2009.

[57] M. Saif Islam, S. Sharma, T. I. Kamins, and R. Stanley Williams. Ultrahigh-density silicon nanobridges formed between two vertical silicon surfaces. *Nanotech.*, 15:L5, 2004.

[58] I. E Itskevich, S. I Rybchenko, I. I Tartakovskii, S. T Stoddart, A Levin, P. C Main, L Eaves, M Henini, and S Parnell. Stark shift in electroluminescence of individual InAs quantum dots. *Applied physics letters*, 76(26):3932–3934, 2000.

[59] Eric M Janke, Nicholas E Williams, Chunxing She, Danylo Zherebetskyy, Margaret H Hudson, Lili Wang, David J Gosztola, Richard D Schaller, Byeongdu Lee, Chengjun Sun, Gregory S Engel, and Dmitri V Talapin. Origin of broad emission spectra in inp quantum dots: Contributions from structural and electronic disorder. *Journal of the American Chemical Society*, 140(46):15791–15803, 2018.

[60] L. E. Jensen, S. Jeppesen M. T. Björk, A. I. Persson, B. J. Ohlsson, and L. Samuelson. Role of surface diffusion in chemical beam epitaxy of InAs nanowires. *Nano Lett.*, 4:1961–1964, 2004.

[61] J. Johansson, K. A. Dick, P. Caroff, M. E. Messing, J. Bolinsson, K. Deppert, and L.Samuelson. Diameter dependence of the wurtzite-zinc blende transition in InAs nanowires. *J. Phys. Chem. C*, 114:3837–3842, 2010.

[62] Sokratis Kalliakos, Yarden Brody, Andre Schwagmann, Anthony J Bennett, Martin B Ward, David J. P Ellis, Joanna Skiba-Szymanska, Ian Farrer, Jonathan P Griffiths, Geb A. C Jones, David A Ritchie, and Andrew J Shields. In-plane emission of indistinguishable photons generated by an integrated quantum emitter. *Applied Physics Letters*, 104(22):221109–, 2014.

[63] A. Kiraz, S. Fälth, C. Becher, B. Gayral, W. V. Schoenfeld, P. M. Petroff, Lidong Zhang, E. Hu, and A. Imamoglŭ. Photon correlation spectroscopy of a single quantum dot. *Phys. Rev. B*, 65:161303(R), 2002.

[64] E. Knill, R. Laflamme, and G. Milburn. A scheme for efficient linear optics quantum computation. *Nature*, 409:46–52, 2001.

[65] Bernard C. Kress. Coupling losses in optical waveguides. In *Field Guide to Digital Micro-Optics*, pages 10–10. SPIE Press, 2014.

[66] A. V. Kuhlmann, J. Houel, D. Brunner, A. Ludwig, D. Reuter, A. D. Wieck, and R. J. Warburton1. A dark-field microscope for background-free detection of resonance fluorescence from single semiconductor quantum dots operating in a set-and-forget mode. *Rev. Sci. Inst.*, 84:073905, 2013.

[67] Patrick Laferrière, Edith Yeung, Lambert Giner, Sofiane Haffouz, Jean Lapointe, Geof C. Aers, Philip J. Poole, Robin L. Williams, and Dan Dalacu. Multiplexed single-photon source based on multiple quantum dots embedded within a single nanowire. *Nano Lett.*, 20:3688–3693, 2020.

[68] Patrick Laferrière, Edith Yeung, Marek Korkusinski, Philip J. Poole, Robin L. Williams, Dan Dalacu, Jacob Manalo, Moritz Cygorek, Abdulmenaf Altintas, and Pawel Hawrylak. Systematic study of the emission spectra of nanowire quantum dots. *Appl. Phys. Lett.*, 2021.

[69] H.-K. Lo and H.-F. Chau. Unconditional security of quantum key distribution over arbitrarily long distances. *Science*, 283:2050–2056, 1999.

[70] H.-K. Lo, M. Curty, and B. Qi. Measurement-device-independent quantum key distribution. *Phys. Rev. Lett.*, 108:130503, 2012.

[71] P. Lodahl, S. Mahmoodian, and S. Stobbe. Interfacing single photons and single quantum dots with photonic nanostructures. *Rev. Mod. Phys.*, 87:347, 2015.

[72] Leandro Lorenzo, Hastrup Jacob, Reznik Rodion, Cirlin George, and Akopian Nika. Resonant excitation of nanowire quantum dots. *NPJ Quantum Information*, 6(1), 2020.

[73] E. A. J Marcatili and S. E Miller. Improved relations describing directional control in electromagnetic wave guidance. *Bell System Technical Journal*, 48(7):2161–2188, 1969.

[74] Morgan Mastrovich. Characterizing single photon emission from quantum dots in nanowires, 2019.

[75] Evan Meyer-Scott, Christine Silberhorn, and Alan Migdall. Single-photon sources: Approaching the ideal through multiplexing. *Review of Scientific Instruments*, 91(4):041101–041101, 2020.

[76] Peter Michler. *Quantum Dots for Quantum Information Technologies*. Nano-Optics and Nanophotonics. Springer, CH, 1st ed. 2017 edition, 2017.

[77] Alan Migdall, Sergey V Polyakov, Jingyun Fan, and Joshua C Bienfang. *Single-Photon Generation and Detection: Physics and Applications*, volume 45 of *Experimental methods in the physical sciences*. Elsevier Science & Technology, San Diego, 2013.

[78] E. Moreau, I. Robert, L. Manin, V. Thierry-Mieg, J. M. Gérard, and I. Abram. Quantum cascade of photons in semiconductor quantum dots. *Phys. Rev. Lett.*, 87:183601, 2001.

[79] Padraic Edward Morrissey, David Goulding, Robert Sheehan, Brendan Roycroft, and Frank H Peters. Experimental technique for quick and efficient lensed fibre to ridge waveguide coupling. *IET optoelectronics*, 7(2):57–61, 2013.

[80] M.Shirane, Y. Igarashiab, Y. Ota, M. Nomura, N. Kumagai, S. Ohkouchi, A. Kirihara, S. Ishida, S. Iwamoto, S. Yorozu, and Y. Arakawa. Charged and neutral biexciton–exciton cascade in a single quantum dot within a photonic bandgap. *Physica E*, 42:2563–2566, 2010.

[81] B. Ohnesorge, M. Bayer, A. Forchel, J. P. Reithmaier, N. A. Gippius, and S. G. Tikhodeev. Enhancement of spontaneous emission rates by three-dimensional photon confinement in bragg microcavities. *Phys. Rev. B*, 56(8):R4367–R4370, 1997.

[82] Zhenxiao Pan, Huashang Rao, Iván Mora-Seró, Juan Bisquert, and Xinhua Zhong. Quantum dot-sensitized solar cells. *Chemical Society reviews*, 47(2):7659–772, 2018.

[83] M. Pelton, C. Santori, J. Vučković, B. Zhang, G. S. Solomon, J. Plant, and Y. Yamamoto. Efficient source of single photons: A single quantum dot in a micropost microcavity. *Phys. Rev. Lett.*, 89(23):233602, 2002.

[84] M. Pfeiffer, C. Herkommer, Junqiu Liu, T. Morais, M. Zervas, M. Geiselmann, and T. Kippenberg. Photonic damascene process for low-loss, high-confinement silicon nitride waveguides. *IEEE Journal of Selected Topics in Quantum Electronics*, 24:1–11, 2018.

[85] Martin H. P. Pfeiffer, Arne Kordts, Victor Brasch, Michael Zervas, Michael Geiselmann, John D. Jost, and Tobias J. Kippenberg. Photonic damascene process for integrated high-Q microresonator based nonlinear photonics. *Optica*, 3(1):20–25, Jan 2016.

[86] Martin H. P. Pfeiffer, Junqiu Liu, Arslan S. Raja, Tiago Morais, Bahareh Ghadiani, and Tobias J. Kippenberg. Ultra-smooth silicon nitride waveguides based on the damascene reflow process: fabrication and loss origins. *Optica*, 5(7):884–892, Jul 2018.

[87] P. J. Poole, D. Dalacu, X. Wu, J. Lapointe, and K. Mnaymneh. Interplay between crystal phase purity and radial growth in InP nanowires. *Nanotech.*, 23(38):385205, 2012.

[88] P. J. Poole, J. McCaffrey, R. L. Williams, J. Lefebvre, and D. Chitrani. Chemical beam epitaxy of self-assembled InAs/InP quantum dots. *J. Vac. Sci. Technol. B*, 19(4):1467–1470, 2001.

[89] M. E. Reimer, G. Bulgarini, N. Akopian, M. Hocevar, M. Bouwes Bavinck, M. A. Verheijen, E. P. A. M. Bakkers, L. P. Kouwenhoven, and V. Zwiller. Bright single-photon sources in bottom-up tailored nanowires. *Nat. Commun.*, 3:737, 2012.

[90] M. E. Reimer, G. Bulgarini, A. Fognini, R. W. Heeres, B. J. Witek, M. A. M. Versteegh, A. Rubino, T. Braun, M. Kamp, S. Höfling, D. Dalacu, J. Lapointe, P. J. Poole, and V. Zwiller. Overcoming power broadening of the quantum dot emission in a pure wurtzite nanowire. *Phys. Rev. B*, 93:195316, 2016.

[91] M. E. Reimer, D. Dalacu, J. Lapointe, P. J. Poole, D. Kim, G. C. Aers, W. R. McKinnon, and R. L. Williams. Single electron charging in deterministically positioned inas/inp quantum dots. *Appl. Phys. Lett.*, 94:011108, 2009.

[92] M. E. Reimer, W. R. McKinnon, J. Lapointe, P. J. Poole, G. C. Aers, D. Kim, M. Korkusiński, P. Hawrylak, and R. L. Williams. Towards scalable gated quantum dots for quantum information applications. *Physica E*, 40:1790–1793, 2008.

[93] M. E. Reimer, M. P. van Kouwen, A. W. Hidma, M. H. M. van Weert, E. P. A. M. Bakkers, L. P. Kouwenhoven, and V. Zwiller. Electric field induced removal of the biexciton binding energy in a single quantum dot. *Nano Lett.*, 11:645–650, 2010.

[94] M Saif Islam, S Sharma, T.I Kamins, and R Stanley Williams. A novel interconnection technique for manufacturing nanowire devices. *Applied Physics. A, Materials science & processing*, 80(6):1133–1140, 2005.

[95] Bahaa E. A. Saleh. *Fundamentals of photonics*. Wiley, Hoboken, N.J, 2nd edition, 2007.

[96] G. Sallen, A. Tribu, T. Aichele, R. André, L. Besombes, S. Bougerol, M. Richard, S. Tatarenko, K. Kheng, and J.-Ph. Poizat. Subnanosecond spectral diffusion of a single quantum dot in a nanowire. *Phys. Rev. B*, 84:041405, 2011.

[97] C. Santori, D. Fattal, J. Vučković, G. Solomon, and Y. Yamamoto. Indistinguishable photons from a single-photon device. *Nature*, 419:594–597, October 2002.

[98] Charles Michael Santori. Generation of nonclassical light using semiconductor quantum dots, 2003.

[99] Andre Schwagmann, Sokratis Kalliakos, Ian Farrer, Jonathan P. Griffiths, Geb A. C. Jones, David A. Ritchie, and Andrew J. Shields. On-chip single photon emission from an integrated semiconductor quantum dot into a photonic crystal waveguide. *Appl. Phys. Lett.*, 99(26):261108, 2011.

[100] R. Singh and G. Bester. Nanowire quantum dots as an ideal source of entangled photon pairs. *Phys. Rev. Lett.*, 103:063601, 2009.

[101] Gyeongho Son, Seungjun Han, Jongwoo Park, Kyungmok Kwon, and Kyoungsik Yu. High-efficiency broadband light coupling between optical fibers and photonic integrated circuits. *Nanophotonics*, 7(12):1845–1864, 2018.

[102] I. N. Stranski and Von L. Krastanow. Zur theorie der orientierten ausscheidung von ionenkristallen aufeinander. *Akad. Wiss. Lit. Mainz Abh. Math. Naturwiss. Kl. II b*, 146:797–810, 1938.

[103] S Studenikin, L Gaudreau, A Sachrajda, P Zawadzki, A Kam, J Lapointe, M Korkusinski, and P Hawrylak. Charging characteristics of a few electron triple lateral quantum dot system in GaAs/AlGaAs. In *2006 Sixth IEEE Conference on Nanotechnology*, volume 2, pages 871–874. IEEE, 2006.

[104] T. Takagahara. Theory of exciton dephasing in semiconductor quantum dots. *Phys. Rev. B*, 60:2638, 1999.

[105] A. Tribu, G. Sallen, T. Aichele, R. André, J.-P. Poizat, C. Bougerol, S. Tatarenko, and K. Kheng. A high-temperature single-photon source from nanowire quantum dots. *Nano Lett.*, 8:4326–4329, 2008.

[106] M. A. M. Versteegh, M. E. Reimer, K. D. Jöns, D. Dalacu, P.J. Poole, A. Gulinatti, A. Giudice, and V. Zwiller. Observation of strongly entangled photon pairs from a nanowire quantum dot. *Nat. Commun.*, 5:6298, 2014.

[107] Linghua Wang, Weiqiang Xie, Dries Van Thourhout, Yazhen Zhang, Hui Yu, and Shaohao Wang. Nonlinear silicon nitride waveguides based on a PECVD deposition platform. *Optics express*, 26(8):9645–9654, 2018.

[108] Jimmy Xu, Sylvain G Cloutier, and Pavel A Kossyrev. Optical gain and stimulated emission in periodic nanopatterned crystalline silicon. *Nature materials*, 4(12):887–891, 2005.

[109] E. Yablonovitch. Inhibited spontaneoius emission in solid-state physics and electronics. *Phys. Rev. Lett.*, 58:2059–2062, 1987.

[110] Iman Esmaeil Zadeh, Ali W Elshaari, Klaus D Jöns, Andreas Fognini, Dan Dalacu, Philip J Poole, Michael E Reimer, and Val Zwiller. Deterministic integration of single photon sources in silicon based photonic circuits. *Nano letters*, 16(4):2289–2294, 2016.

[111] Tiecheng Zhu, Yiwen Hu, Pradip Gatkine, Sylvain Veilleux, Joss Bland-Hawthorn, and Mario Dagenais. Ultrabroadband high coupling efficiency fiber-to-waveguide coupler using Si $_3N_4$ /SiO_2 waveguides on silicon. *IEEE Photonics Journal*, 8(5):1–12, 2016.